# ONE- AND TWO-DIMENSIONAL COUPLING MODELING APPROACHES FOR FLOOD SIMULATIONS

by

**Cesar A. Simon**

B.S. in Civil Engineering, Universidad Nacional de Ingeniería,

Lima, 2003

M.S. in Civil Engineering, University of Pittsburgh, 2013

M.A. in Mathematics, University of Pittsburgh, 2014

Submitted to the Graduate Faculty of

Swanson School of Engineering in partial fulfillment

of the requirements for the degree of

Doctor of Philosophy

University of Pittsburgh

2019

UNIVERSITY OF PITTSBURGH

SWANSON SCHOOL OF ENGINEERING

This dissertation was presented

by

Cesar A. Simon

It was defended on

March 6, 2019

and approved by

Jorge D. Abad, Ph.D., Professor
Department of Civil and Environmental Engineering
University of Technology and Engineering, Peru

Radisav Vidic, Ph.D., Professor
Department of Civil and Environmental Engineering

Daniel D. Budny, Ph.D., Associate Professor
Department of Civil and Environmental Engineering

Eddy J. Langendoen, Ph.D., Hydraulic Engineer
National Sedimentation Laboratory, Agricultural Research Service
United States Department of Agriculture

Dissertation Director: Jorge D. Abad, Ph.D., Professor
Department of Civil and Environmental Engineering
University of Technology and Engineering, Peru

**ONE- AND TWO-DIMENSIONAL COUPLING MODELING APPROACHES FOR FLOOD SIMULATIONS**

Cesar A. Simon, PhD

University of Pittsburgh, 2019

The application of numerical models to calculate the inundation extent and exerted forces of flood events is critical in developing flood damage mitigation plans. One-dimensional (1D) models of open-channel flow are efficient for simulating in-channel hydrodynamics over long reaches and periods but cannot accurately predict overbank flows that require two-dimensional (2D) models. For rapid analysis of many different scenarios or to evaluate model uncertainty, a combination of 1D (in the channel) and 2D (on over-banks) open-channel flow computer models is preferred.

This thesis presents the derivation and discussion of the behavior of the coupling terms for horizontal and vertical coupling of the governing equations of 1D and 2D flow. The coupling introduces transfer terms for mass and momentum. For both coupling methods and relatively high overbank flow depth, the advective momentum transfer exceeded the diffusive momentum transfer. The advective momentum transfer was one order of magnitude higher for the horizontal coupling approach than for the vertical coupling approach.

This research compares vertical and horizontal coupling strategies of widely used 1D and 2D models to simulate flooding events. The study assesses the capability of both approaches to accurately model flooding events for an experiment of overbank flow in a meandering channel. The results showed that the horizontal coupling method yields inaccurate flow fields if the horizontal transfer of mass and momentum between floodplain flow and channel flow is inadequately accounted. The vertical coupling approach implicitly accounts for the lateral transfer between

floodplain flow and channel flow and accounts for the vertical transfer of mass and momentum between overbank and in-bank flow.

Finally, this work compares flooding results in Iquitos City, Peru, of a coupled 1D-2D HEC-RAS model against a 2D HEC-RAS model. Although both models show similar flooding extension, the coupling 1D-2D model uses fewer elements in its discretization. Both models were able to predict flooding near critical infrastructure for the specified flow conditions. The incorporation of the climate change in the simulation shows higher flooding results in both models. The results show that flooding does not extend to the southwest areas of Iquitos city, making that zone safer for development.

## TABLE OF CONTENTS

## LIST OF TABLES

## LIST OF FIGURES

## PREFACE

I thank my wife Janeth for her support and patience during this process. Thanks to my parents whose examples I follow.

I truly appreciate the help of Dr. Vidic and all my committee members for their evaluation and recommendations in my thesis defense. I specially thank my advisor, Dr. Abad, and Dr. Langendoen for their guidance in my research.

Many friends helped me through the research process: I can not forget to thank Dr. Alejandro Mendoza, Dr. Christian Frias, Mr. Jeffrey Herzog, Mr. Robert Rosenthal P.E., Mr. Frederick Douglas.

# 1.0 INTRODUCTION

Historically, human settlements developed in areas that are favorable to human activities. Human settlements mainly occurred in floodplain areas. Floodplains are a geologic characteristic of the terrain developed by river activity. The hydraulic regime of the river, caused by seasonal variations of climate and production of rain, creates an episodic deposition of alluvium along the valley of the river as a consequence of floods. Periodic deposition is the primary process of the genesis of floodplains. We may infer flooding produces flat terrains in the surrounding areas of rivers. Floodplains characteristics are their access to water and transportation, interaction with life such as tree-like plants (Wohl, 2013), and rich nutrient soils; from here, its historical role to civilization. Floodplains are especially important for agriculture because they have a significant potential for food production (Hofer & Messerli, 2006). Nowadays, the agricultural activity in flood-prone areas generates around $ 371,000 million of Gross Domestic Product (GDP) (Dilley, Chen, & Deichmann, 2005). For that reason, the intensity of land use is growing in these areas in the form of agricultural, urban and industrial growth, and high investment in infrastructure and transport systems (Hofer & Messerli, 2006). Existing estimations calculate 1,191 thousand kilometers of road and rail length cross flood-prone areas (Dilley et al., 2005).

Due to the increase in population and infrastructure density, combined with climate change, the associated risk of floodplains is growing (Hofer & Messerli, 2006). Flooding is one of the major natural disasters around the world (Bernini & Franchini, 2013; Connell, Painter, & Beffa, 2001; A. Cook & Merwade, 2009). Floods impact ecosystems, human lives and livelihoods (Jung, Alsdorf, Moritz, Lee, & Vassolo, 2011; O'Connor & Costa, 2008). They have caused the loss of 96,507 human lives between 1992 to 2001 and 170,010 between 1980 to 2000 (Dilley et al., 2005). Each decade there are around 10,000 deaths due to flood events (Jha, Bloch, & Lamond, 2012). "In 2010, alone, 178 million people were affected by floods" (Jha et al., 2012). Also, they are the cause

of economic losses of billions of dollars (Bernini & Franchini, 2013; Connell et al., 2001; A. Cook & Merwade, 2009; Jha et al., 2012). As an example, in exceptional years such as 1998 and 2010, the economic losses associated with flooding exceeded $40 billion" (Jha et al., 2012). For that reason, floodplain management has become an increasingly fundamental topic world-wide (Hofer & Messerli, 2006). Flood-prone areas (11.5 millions $km^2$) account for approximately one third of the world's land area where 82% of the population resides (a population around 2,283 millions) (Dilley et al., 2005).

"The flood-prone regions include large areas of the Midwestern United States, Central America, South America, Europe, eastern Africa, North-eastern India and Bangladesh, China, the Korean peninsula, South-eastern Asia, Indonesia, and the Philippines" (Dilley et al., 2005). Figure 1.1 in Dilley et al. (2005) show the areas in the world (with a density above 105 people per square kilometer) in risk of flooding, categorized by its hazard level.

Determining the extent of inundation and forces exerted on infrastructure during flood events is critical in the development of contingency planning, rescue and relief operations (Connell et al., 2001; A. Cook & Merwade, 2009). These flood characteristics can be examined by field investigation or estimated by applying numerical models (Costabile & Macchione, 2011).

Although most studies do not depict the Amazon basin (Figure 1 in J. L. Chen, Wilson, and Tapley (2010)) as a region of high flooding problem, many statistics exclude this area due to its low population density. However, the flood events in this basin extend longer and affect a larger population in cities like Iquitos (Coordinadora Nacional de Derechos Humanos, 2012; Espinoza et al., 2013). The map shown in Figure 1.1 in Dilley et al. (2005) is an example of the lack of studies in this area. Indeed, "No work has been dedicated to the highest floods in the western Amazon basin" (Espinoza et al., 2013). Even though sedimentary history and pollen data show that flooding has altered the Amazonian ecosystem over several millennia, these non-equilibrium processes could be the reason for the well know species-richness in the Amazonian (Colinvaux, Miller, Liu, & Steinitz-Kannan, 1985).

The Amazon basin is the largest drainage basin in the world with a total area of 7.05 million $km^2$ ($2.72 \times 106$ square miles), which is about 40% of the total area of South America, and extends inside several countries (see Figure 1 in J. L. Chen et al. (2010)) (J. L. Chen et al., 2010). From the 1980s the Amazon basin experimented with an intensification of hydrological extremes, which

mainly affects the Andes rivers of this basin (Espinoza et al., 2013). Nowadays, surface water (high) stage, discharge, flood extent, and floodplain-river connectivity are being monitored using satellite sensors, complementing the terrestrial stations (Birkett, 2002; Hall, Schumann, Bamber, & Bates, 2011). The use of satellite gravity missions, such as the Gravity Recovery and Climate Experiment (GRACE), bring new capabilities to study extreme climate events (J. L. Chen et al., 2010). The study of Martinez and Le Toan (2007) demonstrates that temporal variations of the radar backscatter can be used to efficiently monitor the flood extent and make maps with a precision of 90% in excess to a flood stage. Results show (see Figure 9 in Martinez and Le Toan (2007)) that the flood stress governs the vegetation communities distribution (Martinez & Le Toan, 2007).

M. Wilson et al. (2007) made the first 2D hydrodynamic model application for the Amazon (in Brazil) at a scale of 240 x 150 km. They used topographic data from the Shuttle Radar Topography Mission as an input to the 2D hydrodynamic model LISFLOOD-FP and compared the results with inundation extents and water level from satellite estimates and existing gauged data. Results show (see Figure 2 in M. Wilson et al. (2007)) that a higher proportion of the river discharge than previously thought, flow through the floodplain (M. Wilson et al., 2007).

Coe, Costa, and Howard (2008) improved a water balance model including dependence on river sinuosity and friction to describe their impacts on the simulated surface water dynamics of the Amazon river basin. Coe et al. (2008) used 1 km resolution topographic data from the Shuttle Radar Topography Mission in order to calculate the statistics of the fractional flooding for each grid cell. Coe et al. (2008) used these statistics combined with field measurements as inputs for the model. The model was calibrated and validated against 122 gauge stations (see Figure 1 in Coe et al. (2008)). The results for the simulated period 1968-1998 show an accuracy of 5% to the satellite-derived estimates of flooded area (Coe et al., 2008).

The monthly gravity solutions of GRACE records over the seven (7) years from April 2002 to August 2009 show the changing evolution in both non-seasonal and inter-annual water storage in the Amazon basin (J. L. Chen et al., 2010). J. L. Chen et al. (2010) affirm that "GRACE measurements are consistent with precipitation data" and the Inter-annual terrestrial water storage changes in the Amazon basin closely connect to events in the tropical Pacific, especially El Niño (or ENSO). J. L. Chen et al. (2010) connect the 2002-2003 dry season with the El Niño of 2002-2003 and the high terrestrial water storage increase in the lower Amazon basin in the first half of 2009 that

produce the flooding described by Marengo, Tomasella, Soares, Alves, and Nobre (2012) with La Niña event. Figure 2 in J. L. Chen et al. (2010) shows a comparison of the Amazon river behavior between these two (2) time frames.

Alsdorf, Han, Bates, and Melack (2010) used gravimetric and imaging satellite methods to estimate the amounts of water filling and draining from the main stem Amazon to the floodplain. Alsdorf et al. (2010) calculated an exchange flow rate that varied from $5500\,m^3/s$ to $7500\,m^3/s$ when the floodplain drained to the main Amazon stem. Also, Alsdorf et al. (2010) calculated that from the total floodplain water volume, 80 % comes from overflow and less than 20 % comes from lateral tributaries contributions.

Hall et al. (2011) made a review in the use of remote sensing and its integration with hydrodynamic models in the Amazon basin concluding that, "thanks to the extensive coverage provided by various active remote sensing systems", it is possible to get the flood extent, the floodplain flow direction, and a relationship between the floodplain level and the distance to the main channel.

A study of the Amazon discharge record from 1903 to 1985 show that there was not a significant change in discharge and the inter-annual variability was predominantly between 2 to 3 years (Richey, Nobre, & Deser, 1989). Studies, such as cross-spectrum analysis and others, show a strong relationship over the equatorial region of the sea surface temperatures and climate cycles in the tropical Pacific and Atlantic oceans with rainfall and subsequent hydrographs in the Brazilian Amazon (Liebmann & Marengo, 2001; Richey, Nobre, & Deser, 1989). Liebmann and Marengo (2001) found the best relationships in the transition from wet to dry seasons or entirely within the dry season; highlighting the influence of the sea surface temperatures on the start and end of the rainy season.

In the Amazon river, the time to the peak-level varies from May to July; with a water surface gradient that varies from 1.5 cm/km downstream to 4 cm/km upstream (Birkett, 2002). Satellite radar altimeter results agree with ground-based estimates in the seasonal variation along the main stem of the hysteresis characteristic and velocity of the flood wave (Birkett, 2002). The flood wave velocity is calculated at around 0.35 m/s (Birkett, 2002).

As a large drainage area, the difference in seasonal precipitation between the south and north draining tributaries (see Figure 2 in Alsdorf et al. (2010)) produce a phase lag in the peak flow of 3 months. Also, the high volume of water stored on the floodplains dampens the hydrograph

along the main stem of the Amazon river in a reach of 2000 km between São Paulo de Olivençz and Obidos, Brazil (Richey, Mertes, et al., 1989).

Big rivers of continental scale, like the Amazon, have a significant proportion of their sediment load sequestrated in floodplains (Aalto et al., 2003). A sediment Stratigraphy study in the Andean-Amazonian in the Beni and Mamore river sub-basins (see Figure 1 in Aalto et al. (2003)) show discrete sediment packages of uniform age typically between 20 to 80 cm thick, with a recurrence of about eight (8) years, which indicate a rare cyclic deposition event (Aalto et al., 2003). These episodic deposition events are linked to rapidly rising floods which in turn is associated by Ocean temperature records to La Niña events (Aalto et al., 2003).

The study site used by Trigg et al. (2009) is located in the low Amazon basin (see Figure 1 in Trigg et al. (2009)) inside Brazil. This study uses a 1D diffusive /2D mass transfer model LISFLOOD-FP and as 1D model HEC-RAS, showing this type of tools area adequate for flood event simulation in the Amazon basin.

The results show that the codes underpredict the water stage as is shown in Figure 9 in Trigg et al. (2009). One reason could be the lack of friction considered in the LISFLOOD-FP model which make the pressure terms to act at a lower level.

An unequal massive flooding event hit the Amazon basin in 2009 producing a new water level record of the last 107 years at Manaus Harbour in Brazil (coordinates 3° 8′ 35” S 60° 1′ 1” W) (Marengo et al., 2012). According with Marengo et al. (2012), abnormal warmer surface waters in the tropical South Atlantic moved to south the Seasonal Intertropical Convergence Zone (ITCZ) trigging abundant rainfall in large areas of eastern Amazon and North-east Brazil from May to July 2009, starting the northern Amazon floods earlier than usual and peak coincidently with the southern tributaries in the confluences resulting in an extreme flood.

Gage observations (see Figure 1 in Gloor et al. (2013)) and popular perception claim that the duration and water surface elevation of Amazon floods are increasing (Sternberg, 1987). Espinoza Villar et al. (2009) made a spatiotemporal rainfall variability study for the entire Amazon basin. Furthermore, recent events show a significant increasing trend in the flow rate of the Amazon River at Tamshiyacu station (Espinoza et al., 2013). These recent anomalies differ from all the temporal variabilities studied before. As (Espinoza Villar et al., 2009) indicated, the nowadays flow trend in the Amazon river could relate with a climate change in the zone. Following the trends studied by

Gloor et al. (2013) and shown in Figure 1 in Gloor et al. (2013), it is possible to calculate a future extreme event.

Gloor et al. (2013) show that the zone of the Amazon basin where there is a strong correlation of this trend around the Iquitos city. Also, it is observable that the zone with the highest precipitation increment is the area surrounding Iquitos city Gloor et al. (2013).

We can expect that Iquitos city will suffer, more often, from extreme flooding events similar or higher than the natural disasters have happened in the last decade and without any engineering action, the impacts will impair the regional development.

An unprecedented discharge increase rate from September 2010 (8,300 $m^3/s$) to April 2011 (49,500 $m^3/s$), accompanied by a very strong increase in suspended sediment loads was observed (Espinoza et al., 2013). "During the subsequent 2011/12 austral summer, intense rainfall was reported in large part of the northern Amazon basin, especially since November 2011, which led to anomalously high discharge since January 2012", attained a peak of $55,400\, m^3/s$ on April 19 at Tamshiyacu station located in the Upper Amazon basin (Espinoza et al., 2013). "This situation caused inundations in the main cities of the Peruvian Amazon region, affecting about 140 000 people and leading the Peruvian authorities to declare a state of emergency" (Espinoza et al., 2013). Notably, in Iquitos city, there were more than 100 thousand victims by the flooding events and the following diseases.

Several rivers surround the Iquitos city:: Nanay, Guano, Itaya y Amazonas. Figure 5 in Abad et al. (2013) shows the anabranching dynamic near Iquitos city (Abad & Montoro, 2013; Abad, Paredes, & Montoro, 2010). In 1973, the Amazon river flowed near the central zone of Iquitos city. Along the years the river migrates, in a meandering way, to the east leaving dry zones were the population start to settle. These low-level areas have a higher risk of flooding in case of an extreme event or a reversal migration. Is also possible to observe how the Nanay river confluence has been modified by the Amazon river dynamics (see Figure 5 in Abad et al. (2013)).

The Amazon river, in Iquitos city, present a marked annual water level change (see figure 6 in Abad et al. (2013)).

Recently, inhabitants of the Peruvian Amazonian have experienced the most extreme hydrological event since 1970, (Espinoza et al., 2013) shows that the regime of the river is changing; basically, the extreme events are becoming more pronounced. The pattern of rain shows more

extensive periods of droughts with more intense rains during the wet season, which affects the hydraulic regime of the river directly.

The flood event that occurs in April 2012 rise until 118.97 meters above the sea level (see Figure 1), leaving a big part of the city flooded and a lot of economic loses.

In this Thesis, a computer model that couples inbank and overbank hydraulic processes are tested to predict flooding across the Amazon Basin. The intention is to study the model complexity and controlling parameters required to simulate flooding and apply that theory to a real case, as the extreme flood of 2012 occurred in Iquitos City, Peru. Also, the author analyze how observed and forecasted changes in hydraulic regimes in the Amazon Basin impact flooding in Iquitos City.

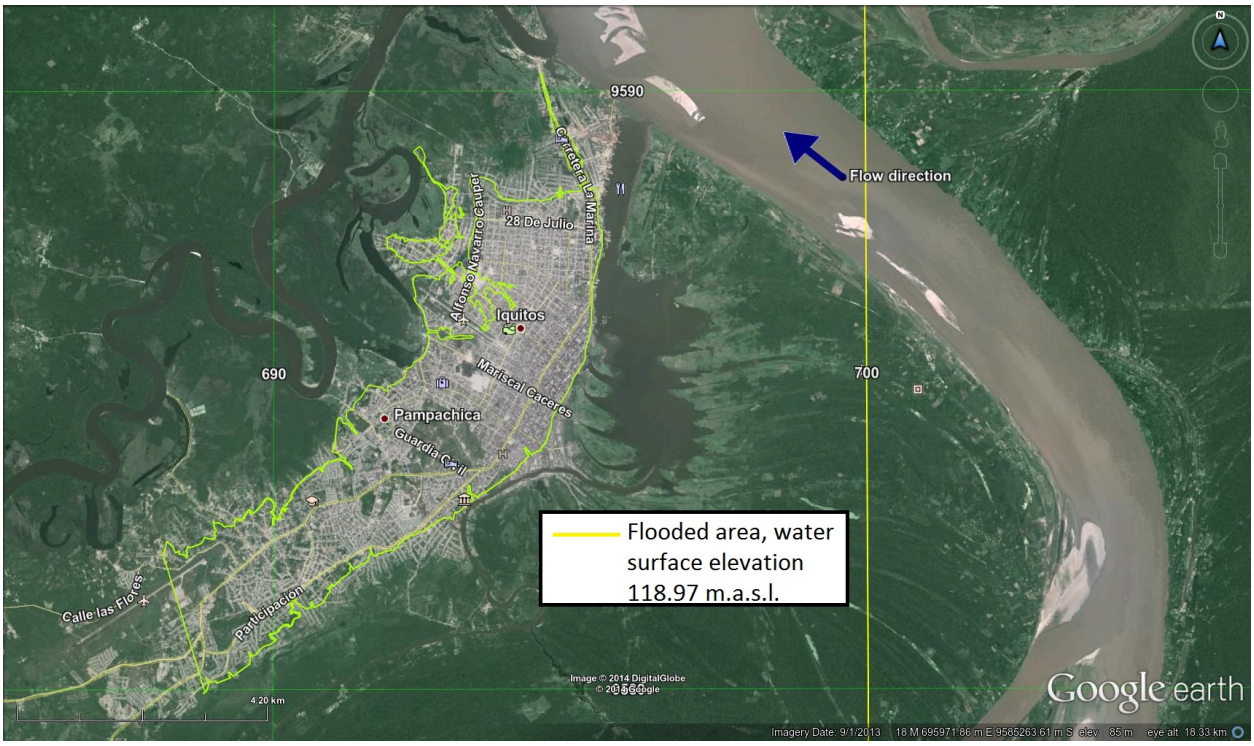


Figure 1: Flooded area in Iquitos city during the extreme event of 2012

# 2.0 ON THE GOVERNING EQUATIONS FOR HORIZONTAL AND VERTICAL COUPLING OF ONE- AND TWO-DIMENSIONAL OPEN CHANNEL FLOW MODELS

## 2.1 INTRODUCTION

Prediction of inundation extent and flood-wave travel time are typical problems addressed by flood inundation models (Horritt & Bates, 2002). In general, river flood studies require the use of hydrodynamic models that can efficiently compute large areas; for example, the 2010 Indus flood had an estimated extent of $17,900\ \text{km}^2$ (Gaurav, Sinha, & Panda, 2011; Khan, Hong, Gourley, Khattak, & De Groeve, 2014; Kwak, Park, & Fukami, 2014; Mustafa & Wrathall, 2011). Practical planning for more regularly occurring floods still requires areas of hundreds of square kilometers to be evaluated. For such flood extents, a two-dimensional (2D) hydrodynamic model may not be efficient, and a one-dimensional (1D) hydrodynamic model cannot capture the flow with sufficient detail along the floodplain (R. Liu & Liu, 2002).

Cross-section averaged 1D and depth-averaged 2D computer models have been used to simulate the interaction of flooded floodplains and river flow (Horritt & Bates, 2002). Unsteady, one-dimensional models such as HEC-RAS (A. Cook & Merwade, 2009; Dyhouse, Hatchett, Benn, & Haestad Methods Inc., 2003; Hick & T., 2005; Horritt & Bates, 2002; Timbadiya, 2011), MIKE11 (Connell et al., 2001; H.-L. Liu, Chen, Bao, & Wang, 2007; Post, a.E. Kinsey-Henderson, Stewart, Roth, & Reghenzani, 2003; Woltemade & Potter, 1994; Yazdi & Salehi Neyshabouri, 2012) and CONCEPTS (Langendoen, 2000; Langendoen & Alonso, 2008; Langendoen & Simon, 2008; Langendoen, Wells, Thomas, Simon, & Bingner, 2009) are robust and computationally efficient when the flow is confined in the channel. Other advantages of 1D models are: the ease to include hydraulic structures in the computational domain, to cover very large regions is computationally

inexpensive, fewer data are required, and less user experience is needed to run the model (Allitt, 2009).

When flow rises above the floodplain, a common approach is to represent the floodplain as a storage area, where the hydrodynamics of the flow is computed using empirical laws to represent the exchange of water between channel and storage cells (Kuiry, Sen, & Bates, 2010); this approach is based on mass exchange, thus no momentum transfer is considered. Two-dimensional models such as TELEMAC-2D (Horritt, Di Baldassarre, Bates, & Brath, 2007; C. A. M. E. Wilson, Stoesser, Olsen, & Bates, 2003), FESWMS (A. Cook & Merwade, 2009) and FLO-2D (O'Brien, Julien, & Fullerton, 1993; Supharatid, 2006) have been used to simulate the complete inundation extent. However, the computational effort of such models can be expensive (Bernini & Franchini, 2013; Zhang, Li, & He, 2014).

The advantages of 1D and 2D approaches are clear, the former for simulating flows confined within the river banks and the latter for simulating the flow propagation over the floodplain. The coupling of both approaches could therefore produce an efficient tool to model the interaction between river flow and inundated floodplains. The selected division of the region can lead to improved and more efficient field data collection, model setup, and computational effort (Allitt, 2009; Bladé et al., 2012; Y. Chen, Wang, Liu, & Zhu, 2012). To model the interaction of the flow within the river channel and that on the floodplain, the coupling of one- and two-dimensional models can be performed in two ways: (1) horizontal coupling (horizontal transfer of mass through vertical interfaces), where the 1D model covers the channel region, while the 2D model covers the left and right overbank regions; and (2) vertical coupling (vertical transfer of mass with horizontal interfaces), where the 1D model covers the bankfull region of the channel and the 2D model covers the overbank (left, central and right) regions.

Based on laboratory experiments of flow in straight, smooth compound channels, Knight and Demetriou (1983) derived the apparent shear stress on the vertical and horizontal interfaces used by the horizontal and vertical coupling approaches. A positive apparent shear stress indicates that the channel flow is retarded by the floodplain flow. The apparent shear stresses on vertical interfaces were always positive; however, apparent shear stresses on horizontal interfaces presented both positive and negative values. Further, apparent shear stresses on the horizontal and vertical interfaces had similar absolute magnitudes.

Prinos and Townsend (1984) developed a relation of the apparent shear stress on a vertical interface based on data from experiments of both straight, smooth and rough compound channels. They showed how the use of the apparent shear stress (or momentum transfer) on the vertical interfaces improved the estimation of the discharge. Furthermore, their analysis also showed that the vertical coupling approach produced better discharge estimates than the horizontal coupling approach.

Turbulence measurements in a straight compound channel by Knight and Shiono (1990) showed that, even for low overbank flow depths, longitudinal vortexes were present across the vertical interface, which are responsible for an important momentum transfer across vertical interfaces.

There has been a considerable effort to develop coupled 1D-2D computer models (e.g., Bladé et al., 2012; Ghostine et al., 2014). Yeh, Huang, Zhang, Cheng, and Lin (2006) developed a numerical model using a horizontal coupling approach, it considers only the transfer of mass and enforced water surface continuity between the main channel and the floodplain; their results showed mass fluxes opposite to the water surface gradient and flow direction in the 1D channel, likely because momentum transfer was not taken into account. Similarly, Bladé et al. (2012), Altinakar, Miglio, and Wu (2008), and Lindenschmidt (2008) presented horizontal coupling approaches with the transfer of mass computed using a weir equation and the momentum transfer being ignored. A variation on the last method is presented by Kuiry et al. (2010), who replaced the weir equation by Manning's equation using water depth differences between the main channel and floodplain. A similar approach is used in the latest version of HEC-RAS (version 5), an example application provided by Brunner (2014) shows that the river appears to act as a barrier to floodplain flows transverse to the main channel.

Bousmar and Zech (1999) developed a horizontal coupling approach, called "Exchange Discharge Model"(EDM), that combines both, mass and streamwise momentum transfer assuming a constant water surface elevation in the main channel and floodplain but a different energy gradient. The advective and diffusive streamwise momentum transfer due to geometrical conditions and turbulent energy was calculated using the conveyance derivative and a mixing length type model, respectively. Proust, Bousmar, Riviere, Paquier, and Zech (2009) improved the EDM approach by relating the advective momentum transfer to streamwise velocity. This horizontal coupling approach is called "Independent Subsections Method"(ISM), and, in contrast to EDM, solves the

mass and streamwise momentum transfer separately. Although ISM shows errors as high as 19% in the floodplain discharge, it reduces the error to around 5% in water depth computation and improves the advective and diffusive momentum transfers.

Fernández-Nieto, Marin, and Monnier (2010) developed a horizontal coupling approach that considers both mass and streamwise momentum transfer. They used tangential velocities instead of streamwise velocities at the interface to determine the advective streamwise momentum transfer. Simulations of flow in a straight, symmetric compound channel agreed well with measurements. Similarly, Morales-Hernández, García-Navarro, Burguete, and Brufau (2013) developed a horizontal-coupling model by conserving mass and streamwise momentum fluxes across the 1D-2D interface and assumed constant water surface elevation and velocity between adjacent elements. This model showed results closer to a fully 2D model with much less computation effort. However, simulations show some discrepancies with experimental results.

Few vertically coupled, 1D-2D computer models exist. D'Alpaos and Defina (1993) developed a vertical-coupling approach that neglected the momentum exchange between the in-channel and overbank flow. It computed the in-channel discharge assuming that the slope and roughness of the floodplain and the channel were the same. Also, Li, Chen, and Mao (2009) developed a numerical model with a vertical-coupling approach, which considered only transfer of mass.

There is a lack of generality in the formulation of mass and momentum transfer terms at the interfaces that connect 1D and 2D model regions for the different coupling methods presented in the literature, necessitating a detailed analysis for each study case and strategy. Herein, a rigorous mathematical derivation for the horizontal and vertical coupling of the 1D and 2D forms of the St. Venant equations is presented. Additionally, it is the first time, to the author's best knowledge, that the magnitude of the mass and momentum exchange terms at the 1D-2D interfaces of both horizontal and vertical coupling approaches are analyzed using experimental data and three-dimensional modeling of overbank flow in a compound meandering channel.

## 2.2 GOVERNING EQUATIONS FOR COUPLING OF 1D AND 2D MODELS

Many textbooks of open-channel flow present the derivation of the 1D and 2D shallow water equations in a Cartesian coordinate system $(x, y)$ (e.g., Liggett, 1994). However, these equations do not include the terms for mass and momentum transfer at the interfaces between 1D and 2D model regions when coupling such models. The sections below present the final equations used in our analysis. Their derivation and definition sketches are provided in the supplemental material accompanying this manuscript. The equations are formulated in a Cartesian coordinate system $(x, y, z)$ with the corresponding velocity components $(u_x, u_y, u_z)$. The $x$-axis is directed downvalley, the $y$-axis is directed across the valley from right to left, and the $z$-axis is directed vertically upward. The derivation of the governing equations assumed that the flow in the 1D model is aligned with the $x$-axis.

### 2.2.1 Horizontal coupling

The conservation of mass for 2D and 1D models is expressed by Eqs. (2.1) and (2.2), respectively. The conservation of momentum for 2D and 1D models is given by Eqs. (2.3) through (2.5), respectively.

$$\frac{\partial h}{\partial t} + \frac{\partial q_x}{\partial x} + \frac{\partial q_y}{\partial y} = 0 \tag{2.1}$$

$$\frac{\partial A}{\partial t} + \frac{\partial Q}{\partial s} + q_n|_{y_r}^{y_l} = 0 \tag{2.2}$$

$$\frac{\partial q_x}{\partial t} + \frac{\partial \bar{u}_x q_x}{\partial x} + \frac{\partial \bar{u}_y q_x}{\partial y} + gh\left(\frac{\partial \zeta}{\partial x} + S_{f_x}\right) = \frac{1}{\rho}\frac{\partial h\bar{\tau}_{xy}}{\partial y} \tag{2.3}$$

$$\frac{\partial q_y}{\partial t} + \frac{\partial \bar{u}_x q_y}{\partial x} + \frac{\partial \bar{u}_y q_y}{\partial y} + gh\left(\frac{\partial \zeta}{\partial y} + S_{f_y}\right) = \frac{1}{\rho}\frac{\partial h\bar{\tau}_{xy}}{\partial x} \tag{2.4}$$

$$\frac{\partial Q}{\partial t} + \frac{\partial UQ}{\partial s} + gA\left(\frac{\partial \zeta}{\partial s} + S_f\right) + \left(\bar{u}_s q_n - \frac{h\bar{\tau}_s}{\rho}\right)\Big|_{y_r}^{y_l} = 0 \tag{2.5}$$

where $Q$ is the flow rate, $A$ is the flow area, $U$ is depth-averaged velocity, and $S_f$ is friction slope in the 1D channel region. The momentum flux terms in Eq. (2.5) at the 1D-2D interface are expressed more generally using subscripts $n$ and $s$ to indicate that velocity, unit discharge, and shear stress are oriented normal ($n$) or along ($s$) the 1D-2D interfaces located at the left ($y_l$) and right ($y_r$) channel margins, respectively. Further, $t$ is time, $h$ is flow depth, $q = \bar{u}h$ is unit discharge (in $x$, $y$ or $n$ directions), $\bar{u}$ is depth-averaged velocity (in $x$, $y$ or $s$ directions), $g$ is gravitational acceleration, $\zeta$ is water surface elevation, $S_f$ is friction slope (in $x$ or $y$ directions), $\rho$ is water density, and $\tau_{xy}$ is depth-averaged lateral Reynolds shear stress. The 1D momentum transfer term (last term on the left-hand side of Eq. (2.5), termed $M$ hereafter) comprises advective transport, $M_a = \bar{u}_s q_n$, and diffusive transport, $M_d = -h\bar{\tau}_s/\rho$, of momentum. Note that the mass and momentum transfer terms, $q_n$ and $M$, in the 1D equations are boundary conditions for the 2D equations.

### 2.2.2 Vertical coupling

The mass conservation for 2D and 1D models is expressed by Eqs. (2.6) and (2.7), respectively. The momentum conservation equations for 2D and 1D models are given by Eqs. (2.8) to (2.10), respectively.

$$\frac{\partial h}{\partial t} + \frac{\partial q_x}{\partial x} + \frac{\partial q_y}{\partial y} = \epsilon \frac{\partial d}{\partial t} \tag{2.6}$$

$$\frac{\partial Q}{\partial s} = -B_{z_t} \frac{\partial \tilde{d}}{\partial t} \tag{2.7}$$

$$\frac{\partial q_x}{\partial t} + \frac{\partial \bar{u}_x q_x}{\partial x} + \frac{\partial \bar{u}_y q_x}{\partial y} + gh\left(\frac{\partial \zeta}{\partial x} + (1-\epsilon)S_{f_x}\right) - \epsilon\left(u\frac{\partial d}{\partial t}\right)\Big|_{z_b} = \frac{1}{\rho}\left[\frac{\partial h\bar{\tau}_{xy}}{\partial y} - \epsilon\tau_x|_{z_b}\right] \tag{2.8}$$

$$\frac{\partial q_y}{\partial t} + \frac{\partial \bar{u}_x q_y}{\partial x} + \frac{\partial \bar{u}_y q_y}{\partial y} + gh\left(\frac{\partial \zeta}{\partial y} + (1-\epsilon)S_{f_y}\right) - \epsilon\left(u_y\frac{\partial d}{\partial t}\right)\Big|_{z_b} = \frac{1}{\rho}\left[\frac{\partial h\bar{\tau}_{xy}}{\partial x} - \epsilon\tau_y|_{z_b}\right] \tag{2.9}$$

$$\frac{\partial Q}{\partial t} + \frac{\partial UQ}{\partial s} + gA\left(\frac{\partial \zeta}{\partial s} + S_f\right) + \left[B\left(\tilde{u_s}\frac{\partial \tilde{d}}{\partial t} - \frac{\tilde{\tau_s}}{\rho}\right)\right]\Big|_{z_t} = 0 \tag{2.10}$$

where $d$ is the transfer of mass through the horizontal interface and is represented by a vertical column of water with length $d$, $z_b$ is bottom surface elevation of a model region, $z_t$ is top surface elevation of a model region, $\tau$ is boundary shear stress (in $x$, $y$ or $s$ directions), $B$ is bank-full channel width, and the tilde indicates that a parameter is averaged over the width of the horizontal 1D-2D interface separating 1D and 2D regions. The coefficient $\epsilon$ in the 2D St. Venant equations (2.6), (2.8) and (2.9) is zero in the floodplain area and one in the zone above the channel (1D region). Similar to the horizontal coupling approach, the momentum transfer comprises advection, $M_a = Bu_s\partial d/\partial t$, and diffusion, $M_d = -B\tau_s/\rho$, transport terms. In order to conserve mass and momentum across the combined 1D and 2D interface, the laterally integrated mass and momentum exchange terms in the 2D equations (Eqs. 2.6, 2.8, and 2.9) must equal the mass and momentum exchange terms in the 1D equations (Eqs. 2.7 to 2.10).

## 2.3 ANALYSIS OF MASS AND MOMENTUM TRANSFER TERMS FOR HORIZONTAL AND VERTICAL COUPLING METHODS

### 2.3.1 Three-dimensional flow structure in a compound channel

The governing equations for horizontal and vertical coupling of 1D and 2D hydrodynamic models presented above include mass and momentum transfer terms at the 1D-2D interface. The magnitude of these terms could indicate the suitability of each coupling approach (horizontal or vertical). These terms have been studied extensively for straight compound channel flow (Knight & Demetriou, 1983; Knight & Sellin, 1987; Knight & Shiono, 1990; Myers & Brennan, 1990; Wormleaton & Merrett, 1990); however, detailed analysis of their magnitudes and distributions for a meandering compound channel are lacking. Here, the transfer terms were evaluated for test "R2-rectangular" of the experimental study on overbank flow in a compound meandering channel by Shiono and Muto (1998). The rectangular, meandering channel has a width of 150 mm, a depth of 53 mm, and a sinuosity of 1.37. The floodplain has a width of 1.2 m, a length of 10.8 m, and a longitudinal slope of 0.001. The average ratio of the floodplain width to the meandering channel width is 8.

The discharge was 20 L/s, which resulted in a total flow depth of 106 mm and a relative flow depth $D_r = 0.50$, defined as the ratio of the floodplain water depth to the main channel water depth.

Shiono and Muto (1998) did not compute the mass and momentum transfer terms; however, experimental measurements obtained directly from Shiono and Muto were used to calculate the transfer terms at the 1D-2D interfaces. Due to typical limitations in the measurement equipment, it was not possible to get the complete, detailed flow structure, especially near walls and corners.

Therefore, a three-dimensional (3D) numerical model built in FLOW-3D was used to describe the complex flow structure produced along the 1D-2D interfaces in the horizontal and vertical coupling methods by the interaction between the flow in the main channel and the outer bank regions (Fig. 2a). FLOW-3D solves the 3D RANS equations using finite-difference (or finite-volume) approximations and the free surface is resolved with the volume-of-fluid technique on a fixed Eulerian rectangular grid (FLOW Science, 2008). The renormalized group $k$-$\varepsilon$ model was used as the turbulence closure model due to its capacity to reproduce the general pattern of curved flow in meandering channels (Abad, Buscaglia, & Garcia, 2008).

Flow-3D was setup to simulate the 10.8 m long by 1.2 m wide flume using $593 \times 63 \times 16$ elements with a size of 2 cm $\times$ 2 cm $\times$ 1 cm. The measured discharge was imposed at the upstream boundary, while the measured flow depth was imposed at the downstream boundary. The model was validated against the measured water depth, depth-averaged velocity patterns (see Shiono & Muto, 1998, Table 2 and Fig. 4c) and flow parameters related to the interface between the flow in the channel and the floodplain. Measurements were provided by Shiono and Muto.

Figures 2b and 2c show the measured and simulated depth-averaged velocity patterns along a half meander wavelength, respectively. Although the numerical model presents similar velocity patterns to the measured ones, the magnitude is slightly larger on the floodplain and slightly smaller in-channel. Figures 3 to 5 show the streamwise mass flux per unit of mass and length, depth-average shear stress, streamwise advective momentum transfer per unit of mass and unit area, and lateral momentum transfer per unit of mass and unit area computed from experimental data (normal velocities and shear stress on interfaces). Figures 7 to 9 show the same parameters obtained from the Flow-3D simulation. Comparison of both sets of flow parameters shows the same trends and similar magnitudes between experimental and modeled flow parameters at the interfaces, except

for the shear stress. A discussion between experimental and modeled terms is presented in section 2.4.3.

### 2.3.2 Model results at the horizontal and vertical interfaces

In both coupling approaches the 1D flow direction $s$ is aligned with the channel centerline; the transverse direction $n$ is normal to $s$ increasing from the right to the left bank (see Fig. 6b). Figure 6a shows the simulated velocity vectors and contours of shear stress magnitude at the left interface.

The highest shear stresses on the interfaces are found downstream of the bend apex. Figure 6b shows the velocity vectors and the contours of shear stress magnitude at the right interface. A significant volume of fluid with higher velocities is transferred across both vertical 1D-2D interfaces. This indicates that not only mass, but also momentum transfer terms should be considered in the horizontal coupling method. Figure 6c shows the velocity vectors and the shear-stress contours on the bankfull interface between 1D and 2D model regions. The velocity vectors show that fluid is transferred between the inbank channel and overbank regions. It is important to note that, on average, the fluid velocities at the 1D-2D horizontal interface are smaller than those at the vertical 1D-2D interfaces.

### 2.3.3 Horizontal coupling method: mass and momentum transfer terms

Figures 7 and 8 show the simulated mass and momentum transfer parameters for the horizontal coupling method along the left and right interfaces, respectively. These figures show the results for a complete meander wavelength starting at the streamwise coordinate $s = 0.0$ m and ending at $s = 2.53$ m (see Figs. 2a, 6a and 6b).

Figure 7a shows that fluid mass enters the channel in the upstream half of the bend and leaves the channel along the downstream half. The mass transfer is more clearly observed in Figure 6b. Further, the mass flux distribution along the interfaces is nearly symmetrical.

Figures 7a and 8a show that the streamwise depth-averaged shear stress, $\bar{\tau}_s$, along the 1D-2D interfaces is higher immediately downstream of the bend apex. The streamwise depth-averaged shear stresses indicate acceleration of fluid from the floodplain regions into the channel region. The streamwise advective momentum transfer per unit of mass and unit area term, $M_s = u_s u_n$, along the

left interface is negative (positive) when the momentum is transferred from the floodplain (main channel) into the main channel (floodplain) region; along the right interface it is the opposite (Figs. 7a and 8a). The lateral advective momentum transfer per unit of mass and unit area term, $M_n = u_n^2$, along the left and right interfaces is slightly higher than the advective streamwise momentum transfer per unit of mass and unit area term. This condition shows the need to consider the lateral momentum transverse term in the horizontal coupling approach.

### 2.3.4 Vertical coupling method: mass and momentum transfer terms

Figure 9 shows the mass and momentum transfer terms for the vertical coupling method along the horizontal interface at the bankfull flow elevation. For the vertical coupling approach, the transfer term $\partial d/\partial t$ in the 1D mass conservation equation (Eq. 2.7) represents the velocity of the fluid moving from the 1D into the 2D model region, which is also equal to the channel width-averaged vertical velocity, $\tilde{u}_{z_t}$, at the bankfull interface. Figure 9a shows that the streamwise distribution of $\tilde{u}_{z_t}$ is irregular. The spatial distribution of $u_{z_t}$ exhibits zones of high outflow and high inflow at the same cross section (see Fig. 9b). The vertical velocities show the secondary flow in the meandering channel, flow interactions between the in-channel and overbank regions, and the 3D nature of the flow. Note, a 2D model of the channel region cannot describe such flow characteristics.

The streamwise shear stresses (Fig. 9a) are generally positive, indicating higher overbank velocities than in the channel. The width-averaged streamwise advective momentum transfer per unit of mass and area ($M_s = u_s u_{z_t}$) is shown in Figure 9a. The spatial distribution of $M_s$ is plotted in Figure 9d, which shows values near zero everywhere except along the banks near the bend apices. The spatial distribution of the vertical advective momentum transfer per unit of mass and area ($M_z$) is plotted in Figure 9e, and its laterally-integrated value is shown in Figure 9a.

## 2.4 DISCUSSION

The equations for horizontal coupling (Eqs. 2.1 to 2.5) are quite similar to the equations presented by Fernández-Nieto et al. (2010), except that the turbulent diffusion terms are not neglected. To the

knowledge of the authors, the full equations for the vertical coupling (Eqs. 2.6-2.10) are presented for the first time in the hydraulic literature. The advantage of the horizontal coupling over the vertical coupling is the more intuitive grid independence (Fernández-Nieto et al., 2010). Fernández-Nieto et al. (2010) proved that the mesh independence between 1D and 2D model regions does not affect the accuracy of results. One disadvantage of the horizontal coupling is the fact that the 1D model cannot provide the full set of boundary conditions to the 2D model (Gejadze & Monnier, 2007).

Comparing the set of equations for the horizontal (Eqs. 2.1-2.5) and vertical (Eqs. 2.6-2.10) coupling methods, the implementation of the solution for the vertical case is straightforward since the mass and momentum transfer are explicitly accounted for through additional terms in both 1D and 2D governing equations, whereas they are boundary conditions for the 2D model in the horizontal coupling method.

### 2.4.1 Mass transfer

Based on the three-dimensional simulation results presented here, the mass flux per unit mass and length on the horizontal bankfull interface in the vertical coupling method is of the order of $10^{-3}$ $m^2s^{-1}$, while the left and right vertical interfaces in the horizontal coupling method present mass fluxes per unit mass and length of order $10^{-2}$ $m^2s^{-1}$. As these flux terms have to be partially approximated, the influence of an error in these terms will have less impact in the flow solution for the vertical-coupling methodology than for the horizontal-coupling method.

### 2.4.2 Momentum transfer

In general, coupling of 1D and 2D models must consider the momentum transfer at the interfaces of both regions because "the primary flow field is considerably modified by the lateral and vertical momentum transfer between regions of different depths" (Knight & Demetriou, 1983). The presence of vortices between the shallow and deep sections indicates momentum transfer between the main channel and the floodplain channel (Knight & Demetriou, 1983). This is further verified by the observations of Shiono and Muto (1998) in a laboratory meandering channel with overbank flow, regarding the interaction between the flows in the main channel and the floodplain to produce shear stresses that modify the inbank secondary flow.

In the experiments of flow in a simple, straight prismatic compound channel performed by Knight and Demetriou (1983), the shear stresses at the vertical interface between the main channel and the floodplain were larger than the boundary shear stress acting on the floodplain. Thus, these shear stresses acting on the 1D-2D interface must always be considered when using a horizontal-coupling method.

The momentum transfer terms have historically been denoted as apparent shear stress $\tau_a$ (Knight & Demetriou, 1983; Prinos & Townsend, 1984). The apparent shear stress can be calculated as $\tau_a = \tau_{sn} - \rho M_s$ for vertical interfaces, and $\tau_a = \tau_{sz} - \rho M_s$ for the horizontal interface. For the meandering compound channel presented here, the vertical interfaces of the measurements and the Flow-3D model present a range of $-60 < \tau_a < 60$ Pa (Figs. 7 and 8), while for the horizontal interface the range is $-18 < \tau_a < 18$ Pa (Fig. 9). These values for a meandering channel are much larger than the mean values measured by Knight and Demetriou (1983) and Prinos and Townsend (1984) for straight compound channels,s showing that meandering channels present more interaction between the channel and floodplains for overbank flow conditions.

Knight and Demetriou (1983) found mean apparent shear stresses on vertical and horizontal interfaces equal to 0.025 Pa and 0.05 Pa, respectively, for a straight compound channel with bed slope equal to $9.66 \times 10^{-4}$ m/m, $D_r = 0.506$ and floodplain to channel width of 4. Prinos and Townsend (1984) found mean apparent shear stresses on vertical interfaces ranging between 0.025 Pa to 0.035 Pa for Manning $n$ values varying between 0.011 to 0.022, respectively, for a straight compound channel with bed slope equal to $3 \times 10^{-4}$ m/m, $D_r = 0.329$ and floodplain to channel width of 3.5. Applying the apparent shear stress relationship for a straight channel of Prinos and Townsend (1984) to the meandering channel modeled here, yields an apparent shear stress less than one third of the smallest value calculated by the model. Clearly, a meandering channel presents more complex overbank flow dynamics at the transition between the main channel and floodplain.

van Prooijen, Battjes, and Uijttewaal (2005) found that diffusive momentum transfer was one order of magnitude greater than advective momentum transfer. Conversely, our findings show that the advective momentum transfer ($M_s$ and $M_n$) in meandering channels is two orders of magnitude higher than the diffusive momentum transfer (Figs. 7 and 8). Similarly, using a modification of the Shiono and Knight (1991) analytical model that accounts for the exchange of secondary flows in compound meandering channels, Ervine, Babaeyan-Koopaei, and Sellin (2000) found that the

momentum transfer in a meandering compound channel was approximately an order of magnitude larger than that in a straight channel, which was primarily due to the bulk exchange of fluid between main channel and floodplain.

D'Alpaos and Defina (2007) neglected the momentum transfer term in the 1D momentum equation of their model using a vertical coupling approach as it was assumed to be small relative to the channel boundary friction. It is therefore of interest to compare the momentum transfer term ($B\tilde{u_s}\partial\tilde{d}/\partial t - B\tilde{\tau_s}/\rho$) in the 1D momentum equation (Eq. 2.10) to channel bottom and bank resistance $gAS_o$, where $S_o$ is the channel bottom slope. For convenience we replaced the friction slope with channel slope, which varied between 0.0005 to 0.001 for experiment R2-rectangular in Shiono and Muto (1998). We define the following momentum exchange ratios (MERs): MER = $(B\tilde{u_s}\partial\tilde{d}/\partial t - B\tilde{\tau_s})/(\rho gAS_0)$, Adv. MER = $[B\tilde{u_s}\partial\tilde{d}/\partial t]/[\rho gAS_0]$ (advective MER), Diff. MER = $-B\tilde{\tau_s}/[\rho gAS_0]$ (diffusive MER). These ratios are plotted in Figure 10, assuming $S_0 = 0.001$. Although this assumption yields smaller ratios, results show that the momentum exchange between the inbank and the overbank flow is not negligible. A positive or negative MER means that the 1D inbank flow is decelerating or accelerating by the momentum exchange through the interface, respectively.

The Adv. MER distribution is irregular, reflective of the vertical velocity ($w_s$) distribution at the interface. The Diff. MER distribution indicates acceleration of the 1D flow near the bends and deceleration near the inflection points. Figure 10 shows that the diffusive momentum transfer is negligible because it is an order of magnitude less than the advective momentum transfer. Further, the simulation results show that MER varies from -2.5 to 1.5. This variation is equivalent to a change in the Manning roughness coefficient of about 40%. Similar to the horizontal-coupling approach, the interface exchange terms must be considered in the vertical-coupling approach.

For comparison, Figure 11 shows the MER = $(\rho\bar{u}_s q_n - h\bar{\tau}_s)/(\rho gAS_0)$ at both left and right interfaces for the horizontal coupling method. The MER values in the horizontal coupling approach are one order of magnitude larger (compare Figure 10 to Figure 11) than those in the vertical coupling approach. The difference in an order of magnitude indicates that the same error percentage approximating the momentum transfer terms will have less impact if a vertical approach is used. The high MER values indicate the importance of momentum transfer in the horizontal coupling approach to flow hydrodynamics.

Based on the three-dimensional simulation results presented here, it is found that the streamwise shear stresses (Fig. 9c) are in general larger than those acting on the vertical 1D-2D interfaces in the horizontal coupling method. Also, the results show that the values of the vertical advective momentum transfer through the horizontal interface is one order of magnitude smaller than the lateral advective momentum transfer through the vertical interfaces (compare Figs. 7e, 8e, and 9e).

To derive the one-dimensional momentum equation it was assumed that cross-stream variations of flow variables at the upper surface $z_t$ (i.e., horizontal interface in the vertical coupling method), were negligible. Figure 12 compares the vertical advective momentum transfer per unit of mass and length over the horizontal bankfull interface in the vertical coupling approach ($B\,M_s = -\int_{y_r}^{y_l}(u_s\,\partial d/\partial t)|_{z_t}\,dy$) versus that approximated using width-averaged values ($[-B\,\tilde{u}_s\,\partial\tilde{d}/\partial t]_{z_t}$), which is included in Eq. (2.10). In the straight portions (crossovers) between bends these terms are similar, however $|B\,M_s| \gg |-B\,\tilde{u}_s\,\partial\tilde{d}/\partial t|$ in the bends. Figure 9(d) shows that the spatial distribution of $u_s u_z$ is fairly uniform except in the bends. A vertical coupling model could use a correction factor to account for this non-uniformity.

### 2.4.3 Numerical modeling implications

Comparison between experimental and modeled hydraulic parameters at the interfaces shows similar patterns, they follow the perturbations created by the bends in the channel; however, magnitude ranges are different. Velocity gradients at the interfaces have similar patterns and magnitudes. The ranges of flux of mass and momentum at the interfaces are more similar in magnitude for the vertical coupling than for the horizontal coupling approach. Diffusive momentum transfer shows larger differences between experimental and modeled magnitudes; especially on the horizontal interface, where flow across this interface is much more complex. Hence, the $k$-$\epsilon$ model may not be accurate enough to compute the interface diffusive momentum exchanges in a compound meandering channel.

For both coupling approaches, the transverse velocity can be computed directly from the mass transfer term; the mass transfer term values are obtained when the system of mass and momentum equations are solved. We can use the projected velocities from the 1D and 2D solution to compute an average velocity parallel to an interface. The advective momentum transfer terms are computed

using the transverse and parallel velocities at the interface. The difference (i.e., gradient) of the projected velocities from the 1D and 2D solution can be used to compute the shear stress acting on the interface. The above suggestions complete the closure to solve the coupling approaches.

## 2.5 CONCLUSIONS

A rigorous derivation of the depth-averaged (2D) and cross section-averaged (1D) Reynolds-Averaged Navier-Stokes equations for the coupled solution (horizontal and vertical) of overbank flow in compound channels was performed. The horizontal coupling method combines the depth-averaged 2D floodplain flow model at both sides of a 1D cross section-averaged model for the flow in the main channel. The vertical coupling method combines a depth-averaged 2D model for the flow along the overbank region with a 1D cross section-averaged model for the flow in the channel inbank region.

In the horizontal coupling method, the mass transfer between the 1D and 2D model regions is the lateral unit discharge at the interface, while in the vertical coupling method, the mass transfer is given by the vertical velocity at the interface. The momentum transfer between 1D and 2D models is represented by two terms, an advective momentum transfer due to the exchange of mass, and a diffusive momentum transfer due to the shear stresses acting on the interface between 1D and 2D model regions. The magnitudes of these exchange terms were evaluated for overbank flow in a compound meandering channel.

Methods that couple 1D and 2D flow models solve the main flow variables (discharge, depth-averaged velocities, water depth) within the 1D or 2D regions, and approximate the values at the interfaces by constituent equations based on the main variables and empirical or standard formulations. The approximated values of the variables at interfaces have a direct impact on the modeled main channel flow. The transfer terms (mass and momentum) for the vertical-coupling method were smaller than those for the horizontal-coupling method. Therefore, for the case of meandering channels with overbank flows, the errors introduced at the model interface will have a smaller effect on the overall flow characteristics (i.e., discharge, water depth, etc.).

In the horizontal-coupling approach, the streamwise and lateral advective momentum transfer terms were smaller in bends and larger in the straight portion between bends. On the contrary, the vertical-coupling approach presented a fairly constant width-averaged advective momentum transfer magnitude along the full meander wavelength, whereas the shear stress was similar to that of the horizontal-coupling method (maximum values in the bends and close to zero in the cross-overs). Vertical-coupling methods can take advantage of this behavior by simplifying the numerical solution approach.

Vertical velocities at the horizontal interface for the vertical-coupling approach were higher near the bends of the meandering channel, see Figure 9. This vertical flow generates turbulence and flow resistance near the bends, which 2D codes are not able to simulate but could be incorporated by locally increasing the flow resistance parameters.

Future research should compare 1D, 2D, and 1D-2D horizontal and vertical coupling models to study their accuracy in modeling overbank flow in a meandering compound channel. This comparison will help to select the appropriate model approach to simulate floods in natural streams where non-straight alignment is common. Few 1D-2D horizontal-coupling and no vertical-coupling models incorporate all transfer terms presented here. Therefore, it is necessary to develop a 1D-2D vertically-coupled model with all transfer terms and compare it to a complete horizontally-coupled model. Alternatively, a 3D model can be used with fewer cells in strategic locations, that is coarse vertical resolution, to evaluate coupling approaches.

## 2.6 ACKNOWLEDGMENTS

This work was performed under Specific Cooperative Agreement No. 405882 between the Department of Civil and Environmental Engineering of the University of Pittsburgh and the U.S. Department of Agriculture, Agricultural Research Service, National Sedimentation Laboratory, Oxford, MS.

I want to give special thanks to Dr. Shiono and Dr. Muto who provided the experimental measurements of the compound meandering channel discussed here. The information was crucial

in the development of this paper since it helped to validate the FLOW-3D model and to clarify the relations between interface terms.

## 2.7 NOTATION

$\eta$ = representation of the water free surface whether the flow is inbank or overbank (m)

$\tau_{ij}$ = Reynolds stress tensor, $i$ and $j$ stand for $x$, $y$, $z$ (Pa)

$\tau_x, \tau_y$ = shear stresses acting on the top and bottom surfaces in $x$- and $y$-direction (Pa)

$\rho$ = density of the water (kg $m^{-3}$)

$\zeta$ = water surface elevation (m)

$A$ = cross-sectional area to the flow in the in-channel region ($m^2$)

$B$ = channel top width (m)

$d$ = mass flux per unit area and density at the interface of 1D-2D regions for vertical coupling (m)

$g$ = gravitational acceleration (m $s^{-2}$)

$h$ = water depth (m)

$M$ = momentum transfer at the interface of 1D-2D regions, per unit streamwise length and density ($m^3$ $s^{-2}$)

$M_a, M_d$ = advective and diffusive components of M, respectively ($m^3 s^{-2}$)

$Q$ = flow discharge within the channel ($m^3$ $s^{-1}$)

$q_x, q_y$ = unit flow discharge in $x$ and $y$ ($m^2$ $s^{-1}$)

$S_f$ = friction slope (-)

$U$ = cross-section average velocity in the 1D region weighted by unit discharge $U = \int_{y_r}^{y_l} \bar{u_s} q_s dy / Q$ (m $s^{-1}$)

$u_x, u_y, u_z$ = velocities in $x$, $y$ and $z$, respectively (m)

$z_{fp}$ = floodplain elevation at the top river-bank (m)

$z_t, z_b$ = top and bottom elevation, respectively, for the 1D and 2D model regions (m)

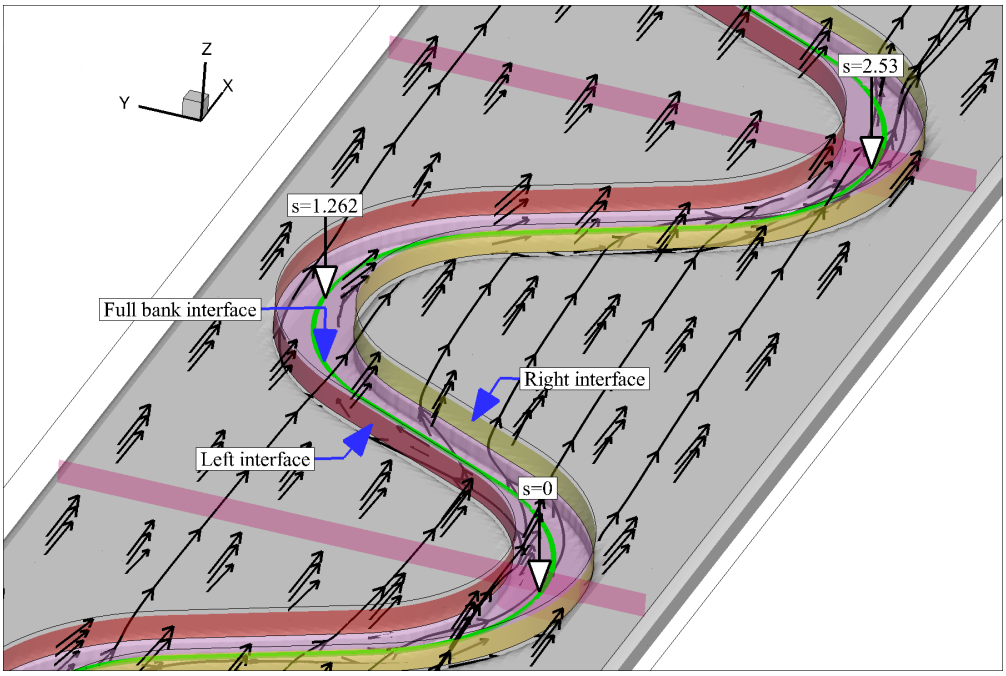


(a) Three-dimensional complex flow structure showing the interaction between the inbank and overbank regions, which are separated by left and right vertical interfaces for the horizontal coupling approach and a horizontal bankfull interface for the vertical-coupling approach.

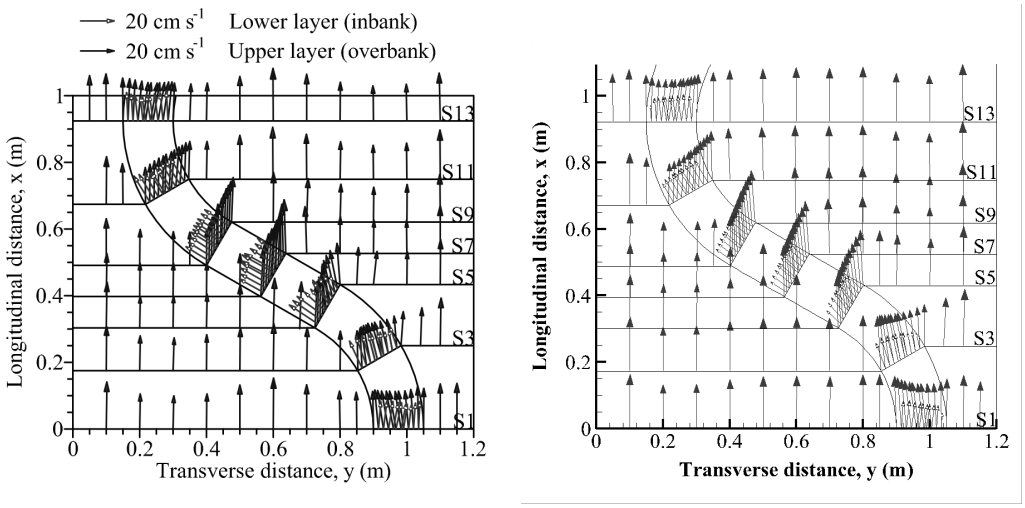


(b) Depth-averaged measured velocities in the inbank and overbank layers (Shiono & Muto, 1998)

(c) Depth-averaged simulated velocities in the inbank and overbank layers.

Figure 2: Numerical simulation of the flow in an experimental compound meandering channel with overbank flow (Shiono & Muto, 1998).

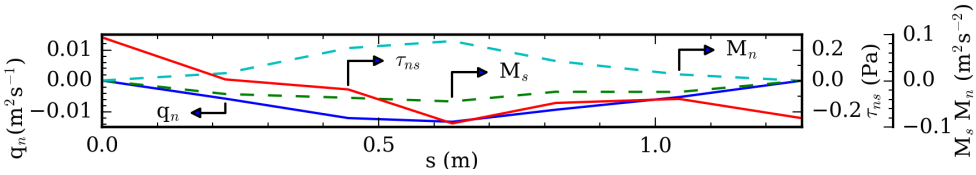


(a) Streamwise distributions of transverse mass flux per unit of mass and length ($q_n$), streamwise depth-averaged shear stress ($\bar{\tau}_s$), streamwise advective momentum transfer per unit of mass and unit area ($M_s = u_s u_n$) and lateral advective momentum transfer per unit of mass and unit area ($M_n = u_n u_n$).

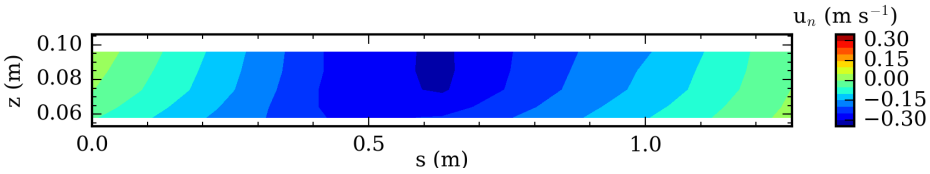


(b) Distribution of $u_n$ over the vertical interface.

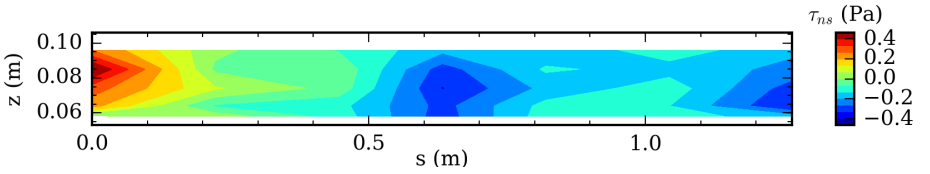


(c) Distribution of $\bar{\tau}_{ns}$ over the vertical interface.

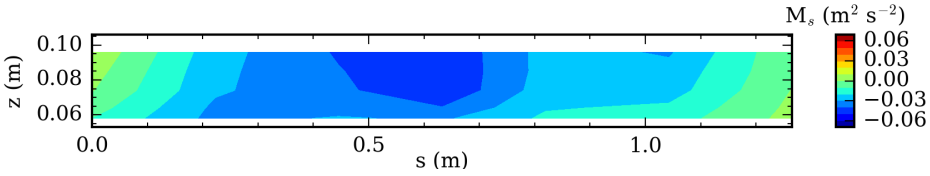


(d) Distribution of $(u_s u_n)|_{y_l}$ over the vertical interface.

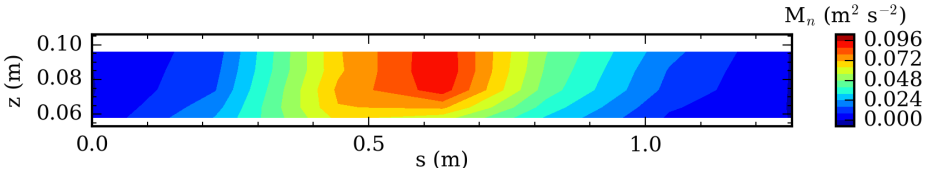


(e) Distribution of $(u_n u_n)|_{y_l}$ over the interface.

Figure 3: Mass and momentum transfer terms at the left interface for the horizontal-coupling method along a half meander wavelength derived from the measured data (Shiono & Muto, 1998). Note that the vertical extent of the interface ranges from the bankfull flow elevation to the free surface.

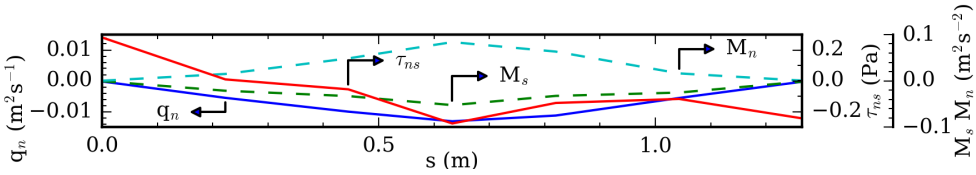


(a) Streamwise distributions of transverse mass flux per unit of mass and length ($q_n$), streamwise depth-averaged shear stress ($\bar{\tau}_s$), streamwise advective momentum transfer per unit of mass and unit area ($M_s = u_s u_n$) and lateral advective momentum transfer per unit of mass and unit area ($M_n = u_n u_n$).

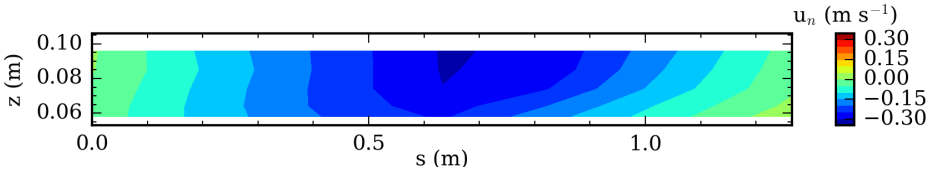


(b) Distribution of $u_n$ over the interface.

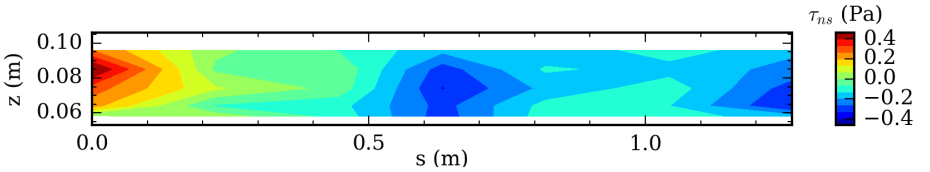


(c) Distribution of $\bar{\tau}_{ns}$ over the interface.

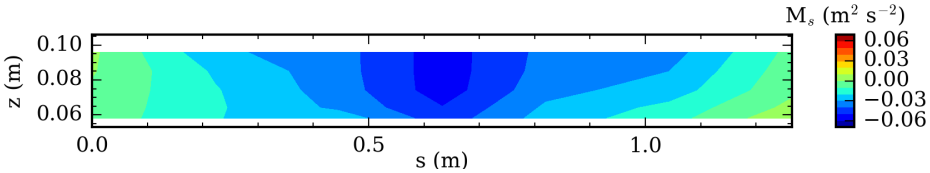


(d) Distribution of $(u_s u_n)|_{y_r}$ over the interface.

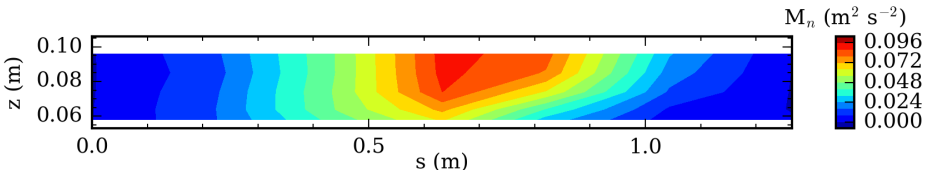


(e) Distribution of $(u_n u_n)|_{y_r}$ over the interface.

Figure 4: Mass and momentum transfer terms at the right interface for the horizontal-coupling method along a half meander wavelength derived from the measured data (Shiono & Muto, 1998). Note that the vertical extent of the interface ranges from the bankfull flow elevation to the free surface.

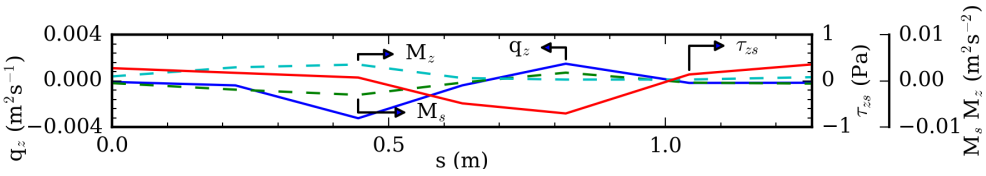


(a) Streamwise distributions of vertical mass flux per unit of mass and length ($q_z = u_z B$), streamwise shear stress ($\tilde{\tau}_{sz}$), streamwise advective momentum transfer per unit of mass and area ($M_s = u_s u_z$), and vertical advective momentum transfer per unit of mass and area ($M_n = u_n u_z$).

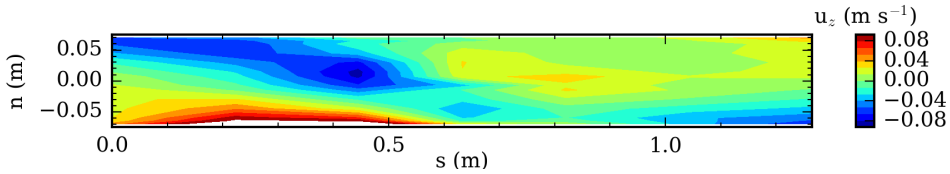


(b) Spatial distribution of $u_x|_{z_t}$.

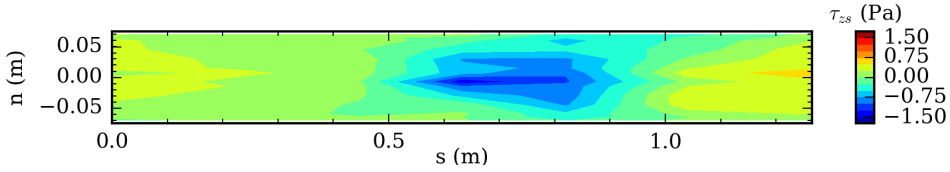


(c) Spatial distribution of $\tau_s$.

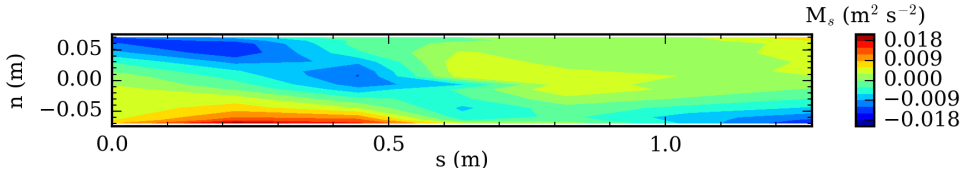


(d) Spatial distribution of $(u_s u_z)|_{z_t}$.

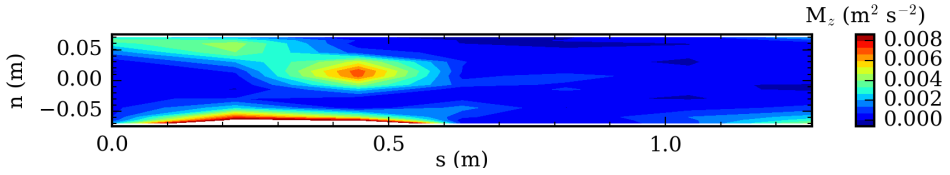


(e) Spatial distribution of $(u_z u_z)|_{z_t}$.

Figure 5: Mass and momentum transfer terms for the vertical-coupling method along a half meander wavelength derived from the measured data (Shiono & Muto, 1998).

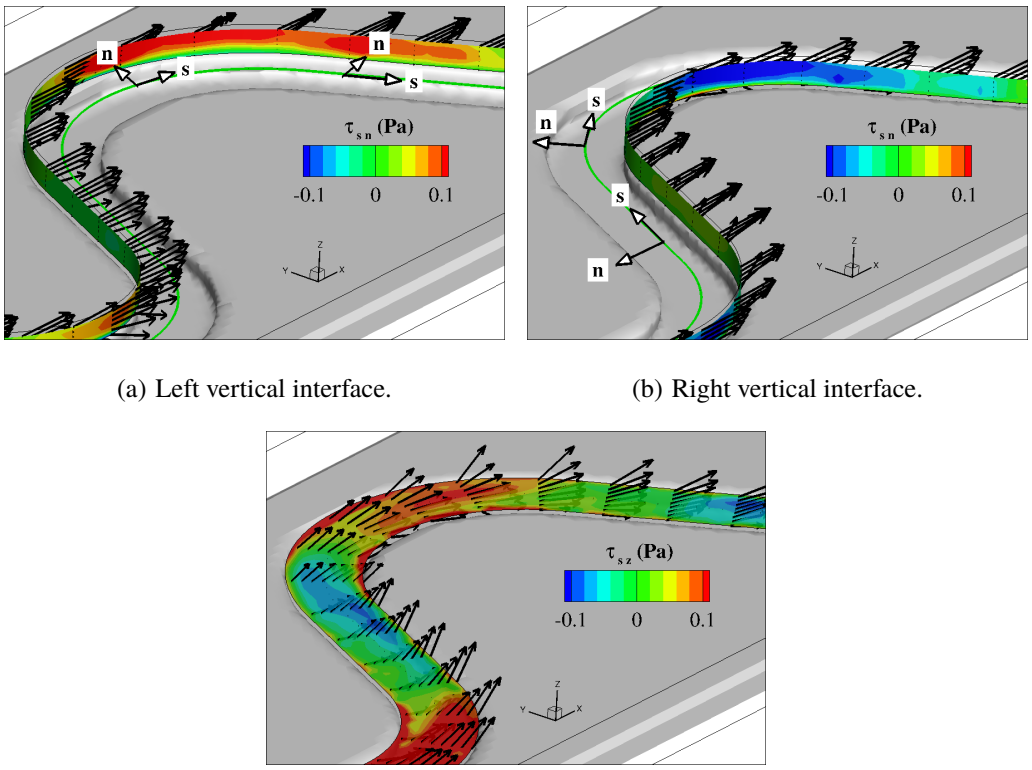


(a) Left vertical interface.

(b) Right vertical interface.

(c) Horizontal bankfull interface.

Figure 6: Three-dimensional view of the simulated velocity vectors and shear stresses at the horizontal and vertical interfaces between inbank and overbank regions of the meandering compound channel experiment "R2-rectangular" of Shiono and Muto (1998).

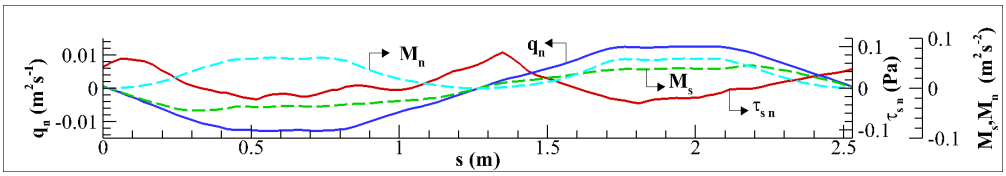


(a) Streamwise distributions of transverse mass flux per unit of mass and length ($q_n$), streamwise depth-averaged shear stress ($\bar{\tau}_s$), streamwise advective momentum transfer per unit of mass and unit area ($M_s = u_s u_n$) and lateral advective momentum transfer per unit of mass and unit area ($M_n = u_n u_n$).

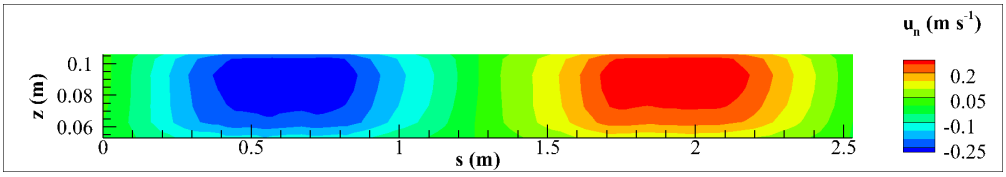


(b) Distribution of $u_n$ over the interface.

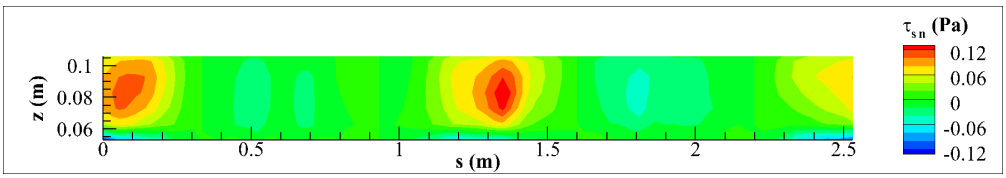


(c) Distribution of $\bar{\tau}_{sn}$ over the interface.

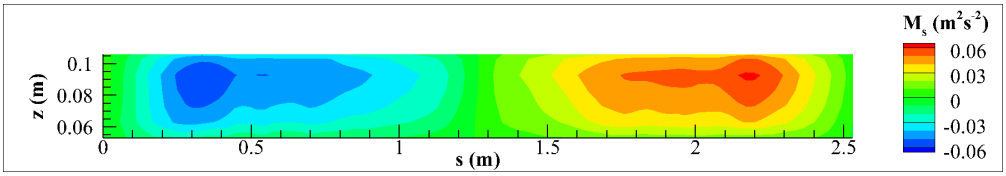


(d) Distribution of $(u_s u_n)|_{y_l}$ over the interface.

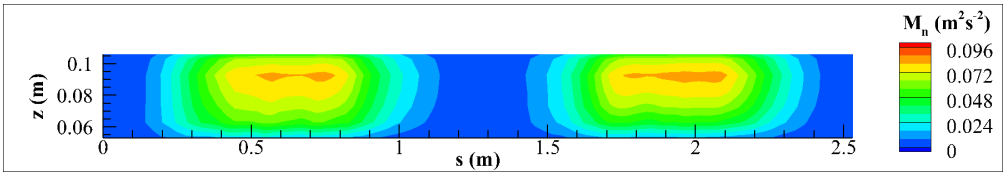


(e) Distribution of $(u_n u_n)|_{y_l}$ over the interface.

Figure 7: Mass and momentum transfer terms at the left interface for the horizontal-coupling method along a complete meander wavelength derived from the Flow-3D simulation. Note that the vertical extent of the interface ranges from the bankfull flow to the free surface elevations.

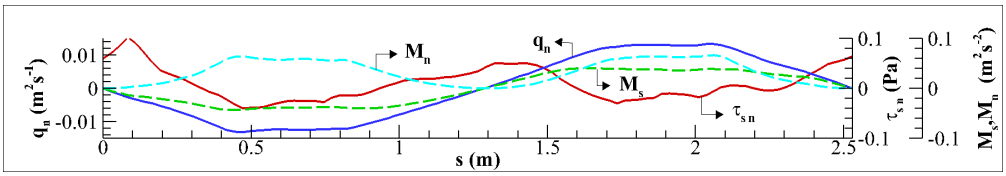


(a) Streamwise distributions of transverse mass flux per unit of mass and length ($q_n$), streamwise depth-averaged shear stress ($\bar{\tau}_s$), streamwise advective momentum transfer per unit of mass and unit area ($M_s = u_s u_n$) and lateral advective momentum transfer per unit of mass and unit area ($M_n = u_n u_n$).

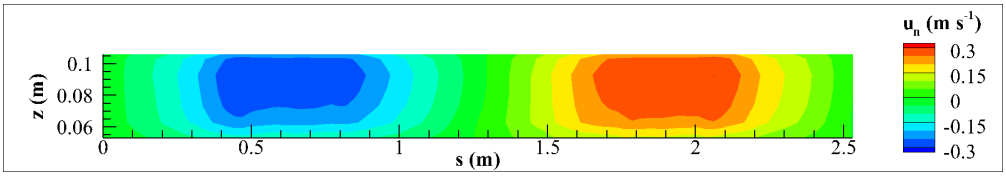


(b) Distribution of $u_n$ over the interface.

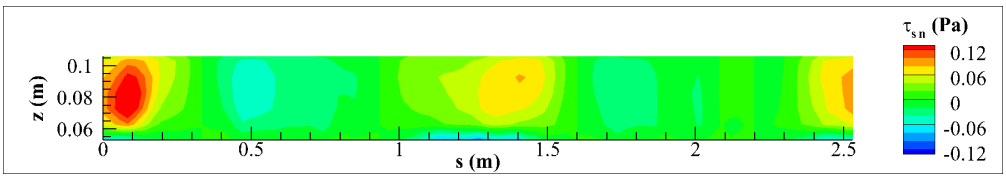


(c) Distribution of $\bar{\tau}_{sn}$ over the interface.

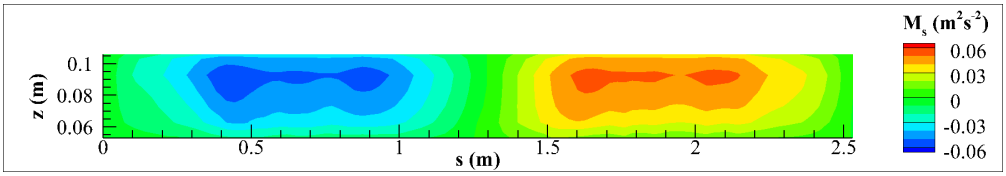


(d) Distribution of $(u_s u_n)|_{y_r}$ over the interface.

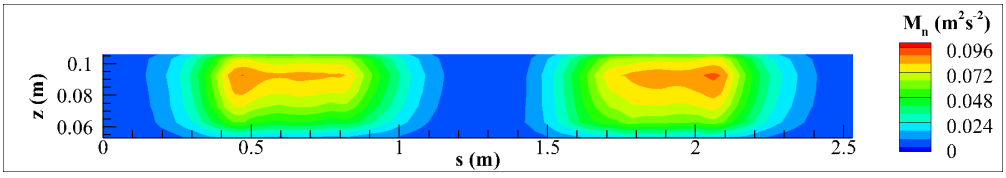


(e) Distribution of $(u_n u_n)|_{y_r}$ over the interface.

Figure 8: Mass and momentum transfer terms at the right interface for the horizontal-coupling method along a half meander wavelength derived from the Flow-3D simulation. Note that the vertical extent of the interface ranges from the bankfull flow elevation to the free surface.

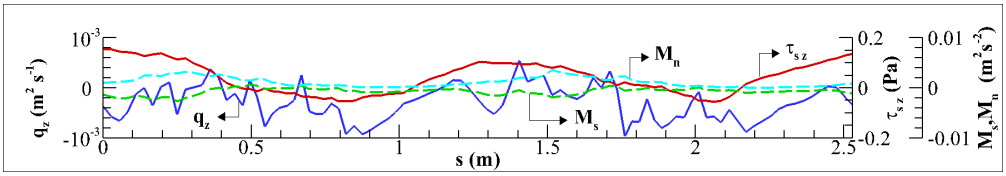


(a) Streamwise distributions of vertical mass flux per unit of mass and length ($q_z = u_z B$), streamwise shear stress ($\tilde{\tau}_{sz}$), streamwise advective momentum transfer per unit of mass and area ($M_s = u_s u_z$), and vertical advective momentum transfer per unit of mass and area ($M_n = u_n u_z$).

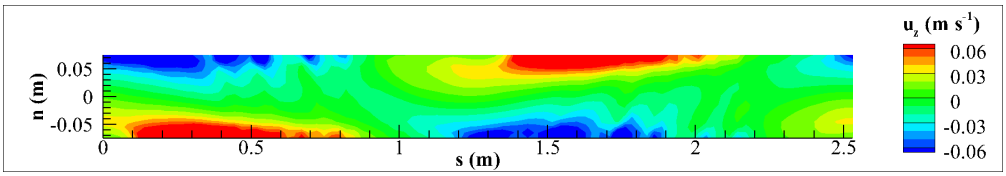


(b) Spatial distribution of $u_x|_{z_t}$.

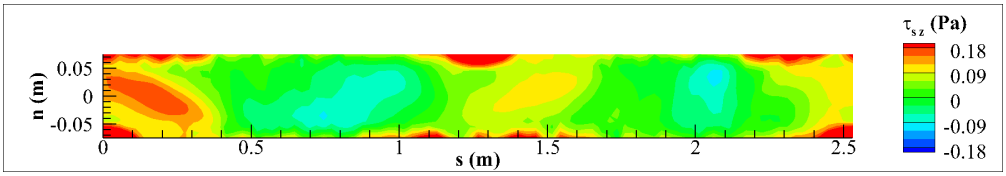


(c) Spatial distribution of $\tau_s$.

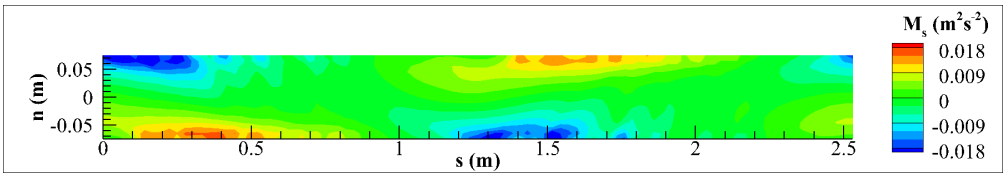


(d) Spatial distribution of $(u_s u_z)|_{z_t}$.

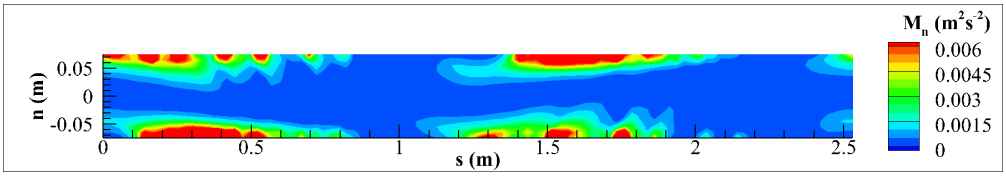


(e) Spatial distribution of $(u_z u_z)|_{z_t}$.

Figure 9: Mass and momentum transfer terms for the vertical-coupling method along a half meander wavelength derived from the Flow-3D simulation.

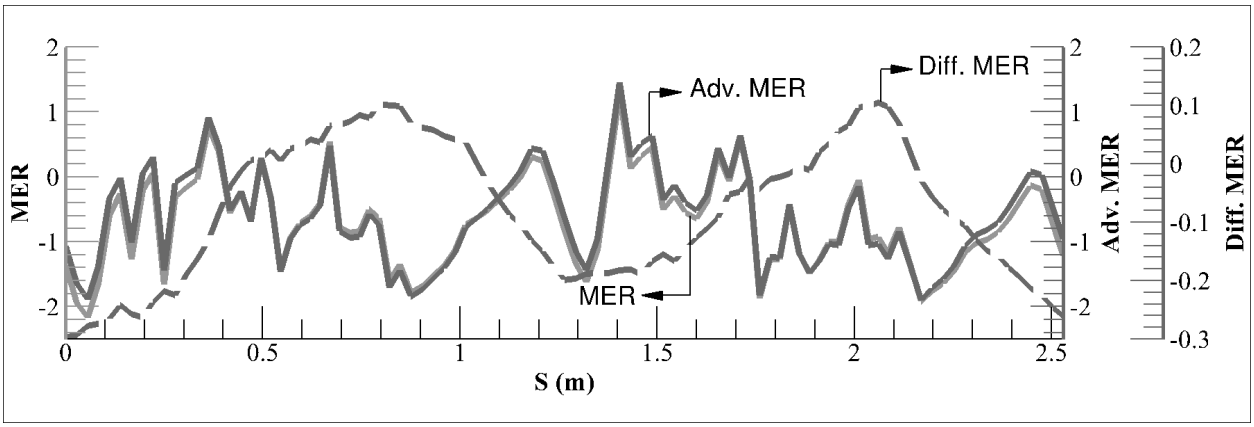


Figure 10: Relative importance of momentum transfer within vertically-coupled 1D and 2D computational regions for experiment "R2-rectangular" of Shiono and Muto (1998). Momentum Exchange Ratio (MER), or ratio between momentum transfer through the horizontal 1D-2D interface and mean boundary shear stress, is defined as $B(\tilde{u_s}\partial\tilde{d}/\partial t - \tilde{\tau_s}/\rho)/(g\,A\,S_o)$, Advective Momentum Exchange Ratio (Adv. MER) is $(B\tilde{u_s}\partial\tilde{d}/\partial t)/(g\,A\,S_o)$, and Diffusive Momentum Exchange Ratio (Diff. MER) is $-B\tilde{\tau_s}/(\rho\,g\,A\,S_o)$.

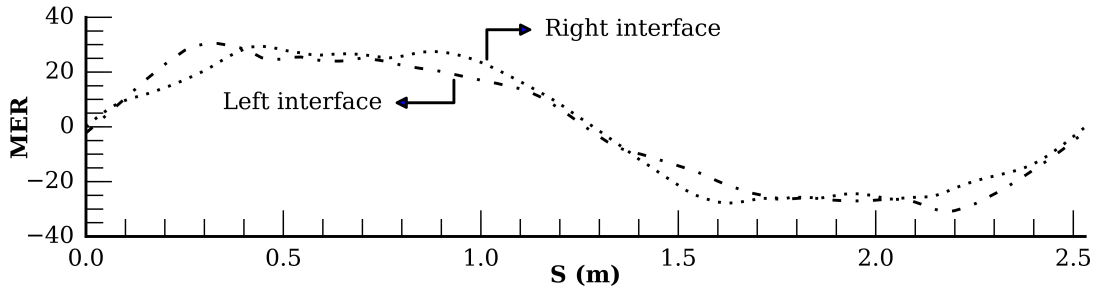


Figure 11: Relative importance of momentum transfer within horizontal-coupled 1D and 2D computational regions for experiment "R2-rectangular" of Shiono and Muto (1998). Momentum Exchange Ratio (MER), or ratio between momentum transfer through the vertical 1D-2D interface and mean boundary shear stress, is defined as $(\bar{u}_s q_n - h\bar{\tau}_s/\rho)/(g\,A\,S_o)$.

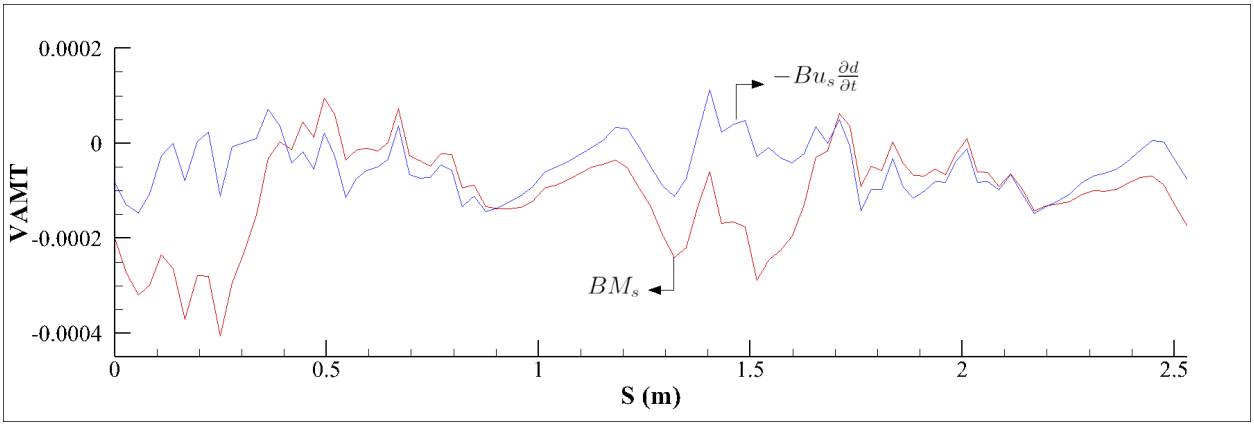


Figure 12: Exact($B\,M_s$) vs. approximate ($-B\,\tilde{u}_s\,\partial\tilde{d}/\partial t$) vertical advective momentum transfer per unit of mass and length over the horizontal bankfull interface in a vertical coupling approach.

# 3.0 COMPARISON OF HORIZONTAL AND VERTICAL COUPLING FOR ONE- AND TWO-DIMENSIONAL OPEN CHANNEL FLOW MODELS

## 3.1 INTRODUCTION

Many numerical models of overbank flow have been developed in the past. Bates and De Roo (2000) used a one-dimensional (1D) kinematic wave model to simulate river flow in combination with a two-dimensional (2D) diffusion-wave model to simulate overbank flow for the large flood event of January 1995 on the river Meuse, Netherlands. The simulation showed errors greater than 10%; however, results from a 2D finite element model and spatial interpolation of observed gauge levels showed the same level of error. Chatterjee, Förster, and Bronstert (2008) applied a 1D model (MIKE 11, DHI (2007a)) and a 1D-2D horizontally coupled model (MIKE FLOOD, DHI (2007b)) to simulate the flooding and withdrawal processes in flood emergency storage areas along the Elbe River for the extreme event of August 2002. Results showed the utility of overbank flood modeling to verify the design of hydraulic works (emergency storage areas), to define control strategies and to compute derived processes (such as erosion or sedimentation). Moussa and Bocquillon (2009) modeled the flood event of October 1958 on the Hérault river, France. Moussa and Bocquillon (2009) combined one 1D dynamic- and two 1D diffusive-wave models to route the flow through the river and its floodplain, respectively. Additionally, weir equations were used to laterally couple the main channel and floodplain domains. Although, Moussa and Bocquillon (2009) presented an efficient methodology, the errors in the simulated shape, volume and peak of the flood event exceeded 10%.

A three-dimensional (3D) hydrodynamic model is computationally expensive and practically unnecessary at the reach scale (Costabile & Macchione, 2011). Especially, since overbank floods are unsteady flows by nature, 3D unsteady solutions need to be run for a long period of time that in

general are more computational and memory expensive than finding a 3D steady solution. Although Horritt et al. (2007) describe 2D models as the most feasible, sophisticated approach to simulate inundations, a full 2D hydrodynamic representation of the river with its surrounding area would be too demanding for data collection and computational effort (Altinakar et al., 2008; Bernini & Franchini, 2013; A. Cook & Merwade, 2009; Costabile & Macchione, 2011) because high slope areas, as the ones presented on the sides of the river, require a very fine resolution; this is not the case when the river is modeled as 1D region in 1D or 1D-2D coupling models. 1D models are the most widely used computer models for flood inundation studies because of their computational efficiency and reduced data requirements (Costabile & Macchione, 2011). The disadvantage of a 1D hydraulic model for flood analysis is the need to set-up the channel network topology, which may be very difficult to assess and can change during a flood event (Connell et al., 2001). Also, 1D models assume, along the entire width of the cross section, a horizontal water surface, the same flow regime and velocity distribution, which most of the time is not valid for compound channels during flood events (Costabile & Macchione, 2011). To improve upon that, 1D models are extended to quasi-2D by dividing the compound cross section into either homogeneous subsections (Divided Channel Method), or subsections with different water levels and velocities (Independent Sub-sections Method) (Costabile & Macchione, 2011). For example, HEC-RAS uses the Divided Channel Method. In addition, ignoring the momentum exchange between the main channel and floodplains causes an overestimation of the discharge (Costabile & Macchione, 2011). This can be overcome by using empirical procedures to account for lateral momentum transfer.

Coupling 1D and 2D models, either horizontally or vertically, could provide computationally efficient models that simulate realistic flow patterns on the floodplain. 1D-2D coupled models are readily available, such as HEC-RAS 5.0.3 (Brunner, 2016b), SOBEK (Deltares, 2016) and MIKE FLOOD (DHI, 2007b). Or, 3D validated models could be used to behave as 1D-2D coupled models. These 1D-2D coupled models use the horizontal coupling strategy, which covers the simulation region by 1D models for river channels and 2D models for floodplain regions. In contrast, the vertical coupling strategy uses 1D models only for the in-bank flow (D'Alpaos & Defina, 2007). The overbank flow, including that above the channel, is simulated by a 2D model.

Simon, Langendoen, Abad, and Mendoza (2016) derived the governing equations of horizontally (1D channel and 2D floodplain regions) and vertically (1D in-bank and 2D overbank regions)

coupled 1D and 2D hydrodynamic models, which introduce terms of mass and both advective and diffusive, turbulent momentum transfer. Simon, Langendoen, Abad, and Mendoza (2016) found that the magnitude of the mass and momentum transfer terms at the 1D-2D interface are lower for the vertical than the horizontal coupling method. As these transfer terms have to be approximated, possible errors could have a smaller impact for the vertical coupling method than for the horizontal coupling method. The main objective of this paper is to test this hypothesis using widely-used, freely available 1D, 2D, and 3D open-channel flow computer models.

## 3.2 METHODOLOGY

### 3.2.1 Models

Different widely-used 1D, 2D and 3D computer models were employed to compare the performance of 1D-2D coupling strategies to accurately simulate overbank flood events. Herein, The authors present a brief description of the models used in this study.

TELEMAC-2D is a free-surface maritime and river hydraulics code originally developed by the National Hydraulics and Environment Laboratory (LNHE) of the Research and Development Directorate of the French Electricity Board (EDF), and currently in collaboration with many other research institutes (Desombre, 2013). TELEMAC-2D can be used to replicate a fully implicit horizontal coupling algorithm. Example applications of TELEMAC-2D to simulate flooding events are Teles, Smolders, Maximova, Rocabado, and Vanlede (2015), Vu, Nguyen, Chua, and Law (2015), Sanyal, Carbonneau, and Densmore (2014), Joy Lim, Anders Brandt Examinator, Östman Co-examinator, and Jiang (2011), Di Baldassarre, Schumann, Bates, Freer, and Beven (2010), Di Baldassarre, Castellarin, and Brath (2009), Viala, Leroy, Brignolles, and Sau (2005), Syme, Pinnell, and Wicks (2004), Giampieri, Tassi, Rodríguez, Gaudin, and Vionnet (2003), and Horritt and Bates (2002).

The Hydrologic Engineering Center - River Analysis System (HEC-RAS) model is widely used for engineering applications. It is designed to perform 1D hydraulic calculations for a full network of natural and constructed channels (Brunner, 2010). The program solve unsteady solutions from

the continuity and momentum equations using an linearized, implicit, finite difference equation of second order in space and first or second order in time depending on the parameter $\theta$ set by the user. Version 5 has added the capacity to perform 2D unsteady hydrodynamic flow routing (Brunner, 2014), such that the authors can use the 1D hydraulic model to simulate flow in the main channel and the 2D hydrodynamic model to simulate the flow over the floodplains. The 2D model solves continuity and momentum of the shallow water equations (SWE) by a finite volume method. Lateral structures connect the 2D flow region on the floodplain with the 1D channel. These lateral structures describe the mass transfer based on the water level difference between 1D and 2D regions either by an empirical weir equation or by imposing a normal flow boundary condition in the 2D flow area. These structures represent a simplified horizontal coupling algorithm. Example applications of HEC-RAS to flooding events are Moya Quiroga, Kure, Udo, and Mano (2016), Gharbi, Soualmia, Dartus, and Masbernat (2016), Suriya and Mudgal (2012), Costabile and Macchione (2011), Timbadiya (2011), Joy Lim et al. (2011), Qi and Altinakar (2011), Di Baldassarre et al. (2009), A. C. Cook (2008), Hicks and Peacock (2005), Benito, Díez-Herrero, and Fernández De Villalta (2003), Horritt and Bates (2002), and Pistocchi and Mazzoli (2002).

To simulate a full vertically coupling algorithm, the authors use the general 3D Computational Fluid Dynamics (CFD) software Open Field Operation And Manipulation platform (OpenFOAM). OpenFOAM is a C++ library used to efficiently solve partial differential equations (Wang & Zhou, 2015). As a general CFD software, OpenFOAM has a wide range of hydraulic applications that range from the simulation of complicated fluid flow to heat conduction and chemical reactions (Wang & Zhou, 2015). Example applications of OpenFOAM to flooding events are Robb and Vasquez (2015), Francesco, Biscarini, and Montesarchio (2014), Lopes (n.d.), and Benito et al. (2003)

### 3.2.2 Study Case

The overbank flow experiment "R2-rectangular" on a compound meandering channel of Shiono and Muto (1998) is our study case. This study case allows us to test specific interactions between zones modeled using 1D and 2D open-channel flow computer models. The relative flow depth is $D_r = 0.50$, which is defined as the ratio of the floodplain water depth to the main channel water

depth. Thus, the flow depth on the floodplain equals that of the in-bank main channel, giving a similar importance to both zones regarding the flow behavior. The experiment was carried out within a basin flume with a width of 1.2 m, a length of 10.8 m, and a longitudinal slope of 0.001; most of this area corresponds to the floodplains. A rectangular meandering channel was carved along the entire length of the basin flume. This meandering channel had a width of 150 mm, a depth of 53 mm, a sinuosity of 1.37, and comprised 5 meander waves with a wavelength of 1.85 m. The measurement section was half a meander wavelength of the fourth meander (Shiono & Muto, 1998). A 3D view of a complete wave of the meandering channel is shown in Figure 13. The discharge for the experiment was 19.996 L/s, which resulted in a total flow depth of 105.9 mm.

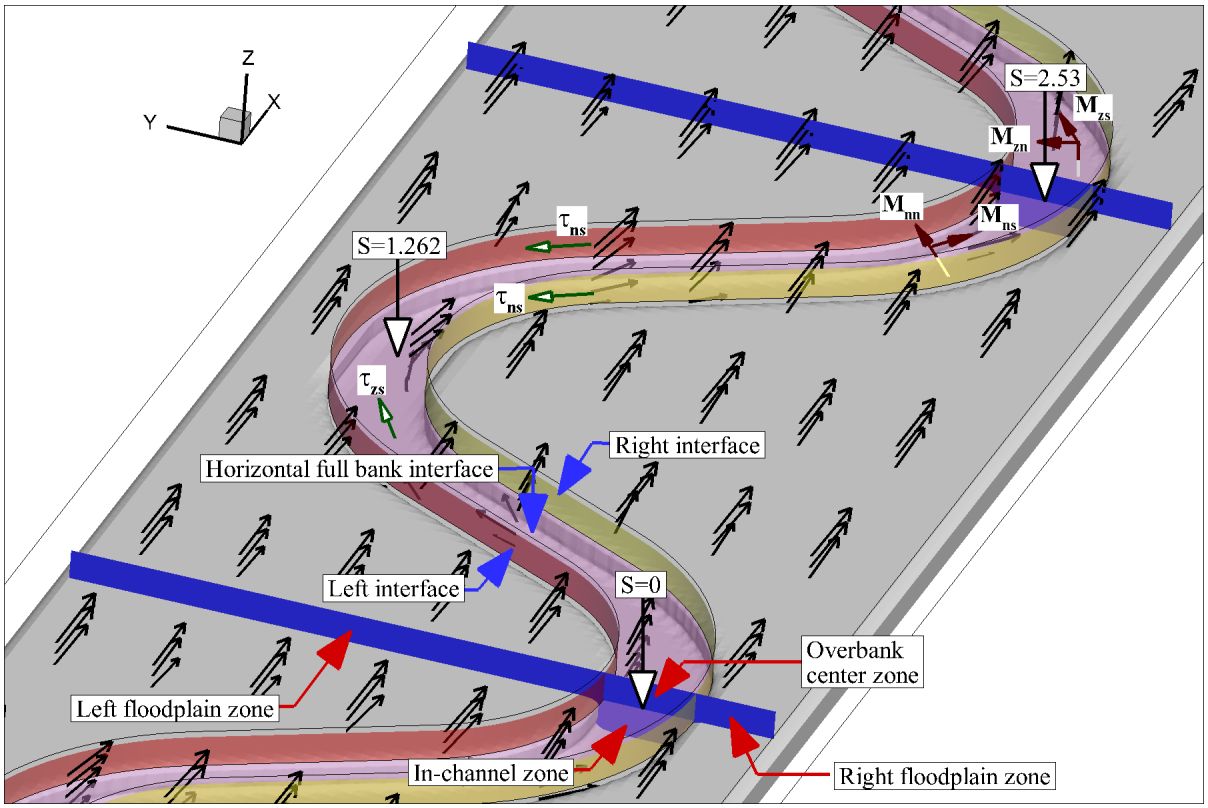


Figure 13: 3D view of a complete wavelength (between $s = 0$ and $s = 2.53$ m) of the meandering channel with zones and their interfaces labeled.

The regions that occupies the central meandering channel below and above the floodplain elevation are denoted to as in-bank and overbank central zones, respectively. The two zones at each side of the central meandering channel are named the left and right floodplain zones. The

interface between the left (right) floodplain zone and the overbank central zone is called the left (right) interface. The left and right interfaces separate the flow in and above the channel from the flow on the floodplains, and are used in the horizontal coupling procedure (1D in the combined in-bank and overbank central zones and 2D in the left and right floodplain zones). In the vertical coupling approach (1D in the in-bank zone and 2D in the left floodplain, overbank central zone and right floodplain) the interface between the in-bank and overbank central zones is called horizontal bankfull interface.

### 3.2.3 Model Setup and Scenarios

The models described in the previous section were used to evaluate 1D-2D coupling scenarios to model overbank flood flows. Two horizontally-coupling scenarios and one vertically-coupling scenario were simulated. The 2D model TELEMAC-2D was used to simulate the combined flow in the main channel and floodplain zones. This is equivalent to a 2D-2D horizontal-coupling scenario that implicitly accounts for the transfer of mass and momentum between the central meandering channel and the floodplain zones. HEC-RAS was used to conduct the second, but simplified horizontal-coupling scenario as only lateral mass tranfer is accounted for. To the knowledge of the authors, no 1D-2D vertical coupling model is readily available. Therefore, the authors used OpenFOAM to mimic this scenario. One mesh consisting of a series of cells, with each cell spanning the width of the channel, was used to represent the in-bank zone (see Fig. 14(i)), which produces a 1D simulation. The overbank zones were covered by an unstructured mesh with two cells in vertical direction, which results in a 2D simulation. Two vertical cells were needed to determine the location of the water surface.

To summarize, the studied scenarios are:

- Scenario 1: a complete 2D simulation over the entire domain using the model TELEMAC-2D (Desombre, 2013), which represents a complete, implicit 2D-2D horizontal-coupling scenario.
- Scenario 2: a 1D-2D horizontal coupling scenario using HEC-RAS (Brunner, 2014), which represents a simplified 1D-2D horizontal coupling scenario.
- Scenario 3: a 1D-2D vertical-coupling approach using the 3D CFD code OpenFOAM.

The flow in the experiment by Shiono and Muto (1998) was subcritical. Therefore, the boundary conditions used for all scenarios were: a discharge of 19.996 L/s imposed at the upstream boundary, a water surface elevation of 105.9 mm imposed at the downstream boundary, and wall conditions (velocity equal to 0) at the solid sides of the basin. The Manning roughness coefficient used in each scenario was calibrated such that the longitudinal water profile slope value equaled the longitudinal bottom slope value of 0.001. The resulting values varied between 0.008 and 0.01. Note, preliminary simulations were performed to determine the required mesh size for achieving mesh independent model results.

The simulation with TELEMAC-2D used an unstructured mesh of triangles (see Figure 14(a)) with a finer resolution in the channel than along the floodplains to more accurately represent the vertical walls of the meandering channel (see Figures 14(b) and 14(c)). The advantage of an irregular mesh in 2D flow simulations is the size adaptability of its elements to make a smooth transition from a coarse mesh zone to a finer mesh zone as is depicted in Figure 14(b) and Figure 14(c). The elements inside the meandering channel had a mean side length of 3 mm, while the mean side length of the elements in the floodplain was 50 mm. Following Frias et al. (2015) and Mendoza et al. (2014), the authors used the $k - \epsilon$ turbulence model

HEC-RAS uses a simplified horizontal coupling with 1D elements in the river and 2D elements in the floodplain (Brunner, 2014). The simplified horizontal coupling strategy considerably reduced the number of elements used in the simulation (compare Figure 14(d) with Figure 14(a)). The meandering central channel was modeled with 1D elements, that is cross sections, spaced 50 mm apart. The floodplain was modeled with a structured mesh comprising square elements with a side length of 50 mm. The elements in contact with the interface between the meandering channel and the floodplain are polygons with multiple faces that adjust to the geometry of the meandering channel and the neighboring elements (see Figure 14(e) and Figure 14(f)).

For the OpenFOAM simulation, the authors used two horizontal distributions of cells: the first distribution covers the height of the in-bank zone, from 0 mm to 53 mm. An overlying second distribution covers all the overbank flow from 53 mm to 120 mm. Figure 14(g) shows the top view of the unstructured mesh used in each block of the OpenFOAM simulation. The cells follow the meandering central channel geometry (see Figure 14(h) and Figure 14(i)). The bigger, square cells used in OpenFOAM had a side length of 50 mm in the horizontal direction and 53 mm in the

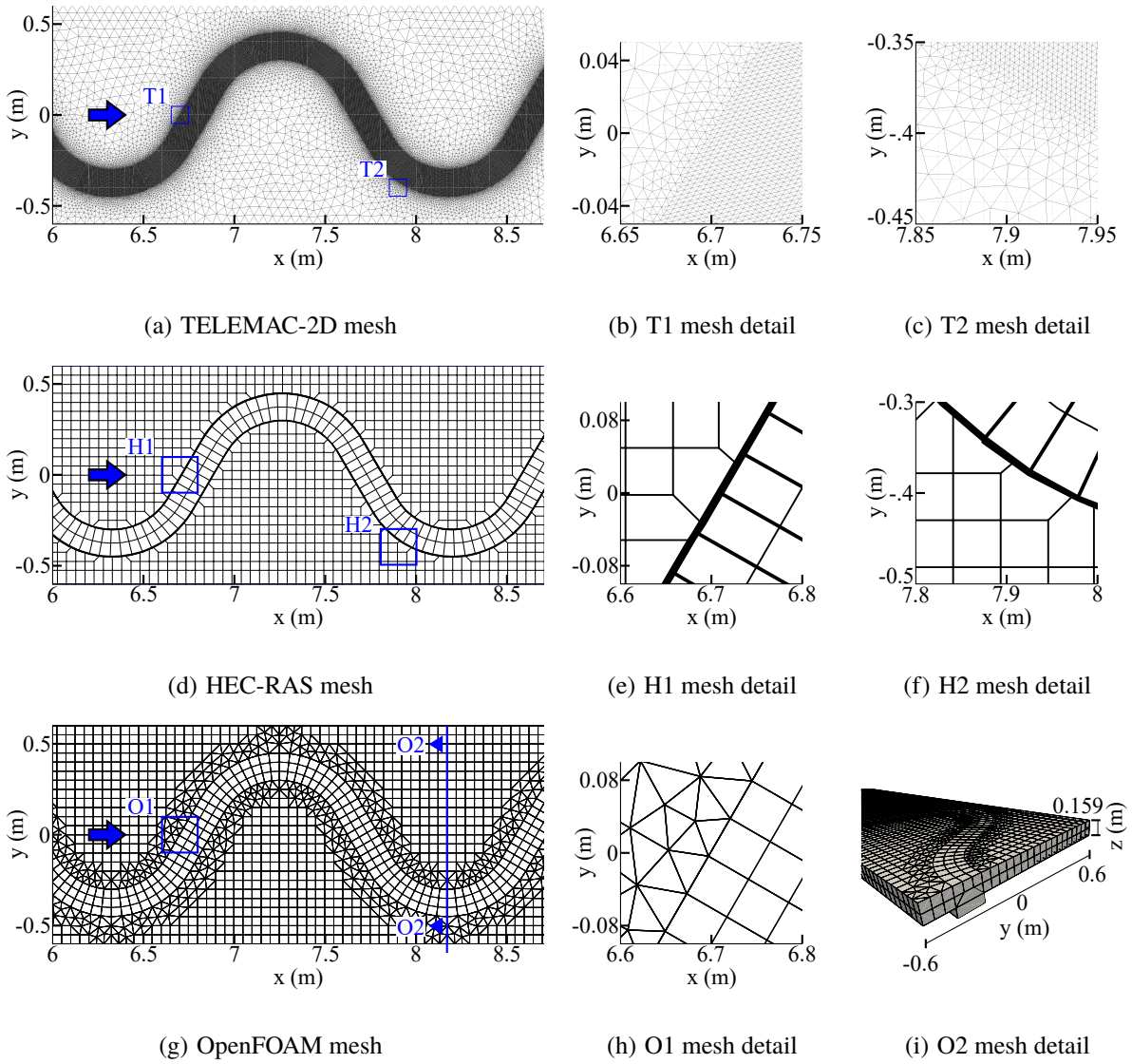


(a) TELEMAC-2D mesh (b) T1 mesh detail (c) T2 mesh detail

(d) HEC-RAS mesh (e) H1 mesh detail (f) H2 mesh detail

(g) OpenFOAM mesh (h) O1 mesh detail (i) O2 mesh detail

Figure 14: Domain discretization to simulate Shiono and Muto (1998)'s compound meandering channel. Blue arrows indicate flow direction. Red arrows indicate streamwise and transverse coordinates following the meandering channel. (a) TELEMAC-2D mesh. (b) T1 mesh detail, within a straight portion of the channel and the left overbank. (c) T2 mesh detail, within a channel bend and the right overbank. (d) HEC-RAS 5.0 mesh. (e) H1 mesh detail, similar to T1. (f) H2 mesh detail, similar to T2. (g) OpenFOAM mesh. (h) O1 mesh detail, with the interface between a central straight channel zone and the left overbank. (i) O2 mesh section.

vertical direction. The simulation was performed using the $k - \epsilon$ turbulence model with the default parameters and no-slip condition for the walls.

To present the model results, the authors used two coordinate systems: a Cartesian coordinate system $(x, y)$ aligned with the principal axes of the experimental basin, and a curvilinear coordinate system $(s, n)$ following the central meandering channel. For the Cartesian coordinate system the $x$-axis is aligned with the length of the basin and ranges from 0 to 10.8 m, while the $y$-axis is aligned with the width of the basin, and is directed from the right (-0.6 m) to the left side of the basin (+0.6 m). For the curvilinear coordinate system, the $s$-axis is aligned with the centerline of the meandering channel. The $n$-axis is perpendicular to the $s$-axis, and is directed to the left of the $s$ direction. For plotting purposes the origin of the $s$-axis ($s = 0$ m) is the fourth meander bend apex. The length of a meander wave measured along $s$ is 2.53 m.

## 3.3 RESULTS

### 3.3.1 Depth-Averaged Velocities

Figure 15 compares the measured and simulated depth-averaged velocities. For the experiment and the vertically-coupled OpenFOAM simulation the vertically-averaged in-bank and overbank vectors are plotted, whereas for the Telemac-2D and HEC-RAS simulations we only present the depth-averaged velocity vector. Figure 16 presents enlarged views of measured and simulated depth-averaged velocities for more a detailed comparison. The locations of the detailed views are identified in Figure 15. The overall depth averaged velocity magnitudes (using the results from both in-bank and overbank regions) are presented as contours.

For TELEMAC-2D the velocity magnitude pattern is different from that measured, with higher and lower velocities regions located in different zones of the flume (compare Figure 15(a) and (b)). The highest velocities are located close to the walls of the flume, away from the meandering channel bends, in a region 0.2 m wide. Lowest values are located inside the meandering channel near the inflection region. Along most of the central part of the flume, flow velocities are close to the average of 0.25 m/s. The steering of the in-channel flow simulated by TELEMAC-2D is not as strong as that

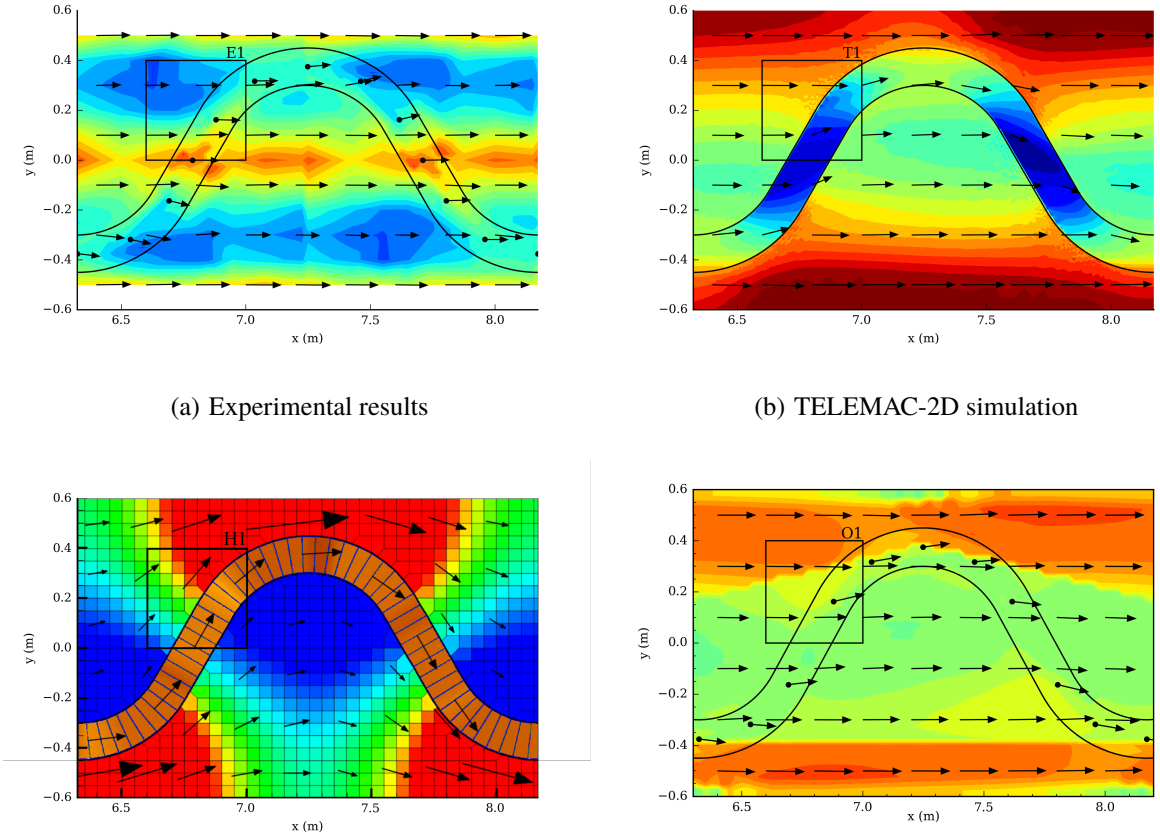


(a) Experimental results

(b) TELEMAC-2D simulation

(c) HEC-RAS simulation

(d) OpenFOAM simulation

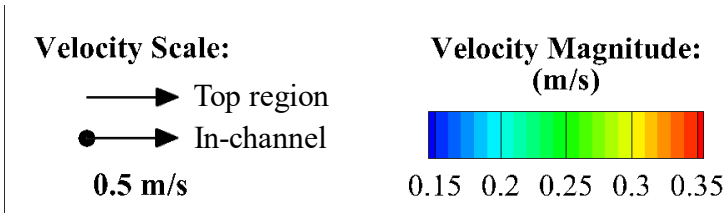


(e) Legend

Figure 15: Comparison of observed and simulated flow velocities using different 1D-2D coupling methods for experiment "R2-rectangular" of Shiono and Muto (1998): (a) observed mean in-bank and overbank velocities; (b) depth-averaged velocities simulated using TELEMAC-2D; (c) depth-averaged velocities simulated by HEC-RAS 5.0 Beta; and (d) layer-mean in-bank and overbank velocities simulated by OpenFOAM. (e) Legend: In-bank velocity vectors are identified by a small bullet at their tail. Details E1, T1, H1, and O1 are shown in Figure 16.

observed where the in-bank flow has similar flow direction as the overbank flow (compare Figure 16(a) and (b)). Further, the simulated in-bank velocities are smaller than those observed. Figure 16(b) shows an abrupt change in flow velocity magnitude at the interfaces between the meandering channel and floodplains. The difference in measured and simulated velocity magnitude is on average 0.065 m/s with a standard deviation of 0.036 m/s, and a maximum of 0.178 m/s. Average velocity magnitude differences are found at the interface of meandering channel and floodplain, at meander bend apices, and along longitudinal transects at $y$ = 0, ± 0.2, and ± 0.5 m. Maximum differences are found in the cross-over regions of the meandering channel.

For the HEC-RAS simulation, the overbank flow is mostly parallel to the meandering channel, with large velocities near the outer bank, where bends approach the basin side walls, and small velocities near the opposite, inner bank (Figure 15(c)). The simplified, incomplete horizontal coupling does not accurately predict the flow velocity directions and magnitudes; the overbank flow does not cross the main channel and converges towards the boundaries of the basin, see also the more detailed velocity field in region H1 (Figure 16(c)). Similar to the flow simulated using TELEMAC-2D, there is an abrupt transition in flow velocity magnitude at the interfaces between the meandering channel and floodplains. The differences between measured flow velocity magnitude and that simulated by HEC-RAS are the largest of all scenarios with a maximum difference of approximately 0.6 m/s on the floodplain near bend apices.

For the vertically-coupled OpenFOAM simulation (Figure 15(d)), the effect of the in-bank flow on overbank flow is minimal. The simulated depth-averaged in-bank flow compares well with that observed (Figure 15(a)). The simulated in-bank velocity magnitude is slightly larger than that measured, and the most significant differences in velocity vector direction are found upstream of the bend apices. Similar to TELEMAC-2D and HEC-RAS, the overall depth-averaged overbank velocities are highest near the right and left sides of the flume, and lowest along the flume centerline. However, in contrast to TELEMAC-2D, the highest velocities are away from the side walls where velocity is reduced from 0.35 m/s to 0.25 m/s.

Figure 16(d) shows a smooth transition of flow between the meandering channel and floodplains. The difference between measured velocity magnitude and that simulated by OpenFOAM is on average 0.052 m/s with a standard deviation of 0.03 m/s, and has a maximum of 0.126 m/s. Average

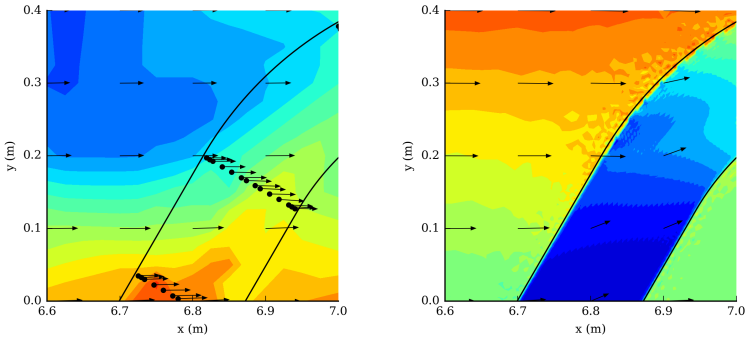


(a) E1 velocity field detail




(b) T1 velocity field detail

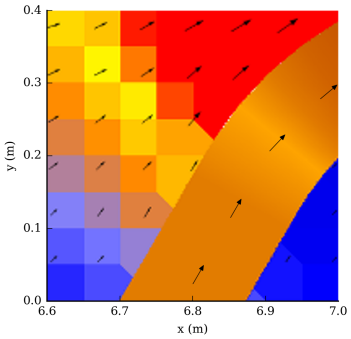


(c) H1 velocity field detail

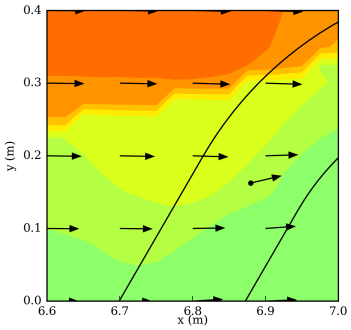


(d) O1 velocity field detail

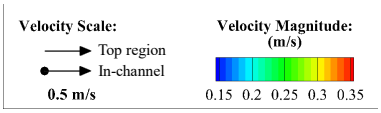


(e) Legend

Figure 16: Detailed view of observed and simulated flow velocities using different 1D-2D coupling methods for experiment "R2-rectangular" of Shiono and Muto (1998): (a) Detail E1, observed mean in-bank and overbank velocities; (b) Detail T1, depth-averaged velocities simulated using TELEMAC-2D; (c) Detail H1, depth-averaged velocities simulated by HEC-RAS 5.0 Beta; and (d) Detail O1, layer-mean in-bank and overbank velocities simulated by OpenFOAM. (e) Legend: In-bank velocity vectors are identified by a small bullet at their tail.

velocity magnitude differences are found at the interface of meandering channel and floodplain, and along longitudinal transects at $y$ = 0, ± 0.2, and ± 0.45 m.

### 3.3.2 Mass and Momentum Transfer Terms

We computed the mass and momentum transfer terms at the channel-floodplain interfaces from the simulated flow field for each coupling strategy. The transfer terms considered are the normal unit discharge ($q_n$ or $q_z$) representing exchange of mass, the shear stress ($\tau_{ns}$ or $\tau_{zs}$) representing diffusive transfer of momentum, and the diffusive and advective momentum transfer terms ($M_{ns}$, $M_{nn}$, $M_{zs}$, and $M_{zn}$). See also Figure 13 (Simon, Langendoen, Abad, & Mendoza, 2016). As the observed and simulated flow fields are nearly the same from bend to bend (see Figure 15), the interface terms will be presented for half a meander wavelength ($0 \leq s \leq 1.26$ m), see Figure 13 for location.

For the horizontal coupling strategy evaluated with TELEMAC-2D the magnitude of the normal unit discharge ($q_n$) varies between -0.015 $m^2/s$ and 0.015 $m^2/s$ (Figure 17(a)). Flow enters the meandering channel zone through the left vertical interface at the first half of the meander and leaves the channel through this interface along the second half in a symmetric manner, which is in agreement with the experimental results. The simulated shear stress is near zero except for $0.8 \leq s \leq 1.1$ m (see Figure 17(a)). The absolute magnitude of the shear stress at the interface does not exceed 1.5 Pa. However, the complete horizontal coupling approach was not able to compute the interface shear stress correctly as it differs markedly from that measured (compare square markers and dash line in Figure 17(a)). The advective transfer of streamwise momentum across the left interface is negative along the first half of the meander ($0 \leq s \leq 1.26$ m) and positive along the second half ($1.26 \leq s \leq 2.53$ m, not shown in Figure 17(b)). For this interface, a negative value indicates that the meandering channel flow is being accelerated in the $s$-direction by the advective momentum transfer from the left floodplain flow. In contrast, a positive value indicates a deceleration of the meandering channel flow in the $s$-direction by an advective momentum transfer from the main channel flow to the left floodplain flow. The computed advective transfer of streamwise momentum by the complete horizontal coupling approach compares well with the experimental results (see cross symbols and dash-dot line in Figure 17(b)). The simulated advective

transfer of transverse momentum to the meandering channel ($M_{nn}$) is always positive and of similar absolute magnitude as $M_{ns}$. The computed values compare well with those measured for $s < 0.7$, but are of opposite sign for $s > 0.8$. By decomposing $M_{nn}$ into $x$- and $y$-components, we can interpret the positive values in the first half of the meander (shown in Figure 17(b)) as an increase in the $x$-momentum inside the meandering channel, and the positive values in the second half of the meander as a decrease in the $x$-momentum.

The mass and advective transverse momentum exchange terms across the left vertical interface simulated by HEC-RAS show the same pattern as those calculated by TELEMAC-2D (see Figures 17 and 18). However, their magnitude is very small compared with the experimental results and TELEMAC-2D simulation. The magnitude of the unit discharge ($|q_n|$) is smaller than 0.001 $m^2/s$, and $M_{nn}$ does not exceed $2 \times 10^{-4}$ $m^2/s^2$ (Figure 18). The observed magnitudes reach 0.015 $m^2/s$ and 0.1 $m^2/s^2$ (see Figure 18). Therefore, the incomplete horizontal coupling provided by HEC-RAS strongly underestimates the exchange of mass and momentum between main channel and floodplain flows.

Figure 19 shows that the mass and advective momentum transfer terms across the horizontal bankfull interface for the vertical-coupling approach, simulated using OpenFOAM, are about 20 times smaller than those for the horizontal-coupling method (cf. Figure 17). A positive $q_z$ indicates a transfer of mass from the in-bank zone to the overbank central zone, and a negative value indicates a transfer in the opposite direction. Figure 19(a) shows a mass transfer controlled by the channel planform. Mass enters the in-bank zone in the straight, crossover sections and upstream portions of bends. Mass is leaving the in-bank zone at bend apices and immediately downstream. The computed mass transfer is greater than and opposite of that observed (Figure 19(a)). The simulated $\tau_{zs}$ is, in general, positive and does not exceed 1.8 Pa. The simulated $\tau_{zs}$ agrees well with the experimental result at the bends but not at the channel crossovers (compare the dashed line with the square symbols in Figure 19(a)). The pattern of the simulated vertical transfer of streamwise momentum, $M_{zs}$, resembles the meander planform similar to $q_z$, which is out of phase with the observed pattern (compare the dash-dot line with the crosses in Figure 19(b)). $M_{zs}$ is positive downstream of bends and negative upstream. A positive or negative $M_{zs}$ indicates a loss or gain, respectively, of momentum in the $s$-direction. The observed vertical transfer of transverse momentum $M_{zn}$ is near zero with slightly higher values in the straight sections of the meandering

channel. A positive or negative $M_{zn}$ indicates a loss or gain of momentum in the $n$-direction, respectively. The $M_{zn}$ simulated with the vertical-coupling approach shows a less erratic behavior; its values are primarily opposite of $M_{zs}$.

## 3.4 DISCUSSION

The observed flow in experiment âĂIJR2-rectangularâĂİ of Shiono and Muto (1998) shows three longitudinal bands of higher velocity ($y$ = 0 and ±0.5 m) and two longitudinal bands, located over the meander bend apices ($y$ = ±0.3 m), of lower velocity (Figure 15(a)). This general pattern is not captured by the horizontal coupling methods of TELEMAC-2D and HEC-RAS and the vertical coupling method of OpenFOAM (Figure 15(b-d)). The vertical interaction between the in-bank and overbank flow is greater at the meander bends, as the bend apex is oriented along the overbank flow direction, than the crossover sections. Using a 3D model, Simon, Langendoen, Abad, and Mendoza (2016) showed that the vertical velocities redirect the flow and concentrate it to the center of the floodplain ($y$ = 0 m) and basin sidewalls. It is therefore important to incorporate the vertical interaction in flood simulations where the floodplain flow interacts with the river flow.

The differences between the observed velocity field and that simulated by TELEMAC-2D is primarily the velocity magnitude. TELEMAC-2D presented the smallest velocity magnitudes at the straight, crossover sections of the channel, where the observed flow field has some of the highest velocities. The vertical interfaces between floodplain and channel do not impede the transfer of fluid mass and momentum between the meandering channel and floodplain, but the sudden increase in flow depth in the meandering channel reduces flow velocities significantly (Figure 16(b)). For the HEC-RAS modeling scenario, higher velocities are present in the meandering channel as well as the narrow outer bank floodplain region at bend apices, while low-velocity regions are present adjacent to the inner bank that extent over almost half the flume width (Figure 15(c)). The channel acts as a barrier for the floodplain flow, which causes the flow to converge where the floodplain narrows at bend apices. Whereas the horizontal coupling approaches of TELEMAC-2D and HEC-RAS showed the largest velocity magnitudes at the flume sidewalls ($y$ = ±0.6 m), the vertical coupling approach of OpenFOAM represents the outer high-velocity bands better (both in

magnitude and location). However, OpenFOAM did not simulate the observed center high-velocity region. OpenFOAM overestimated flow velocity at the bend apices as the velocity reduction by the vertical interaction is too small (Figure 16(d)).

The analysis of mass and momentum transfer terms at the channel-floodplain interfaces may explain the behavior of each coupling strategy. In general, the advective momentum transfer terms are 5 and 16 times larger for the horizontal and vertical coupling scenarios than the diffusive momentum transfer terms at their respective interfaces, which is an indication of the importance of advective exchange of momentum between overbank and in-channel flows. Note the advective momentum transfer terms must be multiplied by water density to directly compare their magnitude with the shear stress acting on the interface. The mass and streamwise advective momentum ($M_{ns}$) transfer terms for the horizontal coupling method using TELEMAC-2D have similar patterns and magnitudes as those measured (Figure 17). However, the diffusive momentum transfer ($\tau_{ns}$) and lateral advective momentum transfer ($M_{nn}$) do not. This may explain the large difference in between simulated and observed flow velocity at channel crossovers and meander bends. Figure 18 shows little or no mass and momentum transfer between 1D and 2D zones for the HEC-RAS simulation. The spatial patterns of mass and momentum transfer terms simulated by OpenFOAM's differ from those observed (Figure 19). For example, the experiment shows mass transfer from the in-bank to the overbank central zone at $s \approx 0.8$, whereas the OpenFOAM simulation shows the opposite behavior. The 3D model results of Simon, Langendoen, Abad, and Mendoza (2016) showed significant, laterally varying in-bank vertical velocities and helical flow in the bends that cannot be represented in a 1D model, and could be responsible for the presented differences.

The mass and momentum transfer terms in the vertical coupling approach (Figure 19) are one to two orders of magnitude smaller than those in the horizontal coupling approach (Figure 17). Therefore, any errors in the mass and momentum transfer terms should have less impact on the simulated flow field in-channel and adjacent to the channel in the vertical coupling approach than the horizontal coupling approach. A further advantage of the vertical coupling approach is that it implicitly accounts for the lateral exchange of mass and momentum between the flow on the floodplain and the overbank central zone.

## 3.5 CONCLUSION

This research investigated the ability of horizontally- and vertically-coupled 1D channel and 2D floodplain flow models, in use by industry and governmental agencies today, to simulate the overbank flow conditions of a meandering channel. The most important findings are:

- The mass and momentum transfer across the vertical channel-floodplain interface in the horizontal coupling method are one to two orders of magnitude greater than those across the horizontal in-bank-overbank interface in the vertical coupling method (compare Figure 17 and Figure 19). A vertical coupling approach therefore should be able to more accurately simulate overbank channel hydraulics, which was demonstrated by the results shown in Figure 15.

- For channels not aligned with the valley centerline, transfer of mass between channel and floodplain through a vertical interface in the horizontal coupling method is as large as the streamwise transfer in the overbank flow itself. Simple horizontal coupling strategies that use, for example, weir equations cannot adequately simulate the interactions, such as flow steering, between in-channel and floodplain flows as shown by Figure 15(b) (TELEMAC-2D) and Figure 15(c) (HEC-RAS).

- A vertical coupling approach implicitly accounts for the lateral mass and momentum exchange between the floodplain and overbank zone above the channel. In addition, it can account for the transfer of mass and momentum from overbank to in-bank and vice-versa through empirical relations, thereby further improving the simulated flow hydraulics in and adjacent to the channel. Here, these relations were based on width-averaged properties as the channel model (OpenFOAM) was one-dimensional. However, the vertical streamwise and lateral advective momentum transfer terms were not adequately simulated (Figure 19(b)), which caused discrepancies between observed and simulated hydraulics. The strongly, three-dimensional flow in meandering channels, and therefore the lateral variatios in vertical velocity and momentum on the bankfull interface, cannot be adequately represented by a 1D model. Improved empirical relations are needed to more accurately simulate the transfer of mass and momentum between in-bank and overbank flow when using a vertical coupling method.

## 3.6 ACKNOWLEDGMENTS

This work was performed under Specific Cooperative Agreement No. 405882 between the Department of Civil and Environmental Engineering of the University of Pittsburgh and the U.S. Department of Agriculture, Agricultural Research Service, National Sedimentation Laboratory, Oxford, MS. We thank CONACYT-Mexico for financially supporting Dr. Alejandro Mendoza's post-doctoral research at the University of Pittsburgh.

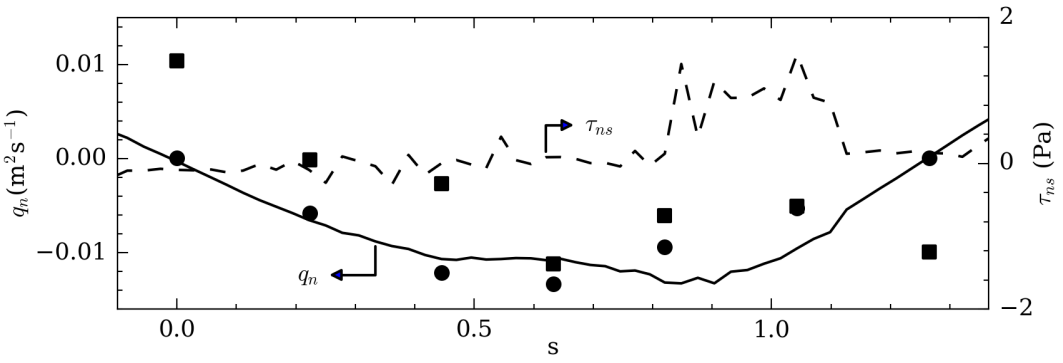


(a) $q_n$ and $\tau_{ns}$

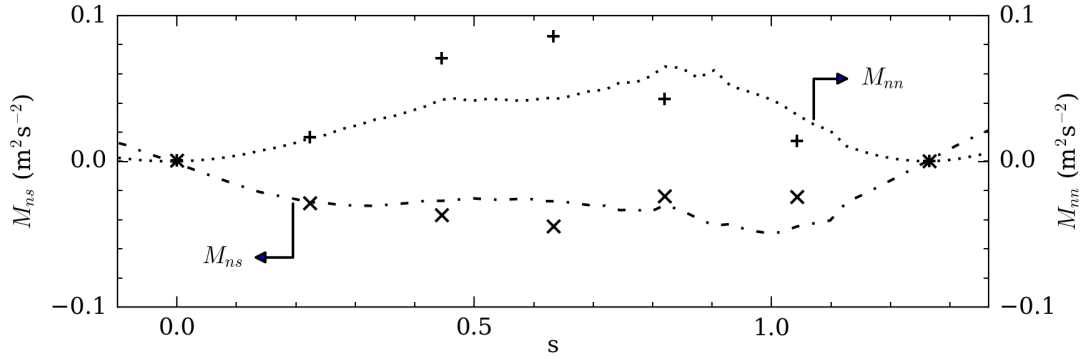


(b) $M_{ns}$ and $M_{nn}$

Figure 17: The mass and momentum transfer terms at the left vertical interface, simulated by TELEMAC-2D using a horizontal coupling method, are plotted for a half meander wavelength ($0 \leq s \leq 1.262$, cf. Figure 13), where: $q_n$ is the unit discharge in the $n$-direction, $\tau_{ns}$ is the vertically-averaged shear stress on the interface in the $s$-direction (representing turbulent momentum transfer), $M_{ns}$ is the transfer of the advective $s$-momentum component across the interface in $n$-direction, and $M_{nn}$ is the transfer of the advective $n$-momentum component across the interface in $n$-direction. The markers represent these terms calculated from the measured flow field: • is $q_n$, ■ is $\tau_{ns}$, × is $M_{ns}$, and + is $M_{nn}$.

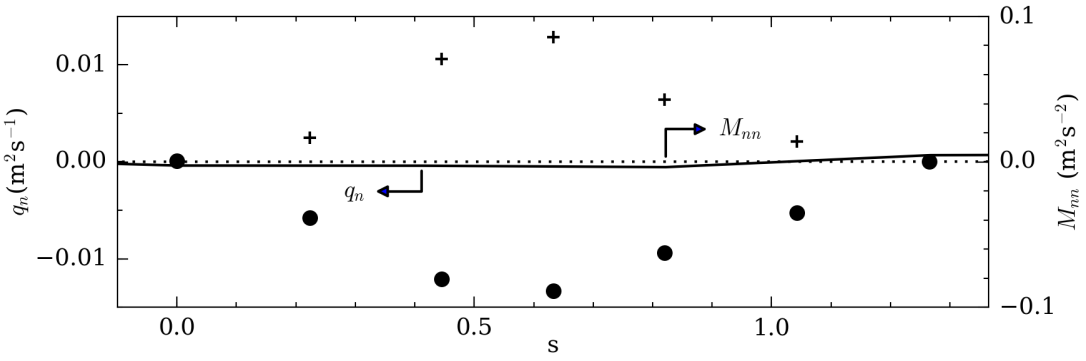


Figure 18: The mass and momentum transfer terms, simulated by the HEC-RAS simplified horizontal coupling method, plotted at the left vertical interface along half meander wavelength ($0 \leq s \leq 1.262$, cf. Figure 13), where: $q_n$ is the normal unit discharge and $M_{nn}$ is the advective transfer of $n$-momentum through the interface in $n$ direction. The markers represent these transfer terms computed from the measured flow field: • is $q_n$ and + is $M_{nn}$.

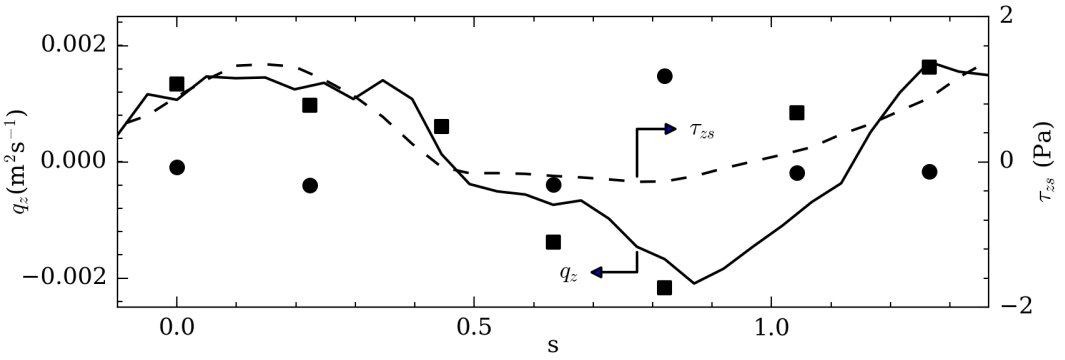


(a) $q_z$ and $\tau_{zs}$

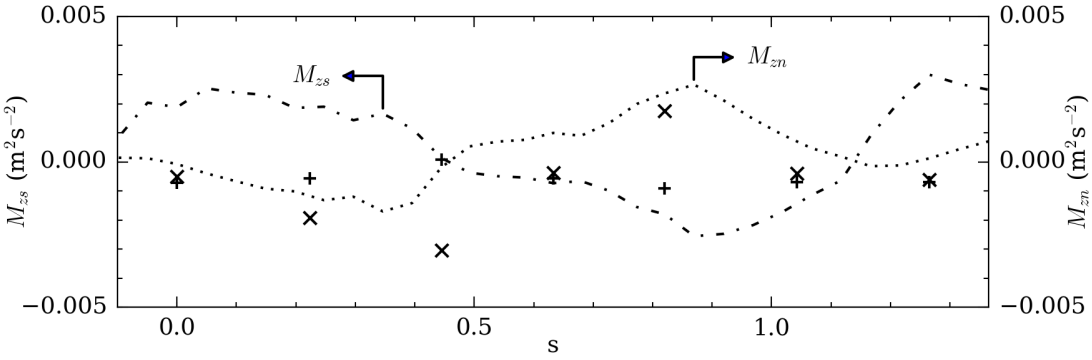


(b) $M_{zs}$ and $M_{zn}$

Figure 19: The mass and momentum transfer terms simulated by the vertical-coupling method using OpenFOAM plotted at the horizontal bankfull interface along half meander wavelength ($0 \leq s \leq 1.262$ m, cf. Figure 13), where: $q_z$ is the vertical unit discharge, $\tau_{zs}$ is the shear stress in the $s$-direction on the bankfull interface, $M_{zs}$ is the advective transfer of streamwise momentum through the interface, and $M_{zn}$ is the vertical advective transfer of transverse momentum through the interface in the $z$ direction. The markers represent these terms calculated from the measured flow field: • is $q_z$, ■ is $\tau_{zs}$, × is $M_{zs}$, and + is $M_{zn}$.

# 4.0 IQUITOS FLOODING PREDICTION, AND VULNERABILITY UNDER BOTH CLIMATE AND GEO-MORPHOLOGICAL CHANGES

## 4.1 INTRODUCTION

Flooding is one of the major natural disasters around the world (Bernini & Franchini, 2013; Connell et al., 2001; A. Cook & Merwade, 2009; Maatar, Domeneghetti, & Brath, 2015; Moya Quiroga et al., 2016). Floods have caused the loss of 96,507 human lives from 1992 to 2001; 170,010 from 1980 to 2000 (Dilley et al., 2005); and, only in 2010, floods affected 178 million people (Jha et al., 2012). Also, they are the cause of economic losses, in the order of billions of dollars (Bernini & Franchini, 2013; Connell et al., 2001; A. Cook & Merwade, 2009; Jha et al., 2012). As an example, in exceptional years of flooding, such as 1998 and 2010, "the economic losses associated with flooding exceeded $40 billion" (Jha et al., 2012). This data show that associated risk of flooding is growing. Principally, due to the increase in population and infrastructure density on floodplains, combined with climate change (Hofer & Messerli, 2006; Moya Quiroga et al., 2016). Nowadays, authorities need to manage flood-risk to reduce significant losses (Maatar et al., 2015) and provide sustainable growth. Especially, in areas where human development could alter the environmental behavior and threat the conservation of natural resources.

The Amazonia is the largest tropical forest on Earth (Adeney, 2009; Gentry & Lopez-Parodi, 1980), with twenty million people and tens of thousands of species living in this area (Adeney, 2009) that extends into several countries (J. L. Chen et al., 2010). The sustain of Amazonia biodiversity is the presence of the Amazon river. The Amazon is the world's largest river (Gentry & Lopez-Parodi, 1980), and its role as a carbon reservoir, water recycler, climate modulator and cluster of biodiversity is undisputed (Adeney, 2009). The Amazon Basin is the largest drainage basin in the world with a total area of 7.05 million $km^2$, which is about 40% of the total area of

South America (Adeney, 2009; Gordienko, 2010). Flood events in the Amazon basin extend along vast areas and affect a large population in cities like Iquitos (Coordinadora Nacional de Derechos Humanos, 2012; Espinoza et al., 2013).

In the decade 1970-1980, Gentry and Lopez-Parodi (1980) pointed to the marked increase in the height of the annual flood crest in the Amazon river. From the 1980s, the Amazon basin experienced an intensification of hydrological extremes, which particularly affects its Andean rivers (Espinoza et al., 2013). Although, exceptional inundations were reported from so long ago as 1859, 1892, 1895 and 1900 (Sternberg, 1987), and extreme high discharges were recorded in 1989, 1999 and 2009; an unprecedented high discharge happened in January 2012. The event of January 2012 peak at 55 400 $m^3 s^{-1}$ (which is the highest value recorded in the Peruvian Amazon river)for a region where the average discharge is 30 700 $m^3 s^{-1}$ (Mendoza et al., 2016). The flood event of January 2012 affected 140 000 people and triggered an emergency state declared by the Peruvian authority (Espinoza et al., 2013). Despite the consequences of Amazon flooding events, not much work has been dedicated to the highest floods in the western Amazon basin (Espinoza et al., 2013). Simulation studies of the Amazon river, like the one by Coe, Costa, Botta, and Birkett (2002), often underestimate discharge results because of the small amount of data available Coe et al. (2002). The small amount of real measurments is probably the reason of low statistical representation of simulations on the region.

Nowadays, there is an increasing concern about how environmental and climate change could affect the most valuable ecosystems on the planet(i.e., the Amazonia), that surround Iquitos city. The increase of atmospheric $CO_2$ threatens to alter the water budget (Coe et al., 2002) and therefore the flooding cycles. Changes in the flood regime directly affect the distribution, composition, and abundance of plants in the Amazon basin. Moderate flooding gives access to the dry area, the unique biology and ecology of the flooded forest (Adeney, 2009; Myster, 2007); allowing moderate flood events to maintain the high biodiversity in the Amazon. However, extreme flood events reduce the biodiversity due to different survival strategies between species of dry and flood forests (Myster, 2007).

We plan to study the flooding hydrodynamic behavior in Iquitos city due to the city's importance in the economy and development of the Peruvian Amazon. Iquitos is the largest Peruvian City in

the Amazon with a population around 1 039 372 in 2015 (Valenzuela-Yasalde, 2017). The city is the center of commerce between Peru and Brazil due to its access to river transportation.

This research will help us to understand the extreme flood process in the Amazon river near Iquitos city, propose mitigation works and reduce future life, environmental and economic impacts. A significant challenge for understanding the extreme flood process in wetland ecosystems is to obtain the controlling parameters as the spatial pattern, extent, timing, and duration of flooding (Adeney, 2009), and to use adequate model complexity to simulate floods in the Peruvian Amazon. These parameters and models are valid if, with them, we can simulate the extent of a real extreme flood like the one in 2012. Floods in riverine wetlands are caused by rising river water not correlated necessarily with local precipitation (Adeney, 2009). Other aspects could trig flooding like high ground water table, sediment transport, river morphodynamics, or artificial modifications. In this research, we suggest that the extent of flooding in Iquitos City correlates to the hydraulic regimes along the Amazon Rivers. A computer model that couples inbank and overbank hydraulic processes is required to predict flooding across the Amazon Basin. In this paper, we are using a 1D-2D coupled HEC-RAS model and compare the result with a more traditional 2D HEC-RAS model.

## 4.2 DATA

Iquitos city is the capital city of the Department of Loreto, located in the Peruvian Amazon, extending between $3°40'S$ to $3°55'S$ and $73°10'W$ to $73°25'W$ (see figure 20). Several rivers surround the city: Nanay, Guano, Itaya, and Amazonas (see figure 20). "The city was founded in the 1750s as a Jesuit mission" (The Hutchinson Encyclopedia with atlas and weather guide, 2014). Its humble start did not prepare it for what is becoming one of the most importan inland port in the world (The Columbia Encyclopedia, 2013) that have to deal with the hydro-climatology changes of the biggest river on earth. The only access to the city is by river and air. The city is on alluvial deposits on the left bank of the Amazon river (see figure 20). This city is the center of oil exploration operations and rainforest tourism (The Hutchinson Encyclopedia with atlas and weather guide, 2014). Although the city has been expanding considerably since its founding, its

extent still lies only within the Amazon valley, which is prone to flooding by high flows and changes in the river.

Geomorphology plays a crucial role in the dynamics of flooding and leads to the required data. Abad and Montoro (2013); Abad et al. (2010) show the current anabranching river dynamics near Iquitos city. In 1973, the Amazon river flowed near the central zone of Iquitos city. Throughout the years the Amazon river migrates to the east leaving dry zones where the population started to settle. These low-level areas have a higher risk of flooding in case of an extreme event or a reversal river migration. It is also possible to observe how the Nanay river confluence has been modified by the Amazon river dynamics (Abad & Montoro, 2013; Abad et al., 2010).

To study the flooding process in Iquitos city, we collected multiple data. We obtained Two ALOS PALSAR DEM files named AP_24769_FBD_F7100_RT1 and AP_24769_FBD_F7100_RT1 from Alaska Satellite Facility web site. These two files were combined and then clipped to get a base DEM for the study area. The base DEM obtained has a resolution approximately of $12.5m$ per pixel. The base DEM reports ellipsoidal elevations in whole meters. Therefore, a rounded conversion of $-21m$ was applied to obtain geoidal elevations. To deal with irregularities (as buildings and trees) a filter based on minimum values in tiles of 200 m x 200 m was applied. Since the filter reduces the resolution of the DEM, a linear interpolation was applied to obtain a refined DEM that match the available bathymetry resolution. Bathymetry surveys were carried out in the Amazon river upstream and downstream of Iquitos city on August 2010 (Frias et al., 2015) and June 2011 (Mendoza et al., 2016), respectively. Both surveys computed the bathymetry in relative elevations. We made use of the refined DEM (which present geoidal elevations) as a benchmark to compute absolute elevations. As no bathymetry data of Itaya and Nanay rivers was available, we used an empirical formulation for bed morphology calculated by RVR Meander software (Abad & Garcia, 2006). All this information was merged to generate a final DEM with a resolution of 5 m of Iquitos City; Amazon, Itaya and Nanay rivers; and the adjacent floodplains.

We collected Geology data from the National Geology Service of Peru using the web service GEOCATMIN (INGEMMET, 2014) (see Figure20). Also, we downloaded the Global Land Survey (GLS2010) collection from USGS (2015) that correspond to a terrain corrected by processing Landsat images acquired in 2008 - 2011. Finally, Global Land Cover Characterization (GLCC)

was obtained from USGS (2015) for South America. These three datasets were used to generate a land classification of the study zone and define local roughness values (Manning's coefficients).

Amazon water surface elevations were collected by the Peruvian navy from 1968 to 2014 at Iquitos city (see figure 21). The highest value ever recorded in local coordinates was 118.97 on April 19, 2012. Also, the Peruvian navy regularly reports computed river discharges and hydraulic grade lines in the principal rivers around the study area.

To project the local coordinates used by the Peruvian navy to WGS84, a correction of -30.15 m was applied to the complete set of measurements in the Iquitos station. Therefore, the water surface elevation in EGM96 at Iquitos station for the flooding peak of 2012 was 88.82 masl (meters above the sea level).

## 4.3 METHODOLOGY

In this research, we suggest that the extent of flooding in Iquitos City correlates with the hydraulic regimes along the Amazon Rivers. Due to the lateral expansion observed during a flooding event (lateral wave diffusion), a computer model that couples inbank and overbank hydraulic processes are required to accurately simulate flooding dynamics in Iquitos City. To analyze the correlation between the hydraulic profile of the rivers surrounding Iquitos City (i.e., Amazon, Nanay, and Itaya) and the flooding extent, the Hydrologic Engineering Center's River Analysis System version 5.0.3 (HEC-RAS 5.0.3) software was selected.

HEC-RAS 5.0.3 is a free river hydraulic software system (Moya Quiroga et al., 2016), maintained and periodically improved by the U.S. Army Corps of Engineers (USACE), comprising "a graphical user interface (GUI), separate hydraulic analysis components, data storage and management capabilities, graphics and reporting facilities" (Brunner, 2016b). From version 5, HEC-RAS has incorporated the capability to run 2D hydrodynamics (Brunner, 2016a). The 2D model capability is a significant improvement for future flood studies (Moya Quiroga et al., 2016). Now, HEC-RAS 5.0.3 allows running 1D, 2D and coupled 1D-2D unsteady flow modeling (Brunner, 2016a). The 2D HEC-RAS engine has the options to solve the 2-D Saint-Venant equations (also known as the Shallow Water equations) or the approximate Diffusion Wave Equations using the

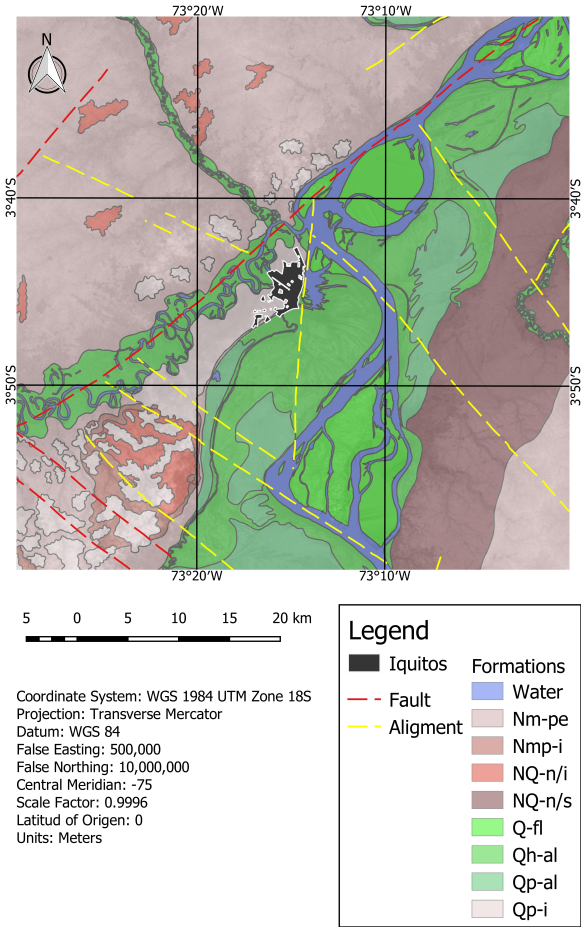


Figure 20: Study Area Geology Map

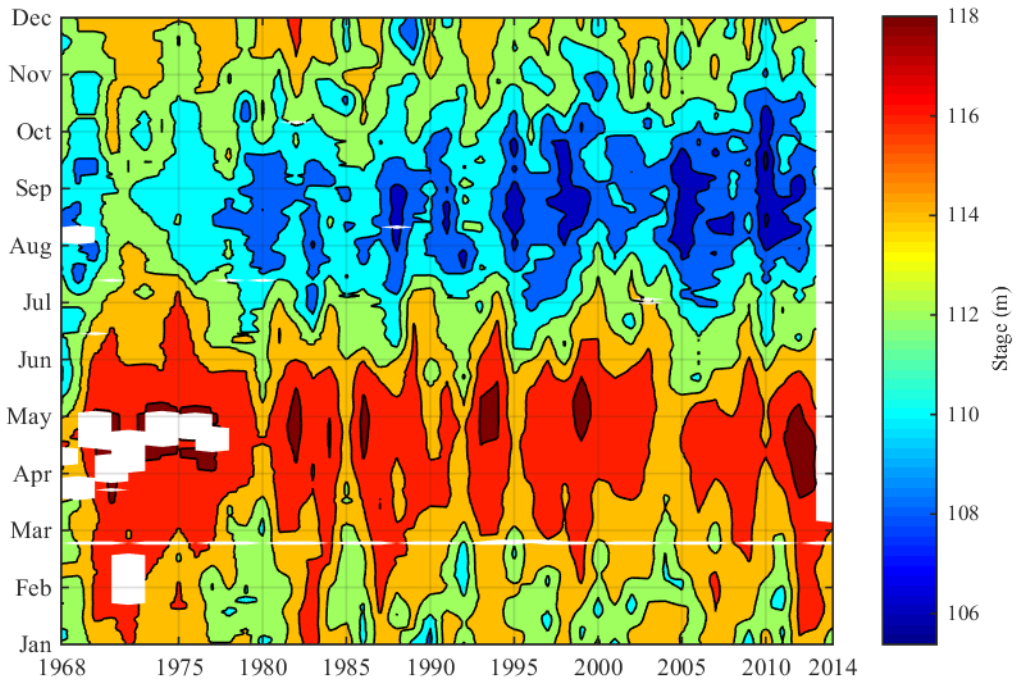


Figure 21: Amazon water surface elevation base in local datum (to obtain geoidal elevation in EGM96 substract 30.15 m).

implicit Finite Volume method, and the option to add turbulence and Coriolis effects (Brunner, 2014, 2016a; Moya Quiroga et al., 2016). The program works over structured and unstructured meshes (Brunner, 2014, 2016a). The coupled 1D-2D model assumes 1-D flow (1-D Saint Venant equations) in the main channel while 2-D flow (Shallow Water equations) in the floodplain, thus performing an iterative process between 1D and 2D solutions converging to the correct flow transfer between them. The work of Vozinaki, Morianou, Alexakis, and Tsanis (2016) shows how suitable is the use of HEC-RAS 5.0.3 with satellite extracted topographic information, as the one obtained here for Iquitos city, for modeling purposes.

In this work, we make use of a 2D and a coupled 1D-2D models. The 2D model covers the complete study area with one continuous 2D region, while the coupled 1D-2D model divides the study area into 1D and 2D regions. The coupled 1D-2D model uses 1D and 2D regions to simulate the flow in rivers and over floodplains, respectively. In all 2D regions, we selected solving the full Saint-Venant equations over the unstructured mesh. We used the "normal 2D equation domain" option as the overflow computation method to model the interface between 1D and 2D regions. The "normal 2D equation domain" option allows a more stable solution (Jarvus, 2016) because it uses normal velocities of 2D regions as lateral flows in 1D regions. However, HEC-RAS interfaces neglect the transfer of the parallel momentum to the interface momentum (As noted by Simon, Langendoen, Mendoza, and Abad (2016)).

Figure 22 shows the unique mesh for the 2D model. The 2D model mesh covers all the region of interest: Iquitos City as well the Amazon, Itaya, and Nanay rivers. We selected the region of interest such that it extends beyond the flooding stage at both sides of the rivers. Initially, we delineated the region of interest from fluvial deposits shown in the geology map (Figure 20), historical data (Figure 21), and historical aerial photographs (Landsat and Radarsat). Later, the modeling results verified that the delineated region extends appropriately. Figure 23 shows the 1D-2D model discretization using a 1D stream network, 2D meshes and lateral structures as lateral connections between 1D and 2D elements. The 1D network covers the Amazon river from Tamshiyacu town to Sinchicuy town, upstream and downstream of Iquitos city, respectively. Also, the 1D network discretizes the Itaya and Nanay rivers that flank Iquitos city from the South-West and North-East, respectively. Because the Amazon river presents two anabranching regions in the study area, the more extensive branch and restricted branches were incorporated in the 1D region; while we modeled the freely

meandering branches inside the 2D floodplain meshes. We used Three 2D meshes: The Iquitos city and two anabranching zones in the Amazon river (Tamshiyacu and Muyuy zones respectively upstream and downstream of Iquitos city).

We discretized the 2D model mesh with square cells spaced 150 m and 200 m on rivers and floodplains, respectively. The 2D mesh contains 30 631 cells and covers 1 105.756 $km^2$. Cells in rivers align with the center line of the river channel. Cells in floodplains align with North-South and East-West axes. Polygonal cells make the transition between the two types of cells alignment. Figure 24 shows a detail of the 2D model mesh around the north part of Iquitos city. A mesh sensitivity analysis using both the double and half size meshes did not show different results.

We discretize the stream network of the coupling 1D-2D model using four reaches, connected by a node just at the North-East of Iquitos City (see Figure 25). Furthermore, we discretized each reach using cross-sections. We used two reaches to discretize the Amazon river. The upstream and downstream reaches of the Amazon river use 9 and 29 cross sections along 20 km and 46 km, respectively. The Itaya and Nanay rivers use one reach each. The Itaya river uses 17 cross sections along 32 km of the river. Finally, The Nanay river uses 13 cross section along 35 km. We tried to maintain the distance between cross sections as half their width. However, we prioritize the zones where the cross section was transversal as possible to the presumed streamlines, and the beginning and end of banks to accommodate lateral connections with 2D regions.

In the coupling 1D-2D model, we used 2D regions to model anabranching zones and the floodplain area of Iquitos city. On the right side of the Amazon river, two anabranching zones were identified and modeled with 2D regions. The first zone named Tamshiyacu start downstream of Tamshiyacu town and end around 39 km upstream of Iquitos city. The Tamshiyacu mesh contains 4 488 cells and covers 178.814 $km^2$. The second zone named Muyuy start around 32 km upstream of Iquitos city and ends upstream of Sinchicuy town. The Muyuy mesh contains 2 304 cells and covers 90.072 $km^2$. These two zones were already studied in previous works (Frias et al., 2015; Mendoza et al., 2016). Similar to previous studies, we used a 2D mesh to discretize each zone. In both meshes, we used a cell size of 150 m around the meandering branches and 200 m everywhere else. The mesh in Tamshiyacu and Muyuy respectively consist of 4 488 and 2 304 cells. On the left side of the Amazon river and enclosed by the Itaya and Nanay rivers, a 2D mesh was defined

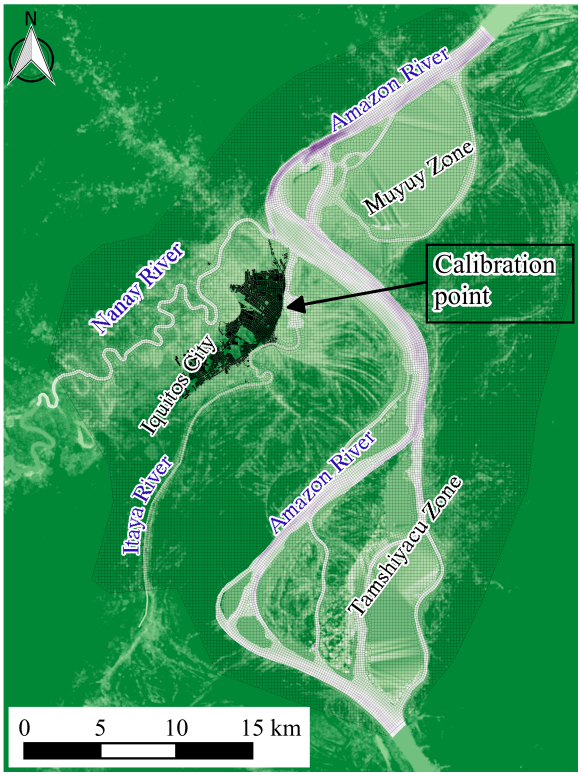


Figure 22: 2D model.

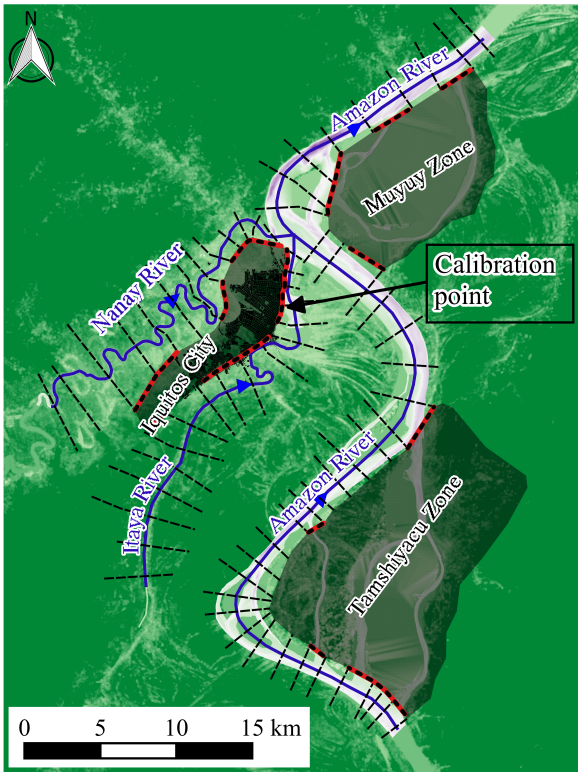


Figure 23: 1D-2D model.

to model the floodplain into which Iquitos city extends. The 2D mesh in Iquitos city has a cell size of 200 m. Figure 25 shows the mesh detail on Iquitos City.

We can see that the 1D-2D model reduce the 2D area region from the 2D model in 794.163 $km^2$ and instead make use of 68 cross sections. The reduction correspond to around 28% of the 2D mesh in the 2D model where a complete survey/bathymetry information is required. The cost saving of replace the survey/bathymetry information of an area of 794.163 $km^2$ by 68 cross sections is an advantage for the 1D-2D model.

All the topographic information was developed inside QGIS (www.qgis.org) using the RiverGIS extension (rivergis.com). The obtained geometry data was imported into HEC-RAS 5.0.3 for computation.

Both models, the 2D and the coupling 1D-2D models, use the same boundary conditions: three upstream inlets and one downstream outflow. The three inlet boundary conditions are located upstream of each river (Amazon, Itaya and Nanay rivers). The outflow boundary condition is located downstream of the Amazon river.

The upstream boundary condition in the Amazon river makes use of the Amazon river maximum discharge reported by Espinoza et al. (2013) ($55\,420\,m^3s^{-1}$) in the 2012 flood event that Iquitos city suffered. Additionally, we used the hydraulic grade line ($3.38\,10^{-5}\,m\,m^{-1}$) computed by the Peruvian navy (Servicio de Hidrografía y Navegación de la Amazonía, 2011) for Sinchicuy town as the slope parameter in the normal flow behavior selected as the downstream boundary condition.

The river discharges computed by the Peruvian navy and reported by Mendoza et al. (2016) were the base to obtain a discharge relation within rivers. The relations were applied to the Amazon river discharge to compute the discharges in the Nanay and Itaya rivers. The computed Itaya and Nanay discharges were $55.25\,m^3s^{-1}$ and $4\,817.69\,m^3s^{-1}$, respectively. The velocity ranges in the Amazon, Itaya and Nanay were respectively from 0.17 m/s to 1.3 m/s, from 0.01 m/s to 0.05 m/s, and from 0.17 m/s to 1.04 m/s. The maximum Courant-Friedrichs-Lewy (CFL) number in the three rivers were 0.16, 0.17, 0.0 7 for the Amazon, Itaya and Nanay rivers, respectively.

HEC-RAS can only apply the unsteady flow analysis over 2D regions. To compute the maximum flood area, we ran the unsteady flow analysis until it reached a steady solution. The boundary conditions were applied at the beginning and were maintained constant over the entire simulation.

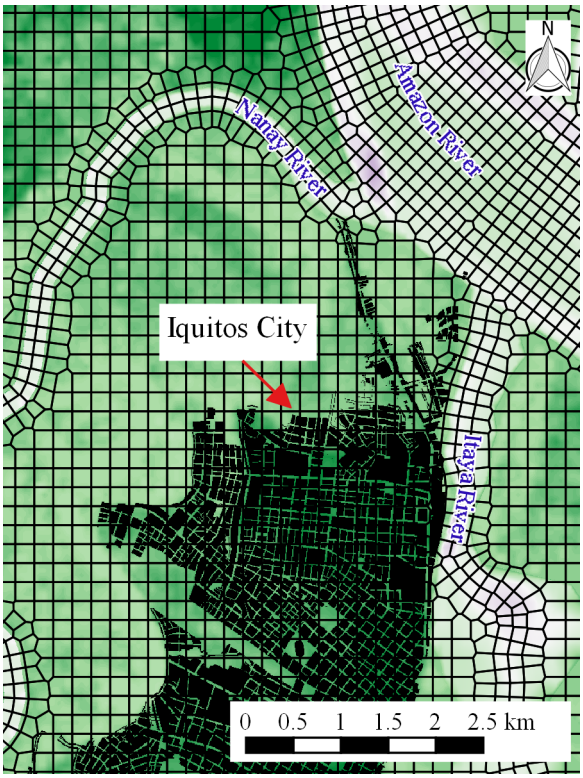


Figure 24: 2D model mesh detail.

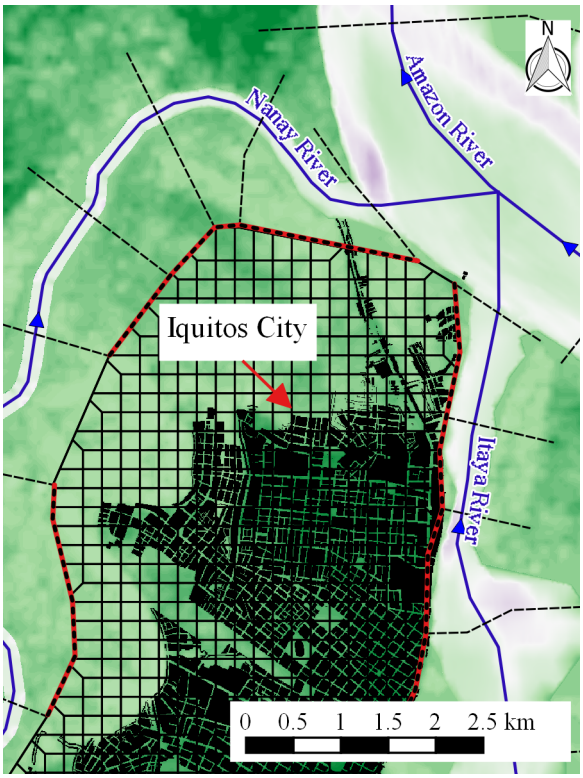


Figure 25: 1D-2D model mesh detail.

Table 1: Calibrated Manning's Numbers

| Model | Region | Manning's Number per Soil Class | | |
|---|---|---|---|---|
| | | Rivers | Floodplains | Inland |
| 2D | 2D | 0.02967 | 0.06 | 0.08 |
| 1D-2D | 1D | 0.0978 | 0.1 | 0.12 |
| | 2D | 0.035 | 0.065 | 0.085 |

We ran the models with an implicit weighting factor of 0.8. A maximum of 40 iterations per time step was used in the 1D and 2D regions, when applicable. For the 1D-2D coupling model, a maximum of 20 iterations per time steps were used on the 1D-2D interface flow calculations to converge both 2D and 1D elevations with the corresponding interface flow.

We calibrated both models based on the Peruvian navy record of April 19, 2012 (88.82 masl). The record was taken in the Itaya River close to the Peruvian navy station (see Figures 22 and 23). We start the calibration process using the Manning's number presented by Chow (1959). We compared the water surface elevation result with the record value and adjusted the Manning's numbers in the model until we reached a match with the measured elevation. Running the model multiple times and modifying the Manning's number each time showed us an order of sensitivity of elevation at the record location. Changes in the inland Manning's numbers impacted the elevation at the calibration point less than the changes in the floodplain. We start modifying the less sensible Inland values, to continue with the floodplain and ending with the river Manning's numbers. As the record has two (2) significant digits, the highest achievable accuracy is 0.005 m. We were able to achieve the highest accuracy possible using more than three (3) significant digits Manning's number in the rivers because they present more sensitivity with the water surface elevation at the record location.

Gloor et al. (2013) indicate an increase of 8% in the Amazon river monthly maxima discharge, at Obidos station, during the last 20 years. If this trend continues for another 20 years, it is expected a flood event with a discharge of 59 853.6 $m^3 s^{-1}$ in the Amazon River will occur, and the Itaya and Nanay river could have discharges of 59.67 $m^3 s^{-1}$ and 5 199.87 $m^3 s^{-1}$, respectively. We used these

values to update the upstream boundary conditions and ran a new set of computations for a future flood event impacted by climate change.

## 4.4 RESULTS

Figure 26 shows the flood extent corresponding to the flood event of 2012 as modeled by the 2D and the coupled 1D-2D models. This set of runs was used to calibrate the models. Both results show the same flooding areas. However, the 1D-2D results show $37.8 km^2$ more flooding than the 2D results. That is 10% more than shows a little bit more extended inundation in North and a more significant inundation in the South-East zone of the city.

We can see that, in both models, most of the flooding inundation occurs in the north of the city by the Nanay river flank. The flooding of the north part of Iquitos city affects essential infrastructure, as the old airport of Iquitos. We need to realize that the only two ways to access the city are by air or by the Amazon river. In case of a natural disaster, as was this flooding event, the fastest and safest way to provide help is using both airports located in the city.

The flooding of the north part of Iquitos city also activates old branches of the Nanay river leaving portions of the city either wholly isolated or with reduced access to land. A notorious feature is an area in the north of the old city airport. This area becomes surrounded by water leaving only one access by the Jiron Putumayo road. However, we need to be careful with some of the isolated areas depicted in the coupling 1D-2D model close to the interface between 1D and 2D regions. Some of the islands formed in the interface are a product of the lack of interpolation accuracy between cross sections to depict the river width variability.

The Nanay river also floods a small area in South-West of the city. Although the South-West flooding does not extend to much inside the city, it affects the new "Coronel FAP Francisco Secada Vignetta" International Airport; leaving the city without air access. This flooded area is where a greater difference occurs between the 2D and the coupling 1D-2D modeling.

On the other side, the Itaya river floods regularly every year in a south area of the city called Belen. Belen is a lowland area prone to flooding with limit access to services. Both models show

that this area will flood entirely. As shown at the Nanay river, the flooding in the Itaya river is led by the water surface elevation of the Amazon river.

The second set of runs represent an extreme 20 years future flood impacted by climate change. We call this event the "Climate Change Event". Figure 27 shows the results of the second run set. It is clear that the highest risk of flooding to Iquitos city under climate change is the Nanay river. Both models show that the Nanay river floods both city airports entirely and leaves the neighborhood at North of the old Iquitos airport completely isolated. The south of the city presents a more extensive flood area. The Itaya river continues to flood the Belen Neighborhood and penetrates further into the city. However, the center part of the city is not directly affected by flooding.

Figures 30 and 31 plot the simulation velocities of both models 2D and 1D-2D, respectively, at the north of Iquitos city for the 2012 event. The north area of Iquitos city is where the Nanay and Itaya rivers joint the Amazon river. We plot the north area of Iquitos city to study how river velocities affect the flood velocities inside the city.

The 2D simulation present high velocities in the Amazon river and low velocities in the Itaya river and the flooding zones around Iquitos city (see Figure 30). Although the 1D-2D simulation also shows low velocities in the Itaya river, the higher velocities are present in spot zones of the flooding around Iquitos city (see Figure 31). The 2D results exhibit a define branching structure while the 1D-2D results does not (compare the upper right corner of Figures 30 and 31) The inability to transfer momentum generate high-velocity spot zones in the 1D-2D results. The same process is carried through the simulation of the Climate Change event generating the same high-velocity spot locations (see Figure 33), but with higher velocity magnitudes. Both simulations show the Nanay river slowing down at it approach the Amazon River. However, the 1D-2D simulation shows a higher velocity gradient making the Nanay river velocities slowing down from a further distance before it arrives at the Amazon river.

Figures 32 and 33 plot the simulation velocities of both models 2D and 1D-2D, respectively, at the north of Iquitos city for the Climate Change event. Both model results exhibit similar velocity patterns but with higher magnitudes for the Climate Change event than the 2012 event, as expected. For both the 2012 flooding event and the Climate Change event, the 1D-2D model suggests that the city will experience velocities until 2 $m/s$ while the 2D model predicts velocities not higher than 1.1 $m/$ (See also statistic results in Table 3).

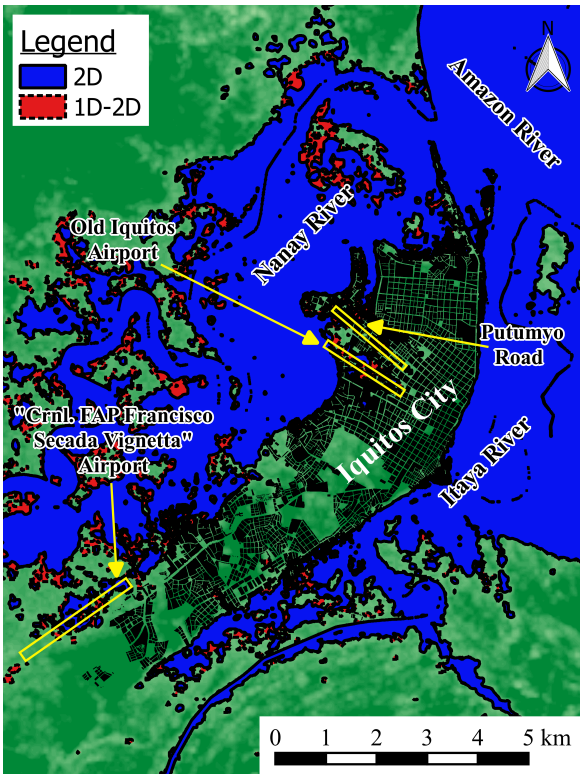


Figure 26: 2012 results: Comparison between the 2D and the 1D2D model results around Iquitos City.

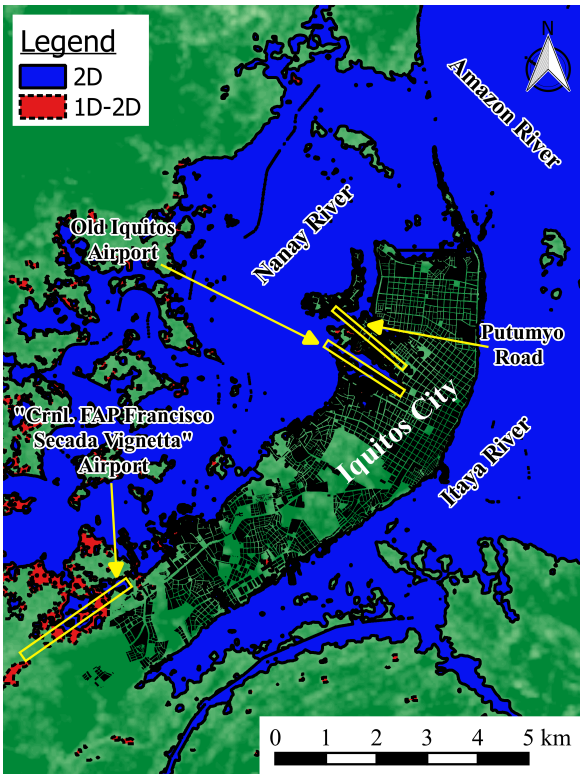


Figure 27: Climate Change results: Comparison between the 2D and the 1D2D model results around Iquitos City.

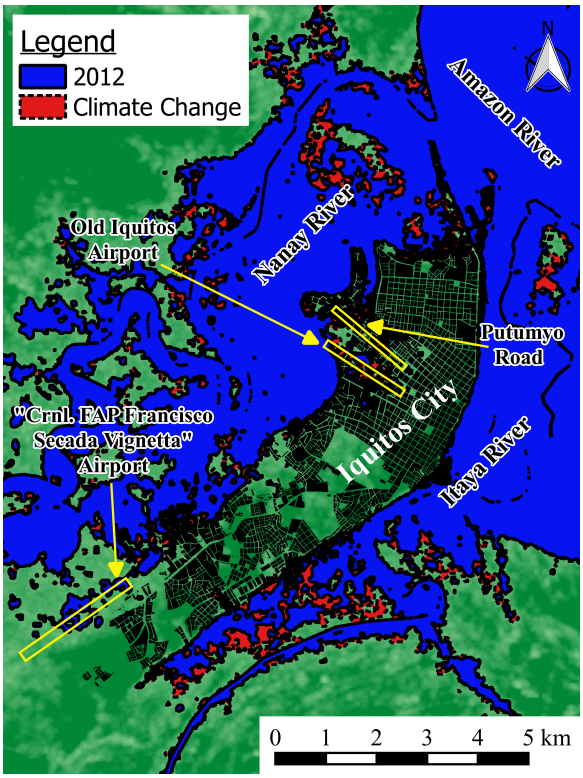


Figure 28: 2D model results: Comparisons between the 2012 and the climate change results

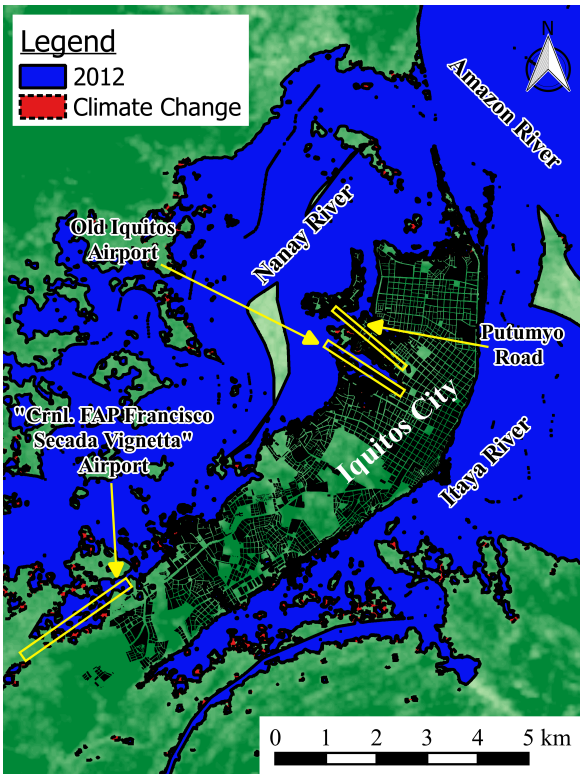


Figure 29: 1D-2D model results: Comparisons between the 2012 and the climate change results

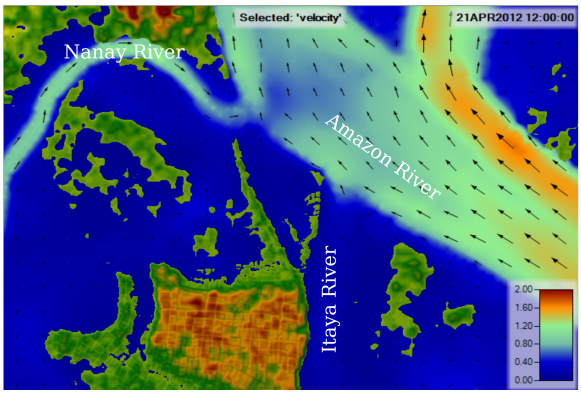


Figure 30: Velocity results of the 2D model for the 2012 flood event

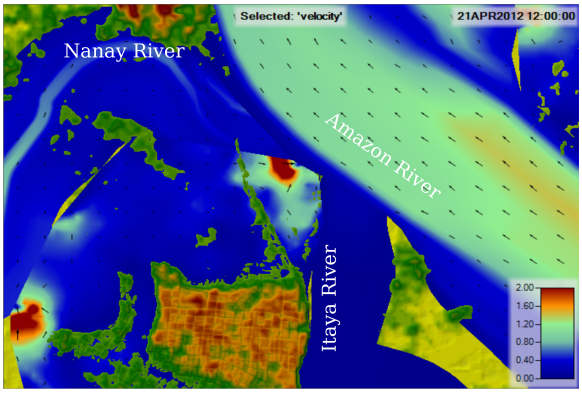


Figure 31: Velocity results of the 1D-2D model for the 2012 flood event

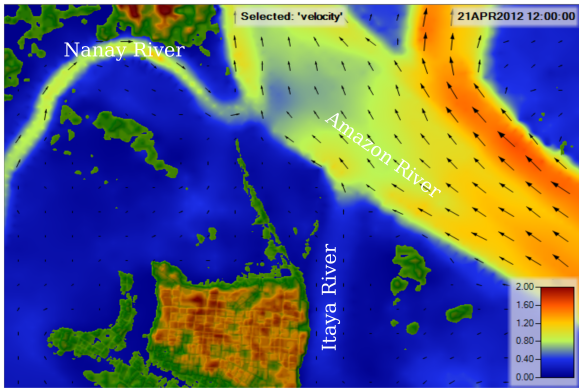


Figure 32: Velocity results of the 2D model for the Climate Change event

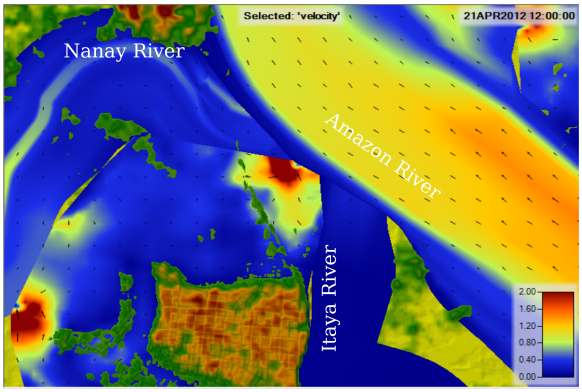


Figure 33: Velocity results of the 1D-2D model for the Climate Change event

We include statistic results of flood depth inside Iquitos city in Table 2. Comparison of the event record against simulation results indicates a better correlation of the statistical results from the 1D-2D model. The 1D-2D Model present a mean flood depth that differs from the 2012 event in 0.2 $m$. Both the record and the 1D-2D Model have the same maximum flood depth and very similar standard deviation (2.84 $m$ and 2.83 $m$, respectively). On the other hand, the 2D model shows a lower mean, maximum, and standard deviation. We can see that the 2D model underestimate the flood depth inside Iquitos city. In contrast, the 1D-2D model simulation predicts a more accurate flood depth on average.

Statistics of the Climate Change event show higher values for the 1D-2D model. The 1D-2D model is more conservative than the 2D model for a future event impacted by climate change. The 1D-2D model will predict an inundation depth in average 0.41 $m$ above the 2D model. Due to the uncertainties in how the climate will change, we recommend using the more conservative result from the 1D-2D model.

We include statistic results of flow velocities inside Iquitos city in Table 3. No velocity record exists of the 2012 flood event that hit Iquitos city. However, the comparison between both 2D and 1D-2D model result statistics indicates that 1D-2D results present the highest values. A review of the velocity plots in Figure 33 reveal high-velocity spots due to the limitation of the model to transfer momentum between the 1D and 2D regions.

Table 2: Flood Depth Statistics

| Statistics | 2012 Event | | | Climate Change Event | |
|---|---|---|---|---|---|
| | Record | 2D Model | 1D-2D Model | 2D Model | 1D-2D Model |
| Mean | 3.43 | 2.93 | 3.23 | 3.03 | 3.44 |
| Maximum | 23.55 | 22.55 | 23.55 | 23.78 | 24.31 |
| Minimum | 0.82 | 0 | 0 | 0 | 0 |
| Std. Dev. | 2.84 | 2.78 | 2.83 | 2.9 | 2.92 |

Table 3: Flood Velocity Statistics

| Statistics | 2012 Event | | Climate Change Event | |
|---|---|---|---|---|
| | 2D Model | 1D-2D Model | 2D Model | 1D-2D Model |
| Mean | 0.065 | 0.246 | 0.076 | 0.289 |
| Maximum | 1.02 | 2.017 | 1.016 | 2.301 |
| Minimum | 0 | 0 | 0 | 0 |
| Std. Dev. | 0.078 | 0.32 | 0.087 | 0.357 |

Table 4: Model Flow Computation Time

| Model | Flow Computation Time per Event | |
|---|---|---|
| | 2012 Event | Climate Change Event |
| 2D | 5.19 min. | 5.16 min. |
| 1D-2D | 35.29 min. | 125.03 min. |

Table 4 presents the flow computation time of each run. The times shown do not include the additional computations to assemble the geometry, preprocessing, or postprocessing. However, all the three of those additional computations took less than one minute for eachof the runs. The coupling 1D-2D runs took more time than the 2D runs due to multiple iteration requirements to converge the results in 1D reaches with 2D mesh solutions by the lateral interface coupling.

## 4.5 DISCUSSION

As we explained before, Iquitos city is flanked by the Itaya and the Nanay rivers. Being flanked by two (2) rivers limits the city's development. Throughout the years, the city has been developing in the direction Northeast to Southwest. The growth of the city, due to its importance as a commercial hub between Brazil and Peru, has pushed occupation into the Nanay floodplains in the north.

The coupling 1D-2D model makes use of fewer elements than the 2D model, as 1D streams replace large regions of 2D cells. For some types of software as HEC-RAS, with a limit number of 2D cells, the coupling 1D-2D model approach allows to simulate more massive extensions or increase the 2D mesh resolution in specific zones. However, the coupling 1D-2D model requires more computational time due to the multiple iterations between the 1D and 2D runs executed for convergence in their connecting interfaces.

There are uncertainties in the estimation of the Manning's number. The uncertainties can be reduced by calibration if more measurements are taken in future flood events. Although depth calibration can adjust the model to centimeters, this uncertainty could mean several cubic meters

per second for wide rivers as the ones presented here. Based on the results of the event impacted by the climate change, the more secure zones to place sensitive infrastructure is in higher elevation zones closer to the Itaya River than the Nanay river. We recommend that future development take place in the Southwest area of the city. Flood modeling is the ideal tool to help the public and private sectors to decide which areas to develop and to quantify the investment risk.

All results show how the water elevation in the Amazon river generate a backwater effect in the Nanay and Itaya rivers. As the Amazon river profile defines the flooding extension around Iquitos city, migration of the Nanay and Itaya rivers will have little effect over the flooded areas. On the other hand, geomorphologic changes in the Amazon river could impact the results obtained here. However, due to the low hydraulic slope and the width of the Amazon river, we believe that any geomorphologic change in the Amazon river will be attenuated to maintain a similar hydraulic profile. We support this idea observing that the substantial increase of flow due to climate change does not impact the flooding extension in the same proportion.

## 4.6 CONCLUSIONS

In this research, we were able to model the Amazon river for an extension of 66.5 km. Also, the Nanay and Itaya rivers were modeled for extensions of 35.0 km and 31.2 km, respectively. We were able to model the three (3) rivers using a 2D model and a coupling 1D-2D model. Both models were able to capture the meandering and anabranching structures in the rivers.

This research allows us to compare, with a real application, the advantages of a coupling 1D-2D model against a more traditional 2D model. We conclude that both models produce very similar results. If the computer time is not a limitation, the coupling 1D-2D model could help to improve the 2D resolution and extend the study area. Although, The computaion time in the 1D-2D model was longer, the reduction of 794.163 $km^2$ of survey/bathymetry required justify the selection of 1D-2D models over pure 2D models.

Statistic results indicate that the 1D-2D model is more accurate to simulate the flood depth. However, a review of the results highlights the importance of including the transfer of momentum in the simulations to describe the flow distribution correctly.

The results show that future development in Iquitos city should take place in the Southwest area of the city. Additionally, city developers should avoid occupying the floodplain of the Nanay river in the North, as was happening in the recent years.

We propose following studies of future high flooding events as a future research plan.

# 5.0 CONCLUSIONS

Chapter 2 presents the equations for the horizontal and vertical coupling strategies of the depth-averaged (2D) and cross section-averaged (1D) Reynolds-Averaged Navier-Stokes equations to simulate overbank flow in compound channels. The author includes a rigorous derivation of the equations in Appendix A. The horizontal coupling method combines 2D floodplain models at both sides of a 1D cross section-averaged model for the flow in the main channel. The vertical coupling method combines a 2D model for the overbank flow with a 1D cross section-averaged model for the flow inside the channel section.

In the horizontal coupling method, the mass transfer between the 1D and 2D model regions is the lateral unit discharge at the interface, while in the vertical coupling method, the mass transfer is given by the vertical velocity at the interface. Two terms describe the momentum transfer between 1D and 2D models, an advective momentum transfer due to the exchange of mass, and a diffusive momentum transfer due to the shear stress acting on the interface between 1D and 2D model regions. The research evaluated the magnitudes of these exchange terms for overbank flow in a compound meandering channel.

Methods that couple 1D and 2D flow models solve the main flow variables (discharge, depth-averaged velocities, water depth) within the 1D or 2D regions, and approximate the values at the interfaces by constituent equations based on the main variables and empirical or standard formulations. The approximated values of the variables at interfaces have a direct impact on the modeled main channel flow. The transfer terms (mass and momentum) for the vertical-coupling method were smaller than those for the horizontal-coupling method.

In the horizontal-coupling approach, the streamwise and lateral advective momentum transfer terms were smaller in bends and more substantial in the straight portion between bends.

On the contrary, the vertical-coupling approach presented a fairly constant width-averaged advective momentum transfer magnitude along the full meander wavelength, whereas the shear stress was similar to that of the horizontal-coupling method (maximum values in the bends and close to zero in the cross-overs). Vertical-coupling methods can take advantage of this behavior by simplifying the numerical solution approach. Vertical velocities at the horizontal interface for the vertical-coupling approach were higher near the bends of the meandering channel, see Figure 9. This vertical flow generates turbulence and flow resistance near the bends, which 2D codes are not able to simulate but could be incorporated by locally increasing the flow resistance parameters.

The vertical coupling approach describe the flow in the river using two velocity variables (In-bank and over-bank velocities) instead of the only one used by the horizontal approach. Having vertically two velocities instead of one not only add information but also reduce the flow region represented by the 1D velocity. A smaller regions improve the discretization and allow to approximate more precisely other parameters computed from velocity as shear stress, sediment transport and river dynamics.

Chapter 3 investigates the ability of horizontally- and vertically-coupled 1D channel and 2D floodplain flow models, in use by industry and governmental agencies today, to simulate the overbank flow conditions of a meandering channel.

The research shows that mass and momentum transfers across the vertical channel-floodplain interface in the horizontal coupling method are one to two orders of magnitude higher than those across the horizontal in-bank-overbank interface in the vertical coupling method (compare Figure 17 and Figure 19). A vertical coupling approach, therefore, should be able to more accurately simulate overbank channel hydraulics, which was demonstrated by the results shown in Figure 15.

For channels not aligned with the valley centerline, transfer of mass between channel and floodplain through a vertical interface in the horizontal coupling method is as large as the streamwise transfer in the overbank flow itself. Simple horizontal coupling strategies that use, for example, weir equations cannot adequately simulate the interactions, such as flow steering, between in-channel and floodplain, as shown by Figure 15(b) (TELEMAC-2D) and Figure 15(c) (HEC-RAS).

A vertical coupling approach implicitly accounts for the lateral mass and momentum exchange between the floodplain and overbank zone above the channel. Also, it can account for the transfer of mass and momentum from overbank to in-bank and vice-versa through empirical relations, thereby

further improving the simulated flow hydraulics in and adjacent to the channel. Here, the author computed the empirical relations on width-averaged properties as the channel model (OpenFOAM) was one-dimensional. However, the vertical streamwise and lateral advective momentum transfer terms were not adequately simulated (Figure 19(b)), which caused discrepancies between observed and simulated hydraulics. The strongly, three-dimensional flow in meandering channels, and therefore the lateral variations in vertical velocity and momentum on the bankfull interface, cannot be adequately represented by a 1D model. Improved empirical relations are needed to more accurately simulate the transfer of mass and momentum between in-bank and overbank flow when using a vertical coupling method.

Chapter 4 uses a coupling approach to study flooding in Iquitos City. The study models the three (3) rivers around Iquitos City (Amazon, Nanay and Itaya rivers) using a 2D model and a coupling 1D-2D model. Both models were able to capture the meandering and anabranching structures in the rivers.

This research allows us to compare, with a real application, the advantages of a coupling 1D-2D model against a more traditional 2D model. The results show that both models produce similar flooding extensions. If the computer time is not a limitation, the coupling 1D-2D model could help to improve the 2D resolution and extent of the study area. Although, The computation time in the 1D-2D model was longer, the replacement of an area of 794.163 $km^2$ where a 2D survey/bathymetry is required with a survey/bathymetry of 63 cross-sections reduce the overall project cost. Also, the result statistics show the superior accuracy of the 1D-2D model to predict flood depth. However, the flow velocity results highlight one more time the importance of considering the momentum transfer in the coupling strategy approaches.

The study shows that future development in Iquitos city should take place in the Southwest area of the city. Additionally, city developers should avoid occupying the floodplain of the Nanay river in the North, as was happening in recent years.

This thesis shows that a computer model that couples inbank and overbank hydraulic processes is required to predict flooding across the Amazon Basin. The simulations show the correlation between the hydraulic regimes along the Amazon River and the extent of flooding in Iquitos City. Also, The research shows that the extent of flooding in Iquitos City will increase due to observed and forecasted changes in hydraulic regimes in the Amazon Basin.

As Chapter 3 describes: The HEC-RAS code does not account for momentum transfer between the 1D and 2D regions. This research included a full 2D model to account for a complete horizontal coupling approach. However, The author identifies, as a future research opportunity, incorporate the momentum transfer in the HEC-RAS code and compare the results of this new code with the results presented in this thesis.

Also, Figure 15 in Chapter 3 shows how each model produce different flow velocity distributions. Different velocity distributions will present different erosion and deposition zones of fine particles. The above sediment transport difference will produce a difference in the morphological dynamics of the river. Higher velocities at the middle of the river plain, as the vertical coupling approach predict, could straight the channel; while higher velocities downstream of the bends, like the 2D model shows, could increase the downstream transport of bends; and higher velocities at the outer side of bends could increase their curvature and promote the generation of cutoffs. It is the opinion of the author that this research can be extended to study what coupling approach could improve the sediment transport and morphodynamic river models from the base of providing more accurate flow velocity results.

This study identifies the necessity of future research in developing a vertical coupling approach code to improve flood simulations. A good starting point for the above code development is the equations presented in Chapter 2 that include the highly recommended mass and momentum transfer terms in the interfaces. To reduce the computation time presented in the existing coupling codes, the author suggests analyzing the possibility of algebraic solve the discretization of the 1D and 2D equations together as only one matrix system.

# APPENDIX A

# DERIVATION OF THE GOVERNING EQUATIONS FOR HORIZONTAL AND VERTICAL COUPLING OF ONE- AND TWO-DIMENSIONAL OPEN CHANNEL FLOW MODELS

## A.1 INTRODUCTION

Many textbooks of open-channel flow present the derivation of the one-dimensional (1D) and two-dimensional (2D) shallow water equations (e.g., Liggett, 1994). However, these equations do not include the terms arising at the interfaces between 1D and 2D model regions that describe the transfer of mass and momentum across them when they are coupled. For completeness, herein, the governing equations (mass and momentum) for 1D and 2D models with permeable interfaces are derived from the three-dimensional, incompressible Reynolds-Averaged Navier-Stokes (RANS) equations. The equations are formulated in a Cartesian coordinate system $(x, y, z)$ with the corresponding velocity components $(u_x, u_y, u_z)$. The $x$-axis is directed downvalley, the $y$-axis is directed across the valley from right to left, and the $z$-axis is directed vertically upward.

## A.2 CONSERVATION OF MASS

The mass conservation equation is presented in the sections below in 1D and 2D forms that can be coupled both horizontally and vertically.

### A.2.1 Two-dimensional mass conservation equation

Integrating the three-dimensional mass conservation equation for an incompressible flow ($\nabla \cdot \vec{u} = 0$) over the water depth $h$ between elevations $z_b$ and $z_t$ (see Figs. 34 and 35) and applying the Leibniz rule, yields the 2D depth-averaged mass conservation equation:

$$\frac{\partial q_x}{\partial x} + \frac{\partial q_y}{\partial y} - G|_{z_t} + G|_{z_b} = 0 \tag{A.1}$$

where $q_x$ and $q_y$ are the unit discharges in $x$- and $y$-direction, respectively, and $G$ is the mass flux through the surfaces at the top $z_t$ and bottom $z_b$

For the two coupling procedures introduced below the upper boundary of the 2D region is the water free surface. Using the kinematic condition for a water free surface, the mass flux through the upper surface can be written as:

$$G|_{z_t} = -\frac{\partial \zeta}{\partial t} \tag{A.2}$$

where $\zeta$ is the water surface elevation and $t$ is time. The lower surface of the 2D region is a solid wall (floodplain ground surface) in case of horizontal coupling and can be either a solid wall or permeable interface (between 1D and 2D regions) in case of vertical coupling. The mass transfer through the lower, stationary surface (assumed to be horizontal below) is defined as:

$$G|_{z_b} = \begin{cases} -u_z|_{z_b} & \text{if permeable surface} \\ 0 & \text{if solid surface} \end{cases} \tag{A.3}$$

### A.2.2 One-dimensional mass conservation equation

Integrating Eq. (A.1) across the channel between distances $y_r$ and $y_l$ (it is assumed that the channel centerline is aligned with the $x$-axis and this stream channel direction is denoted hereon as $s$) and applying the Leibniz rule, yields the 1D mass conservation equation:

$$\frac{\partial Q}{\partial s} - H|_{y_l} + H|_{y_r} - \int_{y_r}^{y_l} \left( G|_{z_t} - G|_{z_b} \right) dy = 0 \tag{A.4}$$

where the flow rate is $Q = \int_{y_r}^{y_l} q_s dy$. The mass flux $H$ through the vertical interfaces defined at the position of the margins for bankfull conditions $y = y_l$ and $y = y_r$ is defined as (for brevity only shown for $y = y_l$):

$$H|_{y_l} = q_s|_{y_l} \frac{\partial y_l}{\partial s} - q_y|_{y_l} \tag{A.5}$$

In both coupling approaches the bottom surface of the 1D model region is a solid wall (channel bottom), that is $G|_{z_b} = 0$. In case the top surface is a free surface, the integral of $G|_{z_t}$ from Eq. (A.4) yields

$$- \int_{y_r}^{y_l} G|_{z_t} dy = \int_{y_r}^{y_l} \frac{\partial \zeta}{\partial t} = \frac{\partial A}{\partial t} \tag{A.6}$$

where $A$ is cross-sectional area of the flow. Further, it was assumed that the interfaces at $y_l$ and $y_r$ are dependent on time. For an upper free surface the 1D mass conservation equation then reads

$$\frac{\partial A}{\partial t} + \frac{\partial Q}{\partial s} - H|_{y_l} + H|_{y_r} = 0 \tag{A.7}$$

### A.2.3 Horizontal coupling of 1D and 2D models

Figure 34 illustrates the horizontal coupling procedure. The 1D model region covers the inbank and central overbank flow region, while the 2D model region covers the left and right overbank flow regions. Notice that the two floodplain regions do not directly interact, since mass and momentum need to be transferred through the 1D region.

Equation (A.7) describes the 1D continuity equation for the 1D region, which is delimited by the channel walls (channel bottom and banks), interfaces with 2D model regions when flow is

overbank, and a top free surface. The channel walls are assumed to be impermeable. The mass flux $H$ between 1D and 2D regions is zero when the flow is inbank and equals the unit normal discharge through the 1D-2D interface, $q_n$, when flow is overbank, that is:

$$H = \begin{cases} -q_n & \text{if } \zeta > z_{fp} \\ 0 & \text{if } \zeta \leq z_{fp} \end{cases} \tag{A.8}$$

where $z_{fp}$ is the floodplain elevation at the channel margin.

The 2D region is bounded by the water surface at the top, a solid wall at the bottom (floodplain ground surface), and a permeable vertical interface with the 1D region. The 2D mass conservation equation becomes the standard 2D shallow water equation (e.g., Eq. (2.79) in Wu (2008)).

### A.2.4 Vertical coupling of 1D and 2D models

Figure 35 illustrates the vertical coupling approach. The 1D model region covers the inbank region, while the 2D model region overlies the 1D region and covers the entire overbank flow region (left, central, and right).

The 1D region is bounded by the bottom and banks and a top permeable interface with the 2D model region. Eq. (A.4) can then be written as:

$$\frac{\partial Q}{\partial s} = \int_{y_r}^{y_l} G|_{z_t} dy \tag{A.9}$$

where the right-hand side of Eq. (A.9) is defined as:

$$-\int_{y_r}^{y_l} G|_{z_t} dy = \begin{cases} \dfrac{\partial A}{\partial t} & \text{if } \zeta < z_{fp} \\ B_{z_t} \tilde{u_z} & \text{if } \zeta \geq z_{fp} \end{cases} \tag{A.10}$$

where $B_{z_t}$ is the channel top width and $\tilde{u_z}$ is the mean vertical velocity at the interface between 1D and 2D model regions. The tilde denotes the average value over the width of the 1D-2D interface. If the interface is not horizontal, the normal velocity to it should be used instead.

The transfer of mass across the interface with the 2D region can be represented by a vertical column of water with length $d$. The mass conservation equation (the combination of Eqs. A.9 and A.10) can then be written in a more generic form as:

$$B\frac{\partial \eta}{\partial t} + \frac{\partial Q}{\partial s} = 0 \tag{A.11}$$

where $B$ is the channel width of the flow in the 1D region and

$$\eta = \begin{cases} \zeta & \text{if } \zeta < z_{fp} \\ \tilde{d} & \text{if } \zeta \geq z_{fp} \end{cases} \tag{A.12}$$

when the transfer of mass across the transversal direction of the 1D flow is approximately constant, $\tilde{d}$ becomes $d$. $\tilde{d}$ or $d$ is the coupling term in the vertical approach and replaces $h$ in the 1D equations, leaving the same number of unknowns as equations. Therefore, the vertical coupling approach computes $\tilde{d}$ or $d$ during the same process of solving the set of equations.

The 2D model region is bounded by the water free surface, a wall on the floodplain ground surface, and a permeable interface above the channel. Eq. (A.1) is then written as:

$$\frac{\partial h}{\partial t} + \frac{\partial q_x}{\partial x} + \frac{\partial q_y}{\partial y} + G|_{z_b} = 0 \tag{A.13}$$

where $G|_{z_b}$ is given by Eq. (A.3) in which the vertical velocity $u_z|_{z_b}$ can be replaced by $\partial \tilde{d}/\partial t$. Further, $G|_{z_t}$ was represented by Eq. (A.2) with $\zeta$ replaced by $h$.

## A.3 CONSERVATION OF MOMENTUM

In the following analysis, shallow water hypothesis is assumed, that is, the horizontal length scale is much larger than the vertical length scale. The vertical momentum equation can then be simplified as $\partial p/\partial z = -\rho g$, which after integration yields the hydrostatic pressure distribution $p = \rho g(\zeta - z)$.

Further, the Reynolds stresses $\tau_{xz}$ and $\tau_{yz}$ are much larger than $\tau_{xx}$, $\tau_{xy}$, and $\tau_{yy}$. The normal Reynolds stresses are therefore omitted, however $\tau_{xy}$ is retained as it can be important near vertical walls.

### A.3.1 Two-dimensional momentum conservation equation

Integrating the momentum equations in horizontal direction (for example, Eq. (4.15) in Kundu (2010) for $i = 1, 2$) over the water depth $h$ between elevations $z_b$ and $z_t$, applying the Leibniz rule, and assuming the shallow water hypothesis, yields the following 2D depth-averaged momentum equations in $x$- and $y$-direction:

$$\frac{\partial q_x}{\partial t}+\frac{\partial(\beta_{xx}\bar{u_x}q_x)}{\partial x}+\frac{\partial(\beta_{xy}\bar{u_y}q_x)}{\partial y}+gh\frac{\partial \zeta}{\partial x}-u_x|_{z_t}G|_{z_t}+u_x|_{z_b}G|_{z_b} = \frac{1}{\rho}\left[\frac{\partial h\bar{\tau}_{xy}}{\partial y}+\tau_x|_{z_t}-\tau_x|_{z_b}\right] \quad \text{(A.14)}$$

$$\frac{\partial q_y}{\partial t}+\frac{\partial(\beta_{xy}\bar{u_x}q_y)}{\partial x}+\frac{\partial(\beta_{yy}\bar{u_y}q_y)}{\partial y}+gh\frac{\partial \zeta}{\partial y}-u_y|_{z_t}G|_{z_t}+u_y|_{z_b}G|_{z_b} = \frac{1}{\rho}\left[\frac{\partial h\bar{\tau}_{xy}}{\partial x}+\tau_y|_{z_t}-\tau_y|_{z_b}\right] \quad \text{(A.15)}$$

where the overbar denotes depth-averaged variables, $\beta$ is the momentum correction factor (assumed equal to one hereafter), and $\tau_x$ and $\tau_y$ are shear stresses acting on the top and bottom surface in $x$- and $y$-direction, respectively.

The upper surface ($z = z_t$) in the 2D computational region is the water free surface and is assumed frictionless, that is $\tau_i|_{z_t} = 0$. The lower surface can be either the interface between the 1D and 2D computational regions (in case of vertical coupling) or is the the floodplain ground surface. In the latter case the bottom shear stress is modeled using the friction slope $S_f$, that is

$$\tau_i|_{z_b} = \rho g h S_{f_i} \quad \text{(A.16)}$$

### A.3.2 One-dimensional momentum conservation equation

Assuming the channel is aligned with the $x$-axis and denoting this stream channel direction by $s$, the 1D momentum conservation equation is obtained by integrating Eq. (A.14) across the channel between lateral distances $y_r$ and $y_l$. Applying the Leibniz rule, substituting Eq. (A.16), assuming a solid channel bed ($G|_{z_b} = 0$) and rearranging terms yields:

$$\frac{\partial Q}{\partial t} + \frac{\partial UQ}{\partial s} + gA\left(\frac{\partial \tilde{\zeta}}{\partial s} + S_f\right) - (\bar{u}_s H)|_{y_l} + (\bar{u}_s H)|_{y_r} - (B\tilde{u}_s\tilde{G})|_{z_t} - \frac{1}{\rho}\left[(h\bar{\tau}_s)|_{y_l} - (h\bar{\tau}_s)|_{y_r} + (B\tilde{\tau}_s)|_{z_t}\right] = 0 \quad \text{(A.17)}$$

where $U$ is the cross-sectional average velocity weighted by the unit discharge and $\tilde{\tau}_s = \int_{y_r}^{y_l} \tau_s dy/B$ is the average streamwise shear stress. It was assumed that cross stream variations of the term $u_z G$ at the upper surface $z_t$ are negligible and variables can be represented by their laterally-averaged values. The shear stresses acting on the solid margins $y_l$ and $y_r$ are incorporated into the friction slope $S_f$.

### A.3.3 Horizontal coupling of 1D and 2D models

In the horizontal coupling method, the 1D model region has at the top the water free surface. The 1D momentum conservation equation (Eq. A.17) reduces to:

$$\frac{\partial Q}{\partial t} + \frac{\partial UQ}{\partial s} + gA\left(\frac{\partial \zeta}{\partial s} + S_f\right) - (\bar{u}_s H)|_{y_r}^{y_l} - \frac{1}{\rho}(h\bar{\tau}_s)|_{y_r}^{y_l} = 0 \quad \text{(A.18)}$$

where the tilde on the water surface elevation has been dropped as it is assumed to be horizontal in the transverse direction of the 1D model region (note, the 3D numerical model presented in the main paper confirms this assumption for the evaluated compound meandering channel), and the mass flux $H$ is defined by Eq. (A.8). The last two terms in Eq. (A.18) account for the transfer of momentum due to mass crossing the 1D-2D interface and to the shear stress acting on the same interface.

The 2D model region is bounded vertically by the free water surface and by the wall represented by the floodplain ground surface. The 2D momentum equation in the $x$-direction (Eq. A.14) reads:

$$\frac{\partial q_x}{\partial t} + \frac{\partial \bar{u}_x q_x}{\partial x} + \frac{\partial \bar{u}_y q_x}{\partial y} + gh\left(\frac{\partial \zeta}{\partial x} + S_{f_x}\right) = \frac{1}{\rho}\frac{\partial h\bar{\tau}_{xy}}{\partial y} \tag{A.19}$$

A similar equation can be developed for the y-direction. The local momentum flux, $\bar{u}_s H + h\bar{\tau}_s/\rho$ at the interface with the 1D model region is estimated from the 2D solution at the boundary between 1D and 2D domains.

### A.3.4 Vertical coupling of 1D and 2D models

For the vertical coupling approach, the 1D model region is bounded by the channel bottom and banks and either the water free surface when the flow is inbank or a permeable interface with the overlying 2D model region when the flow is overbank. The 1D momentum conservation equation (Eq. A.17) reads

$$\frac{\partial Q}{\partial t} + \frac{\partial UQ}{\partial s} + gA\left(\frac{\partial \zeta}{\partial s} + S_f\right) - (B\tilde{u}_s\tilde{G})|_{z_t} - \frac{1}{\rho}\left[(B\tilde{\tau}_s)|_{z_t}\right] = 0 \tag{A.20}$$

The last two terms in Eq. (A.20) denote momentum transfer through a surface at $z = z_t$. For a free surface these terms disappear and the classic 1D St. Venant equation is obtained.

The 2D model region is bounded vertically by the water free surface, a solid bottom surface on the floodplain, and a permeable bottom surface above the channel. The momentum conservation equations in $x$-direction reads:

$$\frac{\partial q_x}{\partial t} + \frac{\partial \bar{u}_x q_x}{\partial x} + \frac{\partial \bar{u}_y q_x}{\partial y} + gh\frac{\partial \zeta}{\partial x} + (u_x G)|z_b = \frac{1}{\rho}\left[\frac{\partial h\bar{\tau}_{xy}}{\partial y} - \tau_x|_{z_b}\right] \tag{A.21}$$

A similar equation can be develop for the $y$-direction. The last term on both, left- and right-hand side in the above equation denotes the transfer of momentum through the bottom surface. The flux

$G|_{z_b}$ is given by Eq. (A.3) with the vertical velocity $u_z|_{z_b}$ replaced by $\partial d/\partial t$. On the floodplain ground surface the boundary shear stress is calculated using a friction slope given by Eq. (A.16).

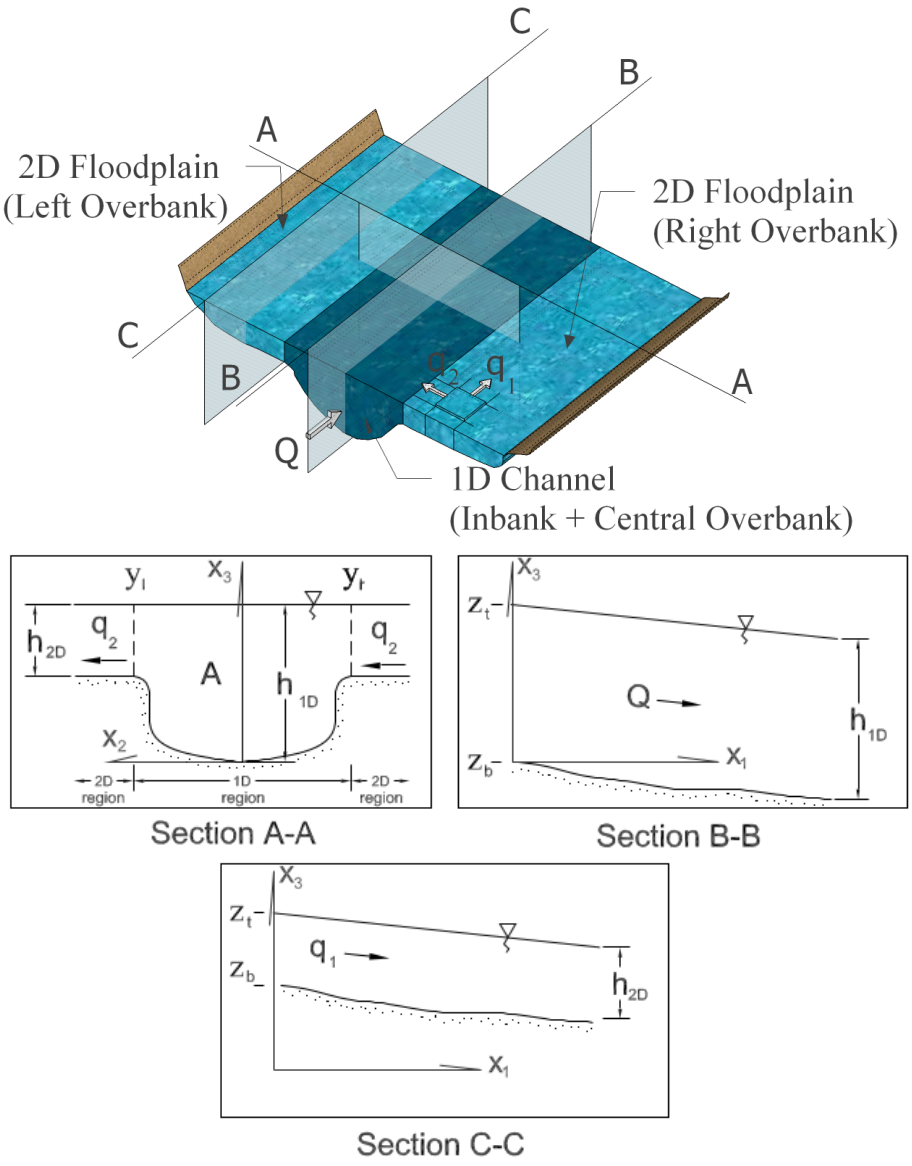


Figure 34: Horizontal coupling method. Top figure: three-dimensional view of the coupling of 1D (inbank+central overbank) and 2D (left+right overbanks) flows. Bottom figures: A-A: transversal cross section, B-B: longitudinal profile along the main channel, and C-C: longitudinal profile along the floodplain channel. Notice that the left floodplain (overbank) is separated from the right floodplain (overbank) region by the 1D region.

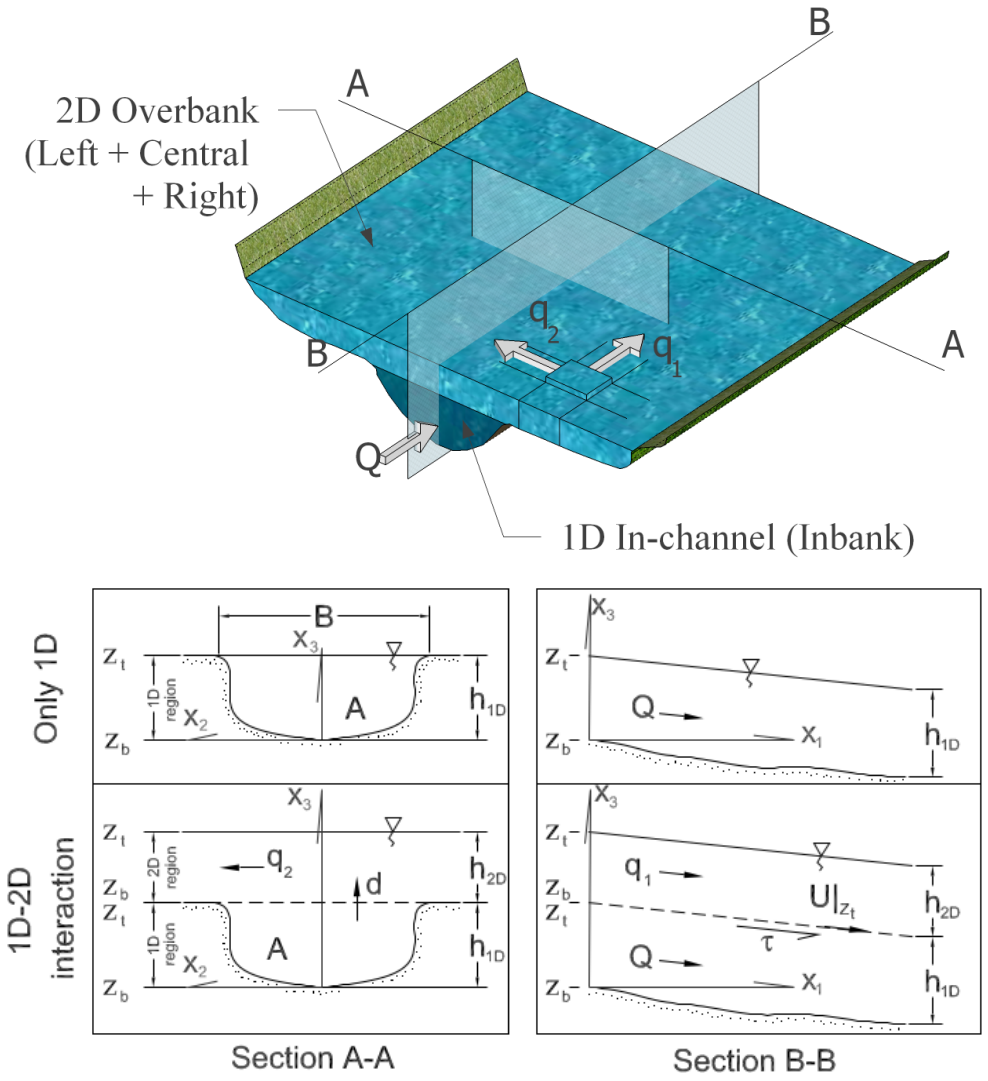


Figure 35: Vertical coupling method. Top figure: three-dimensional view of the coupling of 1D (inbank) and 2D (overbank) flows. Bottom figures: A-A: transversal cross section, B-B: longitudinal profile along the main channel. Notice that the flow above the in-channel region is considered as the overbank (left+central+right) region.

# BIBLIOGRAPHY


Aalto, R., Maurice-Bourgoin, L., Dunne, T., Montgomery, D. R., Nittrouer, C. A., & Guyot, J.-L. (2003, oct). Episodic sediment accumulation on Amazonian flood plains influenced by El Niño/Southern Oscillation. *Nature*, *425*(6957), 493–7. Retrieved from http://dx.doi.org/10.1038/nature02002 doi: 10.1038/nature02002

Abad, J. D., Buscaglia, G., & Garcia, M. H. (2008). 2D Stream Hydrodynamic, sediment transport and bed morphology model for engineering applications. *Hydrological Processes*, *22*, 1443–1459.

Abad, J. D., & Garcia, M. H. (2006). RVR Meander: A toolbox for re-meandering of channelized streams. *Computers and Geosciences*, *32*, 92–101. doi: 10.1016/j.cageo.2005.05.006

Abad, J. D., & Montoro, H. (2013). Anabranching structures in the Upper Amazon River, quasi-freely and non-developed meanders. *In submission*.

Abad, J. D., Paredes, J., & Montoro, H. (2010). Similarities and differences between a large meandering river and an anabranching river: the Ucayali and Amazon River cases. In *Agu fall meeting*. San Francisco, USA.

Abad, J. D., Vizcarra, J., Paredes, J., Montoro, H., Frias, C., & Holguin, C. (2013). *Morphodynamics of the upper peruvian amazonian rivers, implications into fluvial transportation.* EUT Edizioni Università di Trieste. Retrieved from http://www.openstarts.units.it/dspace/handle/10077/8822

Adeney, J. M. (2009). *Remote sensing of fire, flooding, and white sand ecosystems in the Amazon* (Doctoral dissertation, Ann Arbor). Retrieved from

http://pitt.idm.oclc.org/login?url=http://search.proquest.com/docview/304879969?accountid=14709http://rt4rf9qn2y.search.serialssolutions.com/?ctx{_}ver=Z39.88-2004{&}ctx{_}enc=info:ofi/enc:UTF-8{&}rfr{_}id=info:sid/ProQuest+Dissertations+{&}+Theses+Full+Text{&}rft{_}val

Allitt, R. (2009). Coupled 1D - 2D Modelling in Urban Areas. *WaPUG USER NOTE*(40), 1–20.

Alsdorf, D., Han, S.-C., Bates, P., & Melack, J. (2010, nov). Seasonal water storage on the Amazon floodplain measured from satellites. *Remote Sensing of Environment*, *114*(11), 2448–2456. Retrieved from http://www.sciencedirect.com/science/article/pii/S0034425710001768 doi: 10.1016/j.rse.2010.05.020

Altinakar, M. S., Miglio, E., & Wu, W. (2008). Coupling 1D-2D Shallow Water models for Simulating Floods due to Overtopping and Breaching of Leeves. In *8th.world congress on computational mechanics* (pp. 1–2).

Bates, P., & De Roo, A. (2000, sep). A simple raster-based model for flood inundation simulation. *Journal of Hydrology*, *236*(1-2), 54–77. Retrieved from http://www.sciencedirect.com/science/article/pii/S002216940000278X doi: 10.1016/S0022-1694(00)00278-X

Benito, G., Díez-Herrero, A., & Fernández De Villalta, M. (2003). Magnitude and frequency of flooding in the Tagus basin (Central Spain) over the last millennium. *Climatic Change*, *58*(1-2), 171–192. doi: 10.1023/A:1023417102053

Bernini, A., & Franchini, M. (2013, jun). A Rapid Model for Delimiting Flooded Areas. *Water Resources Management*, *27*(10), 3825–3846. Retrieved from http://link.springer.com/10.1007/s11269-013-0383-3 doi: 10.1007/s11269-013-0383-3

Birkett, C. M. (2002). Surface water dynamics in the Amazon Basin: Application of satellite radar altimetry. *Journal of Geophysical Research*, *107*(D20), 8059. Retrieved from http://doi.wiley.com/10.1029/2001JD000609 doi: 10.1029/2001JD000609

Bladé, E., Gómez-Valentín, M., Dolz, J., Aragón-Hernández, J., Corestein, G., & Sánchez-Juny, M. (2012, jun). Integration of 1D and 2D finite volume schemes for computations of

water flow in natural channels. *Advances in Water Resources*, *42*, 17–29. Retrieved from http://www.sciencedirect.com/science/article/pii/S0309170812000760 doi: 10.1016/j.advwatres.2012.03.021

Bousmar, D., & Zech, Y. (1999). Momentum Transfer for Practical Flow Computation in Compound Channels. *Journal of Hydraulic Engineering*, *125*(July), 696–706. doi: 10.1061/(ASCE)0733-9429(1999)125:7(696)

Brunner, G. W. (2010). *River Analysis System User's Manual, Version 4.1* (Tech. Rep. No. January). Davis: US Army Corps of Engineers, Institute for Water Resources, Hydrologic Engineering Center (HEC). doi: CPD-68

Brunner, G. W. (2014, oct). *Combined 1D and 2D modeling with HEC-RAS* (Tech. Rep.). Hydraulic Engineering Corps.

Brunner, G. W. (2016a). *HEC-RAS 5.0 2D Modeling Users Manual* (Tech. Rep.). Davis, CA: US Army Corps of Engineers, Institute for Water Resources, Hydrologic Engineering Center.

Brunner, G. W. (2016b). *HEC-RAS 5.0 Users Manual* (Tech. Rep.). Davis, CA: US Army Corps of Engineers, Institute for Water Resources, Hydrologic Engineering Center.

Chatterjee, C., Förster, S., & Bronstert, A. (2008, nov). Comparison of hydrodynamic models of different complexities to model floods with emergency storage areas. *Hydrological Processes*, *22*(24), 4695–4709. Retrieved from http://doi.wiley.com/10.1002/hyp.7079 doi: 10.1002/hyp.7079

Chen, J. L., Wilson, C. R., & Tapley, B. D. (2010, dec). The 2009 exceptional Amazon flood and interannual terrestrial water storage change observed by GRACE. *Water Resources Research*, *46*(12), n/a–n/a. Retrieved from http://doi.wiley.com/10.1029/2010WR009383 doi: 10.1029/2010WR009383

Chen, Y., Wang, Z., Liu, Z., & Zhu, D. (2012). 1D-2D Coupled Numerical Model for Shallow-Water Flows. *Journal of Hydraulic Engineering, ASCE*, *138*, 122–132.

Chow, V. T. (1959). *Open-Channel Hydraulics* (Internatio ed.). McGraw-Hill Book Company, Inc.

Coe, M. T., Costa, M. H., Botta, A., & Birkett, C. (2002). Long-term simulations of discharge and floods in the Amazon Basin. *Journal of Geophysical Research*, *107*(D20), 8044. Retrieved from http://doi.wiley.com/10.1029/2001JD000740 doi: 10.1029/2001JD000740

Coe, M. T., Costa, M. H., & Howard, E. A. (2008, jul). Simulating the surface waters of the Amazon River basin: impacts of new river geomorphic and flow parameterizations. *Hydrological Processes*, *22*(14), 2542–2553. Retrieved from http://doi.wiley.com/10.1002/hyp.6850 doi: 10.1002/hyp.6850

Colinvaux, P. A., Miller, M. C., Liu, K.-B., & Steinitz-Kannan, M. (1985). Discovery of permanent Amazon lakes and hydraulic disturbance in the upper Amazon basin. *Nature (London)*, *313*(5997), 42–45.

Connell, R., Painter, D., & Beffa, C. (2001, oct). Two-Dimensional Flood Plain Flow. II: Model Validation. *Journal of Hydrologic Engineering*, *6*(5), 406–415. Retrieved from http://dx.doi.org/10.1061/(ASCE)1084-0699(2001)6:5(406) doi: 10.1061/(ASCE)1084-0699(2001)6:5(406)

Cook, A., & Merwade, V. (2009, oct). Effect of topographic data, geometric configuration and modeling approach on flood inundation mapping. *Journal of Hydrology*, *377*(1-2), 131–142. Retrieved from http://linkinghub.elsevier.com/retrieve/pii/S0022169409004909 doi: 10.1016/j.jhydrol.2009.08.015

Cook, A. C. (2008). Comparison of one-dimensional HEC-RAS with two-dimensional FESWNS model in flood inundation mapping. (May), 1–99.

Coordinadora Nacional de Derechos Humanos. (2012). *Iquitos en situación crítica tras inundaciones.* Retrieved from http://derechoshumanos.pe/2012/05/iquitos-en-situacion-critica-tras-inundaciones/

Costabile, P., & Macchione, F. (2011, dec). Analysis of One-Dimensional Modelling for Flood Routing in Compound Channels. *Water Resources Management*, *26*(5), 1065–1087. Retrieved from http://link.springer.com/10.1007/s11269-011-9947-2 doi: 10.1007/s11269-011-9947-2

D'Alpaos, L., & Defina, A. (1993). Venice lagoon hydrodynamics simulation by coupling 2D and 1D finite element models. In *8th conference on finite elements in fluids. new trends and applications* (pp. 917—-926).

D'Alpaos, L., & Defina, A. (2007, may). Mathematical modeling of tidal hydrodynamics in shallow lagoons: A review of open issues and applications to the Venice lagoon. *Computers & Geosciences*, *33*(4), 476–496. Retrieved from http://www.sciencedirect.com/science/article/pii/S0098300406001476 doi: 10.1016/j.cageo.2006.07.009

Deltares. (2016). *SOBEK, User Manual* (Tech. Rep.). Delft: Author. Retrieved from https://content.oss.deltares.nl/delft3d/manuals/SOBEK_User_Manual.pdf

Desombre, J. (2013, oct). *TELEMAC-2D software: Operating Manual* (6.0 ed.).

DHI. (2007a). *Mike 11: A modeling system for Rivers and Channels User Guide* (Tech. Rep.).

DHI. (2007b). *MIKE FLOOD - 1D-2D Modelling - User Manual* (Tech. Rep.).

Di Baldassarre, G., Castellarin, A., & Brath, A. (2009, dec). Analysis of the effects of levee heightening on flood propagation: example of the River Po, Italy. *Hydrological Sciences Journal*, *54*(6), 1007–1017. Retrieved from http://www.tandfonline.com/doi/abs/10.1623/hysj.54.6.1007 doi: 10.1623/hysj.54.6.1007

Di Baldassarre, G., Schumann, G., Bates, P. D., Freer, J. E., & Beven, K. J. (2010, apr). Flood-plain mapping: a critical discussion of deterministic and probabilistic approaches. *Hydrological Sciences Journal*, *55*(3), 364–376. Retrieved from http://www.tandfonline.com/doi/abs/10.1080/02626661003683389 doi: 10.1080/02626661003683389

Dilley, M., Chen, R. S., & Deichmann, U. (2005). *Natural Disaster Hotspots : A Global Risk Analysis*. Washington, DC, USA: World Bank Publications. Retrieved from http://site.ebrary.com/lib/pitt/docDetail.action?docID=10078123

Dyhouse, G., Hatchett, J., Benn, J., & Haestad Methods Inc. (2003). *Floodplain modeling using HEC-RAS* (1st ed. ed.). Waterbury, CT : Haestad Press, c2003.

Ervine, D. A., Babaeyan-Koopaei, K., & Sellin, R. H. J. (2000, sep). Two-Dimensional Solution for Straight and Meandering Overbank Flows. *Journal of Hydraulic Engineering*, *126*(9), 653–669. Retrieved from http://ascelibrary.org/doi/abs/10.1061/(ASCE)0733-9429(2000)126:9(653) doi: 10.1061/(ASCE)0733-9429(2000)126:9(653)

Espinoza, J. C., Ronchail, J., Frappart, F., Lavado, W., Santini, W., & Guyot, J. L. (2013, jun). The Major Floods in the Amazonas River and Tributaries (Western Amazon Basin) during the 1970 - 2012 Period: A Focus on the 2012 Flood. *Journal of Hydrometeorology*, *14*(3), 1000–1008. Retrieved from http://journals.ametsoc.org/doi/abs/10.1175/JHM-D-12-0100.1 doi: 10.1175/JHM-D-12-0100.1

Espinoza Villar, J. C., Ronchail, J., Guyot, J. L., Cochonneau, G., Naziano, F., Lavado, W., ... Vauchel, P. (2009, sep). Spatio-temporal rainfall variability in the Amazon basin countries (Brazil, Peru, Bolivia, Colombia, and Ecuador). *International Journal of Climatology*, *29*(11), 1574–1594. Retrieved from http://doi.wiley.com/10.1002/joc.1791 doi: 10.1002/joc.1791

Fernández-Nieto, E., Marin, J., & Monnier, J. (2010, jun). Coupling superposed 1D and 2D shallow-water models: Source terms in finite volume schemes. *Computers & Fluids*, *39*(6), 1070–1082. Retrieved from http://linkinghub.elsevier.com/retrieve/pii/S0045793010000289 doi: 10.1016/j.compfluid.2010.01.016

FLOW Science. (2008). *FLOW-3D user manual* (Tech. Rep.). Santa Fe, New Mexico: FLOW Science, Inc. Retrieved from www.flow3d.com

Francesco, S. D., Biscarini, C., & Montesarchio, V. (2014). An evaluation of Computational Fluid dynamics model for flood risk analysis. *Geophysical Research Abstracts EGU General Assembly*, *16*, 11671. Retrieved from http://meetingorganizer.copernicus.org/EGU2014/EGU2014-11671.pdf

Frias, C. E., Abad, J. D., Mendoza, A., Paredes, J., Ortals, C. J., & Montoro, H. (2015). Planform evolution of two anabranching structures in the Upper Peruvian Amazon River. *Water Resources Research*, *51*, 1–18. doi: 10.1002/2014WR016259

Gaurav, K., Sinha, R., & Panda, P. K. (2011). The Indus flood of 2010 in Pakistan: a perspective analysis using remote sensing data. *Natural Hazards*, *59*(3), 1815–1826. Retrieved from http://dx.doi.org/10.1007/s11069-011-9869-6 doi: 10.1007/s11069-011-9869-6

Gejadze, I., & Monnier, J. (2007). On a 2D 'zoom'for the 1D shallow water model: Coupling and data assimilation. *Computer methods in applied mechanics and . . .*, *196*(March), 4628–4643. Retrieved from http://www.sciencedirect.com/science/article/pii/S0045782507002319

Gentry, A. H., & Lopez-Parodi, J. (1980, dec). Deforestation and Increased Flooding of the Upper Amazon. *Science*, *210*(4476), 1354–1356. Retrieved from http://www.jstor.org/stable/1686107 doi: 10.2307/1686107

Gharbi, M., Soualmia, A., Dartus, D., & Masbernat, L. (2016). Comparison of 1D and 2D Hydraulic Models for Floods Simulation on the Medjerda Riverin Tunisia. *Journal of Materials and Environmental Science*, *7*(8), 3017–3026.

Ghostine, R., Hoteit, I., Vazquez, J., Terfous, A., Ghenaim, A., & Mose, R. (2014, dec). Comparison between a coupled 1D-2D model and a fully 2D model for supercritical flow simulation in crossroads. *Journal of Hydraulic Research*, 1–8. Retrieved from http://dx.doi.org/10.1080/00221686.2014.974081 doi: 10.1080/00221686.2014.974081

Giampieri, R., Tassi, P., Rodríguez, L., Gaudin, H., & Vionnet, C. (2003). SIMULACIÓN NUMÉRICA DEL DESBORDE DEL RÍO SALADO SOBRE LA CIUDAD DE SANTA FE , ABRIL 2003. In *Primer simposio regional sobre hidraulica de rios* (pp. 1–2).

Gloor, M., Brienen, R. J. W., Galbraith, D., Feldpausch, T. R., Schöngart, J., Guyot, J.-L., ... Phillips, O. L. (2013, may). Intensification of the Amazon hydrological cycle over the last two decades. *Geophysical Research Letters*, *40*(9), 1729–1733. Retrieved from http://doi.wiley.com/10.1002/grl.50377 doi: 10.1002/grl.50377

Gordienko, E. C. (2010). *The Amazon Basin* (Tech. Rep.). Retrieved from https://geogshare.files.wordpress.com/2017/10/resource-l4-amazon-article-2010.pdf

Hall, A. C., Schumann, G. J.-P., Bamber, J. L., & Bates, P. D. (2011, jan). Tracking water level changes of the Amazon Basin with space-borne remote sensing and integration with large scale hydrodynamic modelling: A review. *Physics and Chemistry of the Earth, Parts A/B/C*, *36*(7-8), 223–231. Retrieved from http://www.sciencedirect.com/science/article/pii/S1474706510002172 doi: 10.1016/j.pce.2010.12.010

Hick, F. E., & T., P. (2005, jan). Suitability of HEC-RAS for flood forecasting. *Canadian Water Resources Journal*, *30*, 159+. Retrieved from https://www.tandfonline.com/doi/abs/10.4296/cwrj3002159

Hicks, F. E., & Peacock, T. (2005, jan). Suitability of HEC-RAS for Flood Forecasting. *Canadian Water Resources Journal*, *30*(December), 159–174. Retrieved from http://www.tandfonline.com/doi/abs/10.4296/cwrj3002159 doi: 10.4296/cwrj3002159

Hofer, T., & Messerli, B. (2006). Preface. In *Floods in bangladesh : History, dynamics and rethinking the role of the himalayas* (pp. xix ——— xxix). Tokyo, JPN: United Nations University Press. Retrieved from http://site.ebrary.com/lib/pitt/docDetail.action?docID=10156081

Horritt, M. S., & Bates, P. D. (2002). Evaluation of 1D and 2D numerical models for predicting river flood inundation. *Journal of Hydrology*, *268*, 23–34.

Horritt, M. S., Di Baldassarre, G., Bates, P. D., & Brath, A. (2007). Comparing the performance of a 2-D finite element and a 2-D finite volume model of floodplain inundation using airborne SAR imagery. *Hydrological Processes*, *21*(20), 2745–2759. Retrieved from http://dx.doi.org/10.1002/hyp.6486 doi: 10.1002/hyp.6486

INGEMMET. (2014). *GEOCATMIN sistema de informacion geologico y catastral minero.* Retrieved 2014-01-01, from http://geocatmin.ingemmet.gob.pe/geocatmin/

Jarvus. (2016). *Connecting 1D river with 2D flow area using a lateral structure.* Retrieved 2016-11-14, from http://hecrasmodel.blogspot.com/p/hec-ras-bloggery-forum.html

Jha, A., Bloch, R., & Lamond, J. (2012). *Cities and flooding: a guide to integrated urban flood risk management for the 21st century*. Retrieved from https://openknowledge.worldbank.org/handle/10986/2241

Joy Lim, N., Anders Brandt Examinator, S., Östman Co-examinator, A., & Jiang, B. (2011). *Performance and uncertainty estimation of 1-and 2-dimensional flood models* (Master Thesis, Akademin For Teknik Och Miiljo). Retrieved from http://www.diva-portal.org/smash/get/diva2:426406/FULLTEXT01.pdf

Jung, H. C., Alsdorf, D., Moritz, M., Lee, H., & Vassolo, S. (2011, jan). Analysis of the relationship between flooding area and water height in the Logone floodplain. *Physics and Chemistry of the Earth, Parts A/B/C*, *36*(7-8), 232–240. Retrieved from http://linkinghub.elsevier.com/retrieve/pii/S1474706511000209 doi: 10.1016/j.pce.2011.01.010

Khan, S. I., Hong, Y., Gourley, J. J., Khattak, M. U., & De Groeve, T. (2014). Multi-Sensor Imaging and Space-Ground Cross-Validation for 2010 Flood along Indus River, Pakistan. *Remote Sensing*, *6*(3), 2393. Retrieved from http://www.mdpi.com/2072-4292/6/3/2393 doi: 10.3390/rs6032393

Knight, D. W., & Demetriou, J. D. (1983). Flood plain and main channel flow interaction. *Journal of Hydraulic Engineering*, *109*(8), 1073–1092.

Knight, D. W., & Sellin, R. H. J. (1987, oct). The SERC Flood Channel Facility. *Water and Environment Journal*, *1*(2), 198–204. Retrieved from http://dx.doi.org/10.1111/j.1747-6593.1987.tb01212.x doi: 10.1111/j.1747-6593.1987.tb01212.x

Knight, D. W., & Shiono, K. (1990, mar). Turbulence measurements in a shear layer region of a compound channel. *Journal of Hydraulic Research*, *28*(2), 175–196. Retrieved from http://dx.doi.org/10.1080/00221689009499085 doi: 10.1080/00221689009499085

Kuiry, S. N., Sen, D., & Bates, P. D. (2010, aug). Coupled 1DâĂŞQuasi-2D Flood Inundation Model with Unstructured Grids. *Journal of Hydraulic Engineering*, *136*(8), 493–506. Retrieved from http://ascelibrary.org/doi/abs/10.1061/(ASCE)HY.1943-7900.0000211 doi: 10.1061/(ASCE)HY.1943-7900.0000211

Kundu, P. K. (2010). *Fluid Mechanics* (4th ed.). 30 Corporate Drive, Suite 400, Burlington, MA 01803, USA: Elsevier.

Kwak, Y., Park, J., & Fukami, K. (2014). Near Real-Time Flood Volume Estimation From MODIS Time-Series Imagery in the Indus River Basin. *Selected Topics in Applied Earth Observations and Remote Sensing, IEEE Journal of*, *7*(2), 578–586. doi: 10.1109/JSTARS.2013.2284607

Langendoen, E. J. (2000). *CONCEPTS âĂŞ Conservational Channel Evolution and Pollutant Transport System* (No. 16). P.O. Box 1157, Oxford, MS 38655.

Langendoen, E. J., & Alonso, C. V. (2008). Modeling the evolution of incised streams. I: model formulation and validation of flow and streambed evolution components. *Journal of Hydraulic Engineering*, *134*(6), 749–762.

Langendoen, E. J., & Simon, A. (2008). Modeling the evolution of incised streams. II: streambank erosion. *Journal of Hydraulic Engineering*, *134*(7), 905–915.

Langendoen, E. J., Wells, R. R., Thomas, R. E., Simon, A., & Bingner, R. L. (2009). Modeling the evolution of incised streams. III: model application. *Journal of Hydraulic Engineering*, *135*(6), 476–486.

Li, W., Chen, Q., & Mao, J. (2009, may). Development of 1D and 2D coupled model to simulate urban inundation: An application to Beijing Olympic Village. *Chinese Science Bulletin*, *54*(9), 1613–1621. Retrieved from http://link.springer.com/10.1007/s11434-009-0208-1 doi: 10.1007/s11434-009-0208-1

Liebmann, B., & Marengo, J. A. (2001). Interannual variability of the rainy season and rainfall in the Brazilian Amazon Basin. *Journal of Climate*, *14*(22), 4308–4318. doi: 10.1175/1520-0442(2001)014<4308:IVOTRS>2.0.CO;2

Liggett, J. A. (1994). *Fluid Mechanics*. McGraw-Hill, New York, NY.

Lindenschmidt, K.-E. (2008, apr). Quasi-2D Approach in Modeling the Transport of Contaminated Sediments in Floodplains during River FloodingâĂŤModel Coupling and Uncertainty Analysis. *Environmental Engineering Science*, *25*(3), 333–352. Retrieved from http://www.liebertonline.com/doi/abs/10.1089/ees.2006.0192 doi: 10.1089/ees.2006.0192

Liu, H.-L., Chen, X., Bao, A.-M., & Wang, L. (2007, dec). Investigation of groundwater response to overland flow and topography using a coupled MIKE SHE/MIKE 11 modeling system for an arid watershed. *Journal of Hydrology*, *347*(3-4), 448–459. Retrieved from http://linkinghub.elsevier.com/retrieve/pii/S0022169407005343 doi: 10.1016/j.jhydrol.2007.09.053

Liu, R., & Liu, N. (2002). Flood area and damage estimation in Zhejiang, China. *Journal of environmental management*, *66*(1), 1–8. doi: 10.1006/jema.2002.0544

Lopes, P. (n.d.). Free-surface flow interface and air-entrainment modelling using OpenFOAM. , 71. Retrieved from https://pdfs.semanticscholar.org/5945/596db8a377a68fc5bc37884dac390f7c451a.pdf

Maatar, F. E., Domeneghetti, A., & Brath, A. (2015). HEC-RAS 5 . 0 Vs . TELEMAC-2D : a model comparison for flood-hazard and flood-risk estimation. *EGU General Assembly, held 12-17 April, 2015 in Vienna, Austria. id.910*, *17*, 2015.

Marengo, J. A., Tomasella, J., Soares, W. R., Alves, L. M., & Nobre, C. A. (2012, jul). Extreme climatic events in the Amazon basin: climatological and hydrological context of recent floods. *Theoretical and Applied Climatology*, *107*, 73+. Retrieved from https://link.springer.com/article/10.1007/s00704-011-0465-1

Martinez, J., & Le Toan, T. (2007, jun). Mapping of flood dynamics and spatial distribution of vegetation in the Amazon floodplain using multitemporal SAR data. *Remote Sensing of Environment*, *108*(3), 209–223. Retrieved from http://www.sciencedirect.com/science/article/pii/S0034425706004585 doi: 10.1016/j.rse.2006.11.012

Mendoza, A., Abad, J. D., Frias, C. E., Ortals, C., Paredes, J., Montoro, H., ... Soto-Cortés, G. (2016). Planform dynamics of the Iquitos anabranching structure in the Peruvian upper Amazon river. *Earth Surface Processes and Landforms*, n/a–n/a. Retrieved from http://dx.doi.org/10.1002/esp.3911 doi: 10.1002/esp.3911

Mendoza, A., Frias, C. E., Abad, J. D., Paredes, J., Dauer, K. R., Vizcarra, J., & Montoro, H. (2014). Analysis of the evolution of the Iquitos anabranching structure in the Upper Amazon River, Peru. *In review*.

Morales-Hernández, M., García-Navarro, P., Burguete, J., & Brufau, P. (2013, jul). A conservative strategy to couple 1D and 2D models for shallow water flow simulation. *Computers & Fluids*, *81*, 26–44. Retrieved from http://www.sciencedirect.com/science/article/pii/S0045793013001217 doi: 10.1016/j.compfluid.2013.04.001

Moussa, R., & Bocquillon, C. (2009). On the use of the diffusive wave for modelling extreme flood events with overbank flow in the floodplain. *Journal of Hydrology*, *374*(1-2), 116–135. Retrieved from http://dx.doi.org/10.1016/j.jhydrol.2009.06.006 doi: 10.1016/j.jhydrol.2009.06.006

Moya Quiroga, V., Kure, S., Udo, K., & Mano, A. (2016). Application of 2D numerical simulation for the analysis of the February 2014 Bolivian Amazonia flood: Application of the new HEC-RAS version 5. *RIBAGUA - Revista Iberoamericana del Agua*, *3*(February 2014), 1–9. Re-

trieved from http://linkinghub.elsevier.com/retrieve/pii/S2386378116000025 doi: 10.1016/j.riba.2015.12.001

Mustafa, D., & Wrathall, D. (2011, feb). Indus basin floods of 2010: Souring of a Faustian bargain? *Water alternatives*, *4*(1), 72–85.

Myers, W. R. C., & Brennan, E. K. (1990, mar). Flow resistance in compound channels. *Journal of Hydraulic Research*, *28*(2), 141–155. Retrieved from http://dx.doi.org/10.1080/00221689009499083 doi: 10.1080/00221689009499083

Myster, R. W. (2007, jan). Interactive Effects of Flooding and Forest Gap Formation on Tree Composition and Abundance in the Peruvian Amazon. *Folia Geobotanica*, *42*(1), 1–9. Retrieved from http://www.jstor.org/stable/41245483 doi: 10.2307/41245483

O'Brien, J. S., Julien, P. Y., & Fullerton, W. T. (1993, feb). Two Dimensional Water Flood and Mudflow Simulation. *Journal of Hydraulic Engineering*, *119*(2), 244–261. Retrieved from http://ascelibrary.org/doi/abs/10.1061/(ASCE)0733-9429(1993)119:2(244) doi: 10.1061/(ASCE)0733-9429(1993)119:2(244)

O'Connor, J. E., & Costa, J. E. (2008). *The World's Largest Floods, Past and Present - Their Causes and Magnitudes: U.S. Geological Survey Circular 1254* (Tech. Rep.). Box 25286, Denver Federal Center, Denver, CO 80225: U.S. Geological Survey. Retrieved from http://pubs.usgs.gov/circ/2004/circ1254/pdf/circ1254.pdf

Pistocchi, A., & Mazzoli, P. a. (2002). Use of HEC-RAS and HEC-HMS models with ArcView for hydrologic risk management. In *Proceesing iemss 2002* (pp. 305–310). Retrieved from https://scholarsarchive.byu.edu/cgi/viewcontent.cgi?article=3753&context=iemssconference

Post, D., a.E. Kinsey-Henderson, Stewart, L., Roth, C., & Reghenzani, J. (2003, oct). Optimising drainage from sugar cane fields using a one-dimensional flow routing model: a case study from Ripple Creek, North Queensland. *Environmental Modelling & Software*,

*18*(8-9), 713–720. Retrieved from http://linkinghub.elsevier.com/retrieve/pii/S1364815203000732 doi: 10.1016/S1364-8152(03)00073-2

Prinos, P., & Townsend, R. D. (1984, dec). Comparison of methods for predicting discharge in compound open channels. *Advances in Water Resources*, *7*(4), 180–187. Retrieved from http://linkinghub.elsevier.com/retrieve/pii/0309170884900162 doi: 10.1016/0309-1708(84)90016-2

Proust, S., Bousmar, D., Riviere, N., Paquier, A., & Zech, Y. (2009, dec). Nonuniform flow in compound channel: A 1-D method for assessing water level and discharge distribution. *Water Resources Research*, *45*(12), n/a–n/a. Retrieved from http://doi.wiley.com/10.1029/2009WR008202 doi: 10.1029/2009WR008202

Qi, H., & Altinakar, M. S. (2011). A GIS-based decision support system for integrated flood management under uncertainty with two dimensional numerical simulations. *Environmental Modelling and Software*, *26*(6), 817–821. doi: 10.1016/j.envsoft.2010.11.006

Richey, J. E., Mertes, L. A. K., Dunne, T., Victoria, R. L., Forsberg, B. R., Tancredi, A. C. N. S., & Oliveira, E. (1989). Sources and routing of the Amazon River Flood Wave. *Global Biogeochemical Cycles*, *3*(3), 191–204. Retrieved from http://dx.doi.org/10.1029/GB003i003p00191 doi: 10.1029/GB003i003p00191

Richey, J. E., Nobre, C., & Deser, C. (1989, oct). Amazon river discharge and climate variability: 1903 to 1985. *Science (New York, N.Y.)*, *246*(4926), 101–103. Retrieved from http://www.jstor.org/stable/1703919 doi: 10.1126/science.246.4926.101

Robb, D. M., & Vasquez, J. A. (2015). NUMERICAL SIMULATION OF DAM - BREAK FLOWS USING DEPTH - AVERAGED HYDRODYNAMIC AND THREE - DIMENSIONAL CFD MODELS. In *22nd canadian hydrotechnical conference*. Montreal. Retrieved from https://www.researchgate.net/publication/304075977_Numerical_simulation_of_dam-break_flows_using_depth-averaged_hydrodynamic_and_three-dimensional_CFD_models

Sanyal, J., Carbonneau, P., & Densmore, A. L. (2014, dec). Low-cost flood inundation modelling at reach scale with sparse data in the lower Damodar river basin, India. *Hydrological Sciences Journal*, *6667*(June), 140120033456007. Retrieved from http://www.tandfonline.com/doi/abs/10.1080/02626667.2014.884718 doi: 10.1080/02626667.2014.884718

Servicio de Hidrografía y Navegación de la Amazonía. (2011). *LEVANTAMIENTO HIDROGRÁFICO Y CARTA DE PRACTICAJE DEL RÍO AMAZONAS DESDE LA CONFLUENCIA DE LOS RÍOS MARAÑÓN Y UCAYALI HASTA LA DESEMBOCADURA DEL RÍO YAVARÍ* (Tech. Rep.). Iquitos: Marina de Guerra del Peru.

Shiono, K., & Knight, D. W. (1991, jan). Turbulent open-channel flows with variable depth across the channel. *Journal of Fluid Mechanics*, *222*, 617—-646. doi: 10.1017/S0022112091001246

Shiono, K., & Muto, Y. (1998, dec). Complex flow mechanisms in compound meandering channels with overbank flow. *Journal of Fluid Mechanics*, *376*, 221–261. doi: 10.1017/S0022112098002869

Simon, C. A., Langendoen, E. J., Abad, J. D., & Mendoza, A. (2016). On the Governing Equations for Horizontal and Vertical Coupling of One- and Two-dimensional Open Channel Flow Models. *Journal of Hydraulic Research*(In Review).

Simon, C. A., Langendoen, E. J., Mendoza, A., & Abad, J. D. (2016). *Numerical Comparison for Horizontal and Vertical Coupling of One- and Two-dimensional Open Channel Flows.* Pittsburgh.

Sternberg, H. O. (1987, jan). Aggravation of Floods in the Amazon River as a Consequence of Deforestation? *Geografiska Annaler. Series A, Physical Geography*, *69*(1), 201–219. Retrieved from http://www.jstor.org/stable/521378 doi: 10.2307/521378

Supharatid, S. (2006, feb). The Hat Yai 2000 flood: the worst flood in Thai history. *Hydrological Processes*, *20*(2), 307–318. Retrieved from http://doi.wiley.com/10.1002/hyp.5912 doi: 10.1002/hyp.5912

Suriya, S., & Mudgal, B. V. (2012). Impact of urbanization on flooding: The Thirusoolam sub watershed - A case study. *Journal of Hydrology*, *412-413*, 210–219. doi: 10.1016/j.jhydrol.2011.05.008

Syme, W., Pinnell, M., & Wicks, J. (2004). Modelling Flood Inundation of Urban Areas in the UK Using 2D/1D Hydraulic Models. *8th Natinal Conference on Hydraulics in Water Engineering*(July), 8. Retrieved from https://www.tuflow.com/Download/Publications/Modelling%20Flood%20Inundation%20of%20Urban%20Areas%20in%20the%20UK,%20Syme,%202004.pdf

Teles, M. J., Smolders, S., Maximova, T., Rocabado, I., & Vanlede, J. (2015). Numerical modelling of flood control areas with controlled reduced tide. *E-proceedings of the 36th IAHR World Congress*(1), 10.

The Columbia Encyclopedia. (2013). *Iquitos.* Columbia University Press. Retrieved from http://search.credoreference.com/content/entry/columency/iquitos/0

The Hutchinson Encyclopedia with atlas and weather guide. (2014). *Iquitos.* Helicon. Retrieved from http://search.credoreference.com/content/entry/heliconhe/iquitos/0

Timbadiya, P. V. (2011). Calibration of HEC-RAS Model on Prediction of Flood for Lower Tapi River, India. *Journal of Water Resource and Protection*, *03*(11), 805–811. Retrieved from http://www.scirp.org/journal/PaperDownload.aspx?DOI=10.4236/jwarp.2011.311090 doi: 10.4236/jwarp.2011.311090

Trigg, M. a., Wilson, M. D., Bates, P. D., Horritt, M. S., Alsdorf, D. E., Forsberg, B. R., & Vega, M. C. (2009, jul). Amazon flood wave hydraulics. *Journal of Hydrology*, *374*(1-2), 92–105. Retrieved from http://linkinghub.elsevier.com/retrieve/pii/S0022169409003278 doi: 10.1016/j.jhydrol.2009.06.004

USGS. (2015). *EarthExplorer.* Retrieved from http://earthexplorer.usgs.gov/

Valenzuela-Yasalde, M. (2017). *PERÚ: ESTIMACIONES Y PROYECCIONES DE POBLACIÓN TOTAL POR SEXO DE LAS PRINCIPALES CIUDADES, 2012-2015* (Tech. Rep.). Instituto Nacional de Estadistica e Informatica.

van Prooijen, B. C., Battjes, J. A., & Uijttewaal, W. S. J. (2005, mar). Momentum Exchange in Straight Uniform Compound Channel Flow. *Journal of Hydraulic Engineering*. Retrieved from https://ascelibrary.org/doi/abs/10.1061/(ASCE)0733-9429(2005)131:3(175)

Viala, Y., Leroy, H., Brignolles, C., & Sau, J. (2005). Modelling of the Floods of the River Siagne. , 1–13. Retrieved from https://mafiadoc.com/modelling-of-the-floods-of-the-river-siagne-_5aa41cb31723dd34360f2f88.html

Vozinaki, A.-E. K., Morianou, G. G., Alexakis, D. D., & Tsanis, I. K. (2016, nov). Comparing 1D- and combined 1D/2D hydraulic simulations using high resolution topographic data, the case study of the Koiliaris basin, Greece. *Hydrological Sciences Journal*, 02626667.2016.1255746. Retrieved from https://www.tandfonline.com/doi/full/10.1080/02626667.2016.1255746 doi: 10.1080/02626667.2016.1255746

Vu, T. T., Nguyen, P. K. T., Chua, L. H. C., & Law, A. W. K. (2015). Two-Dimensional Hydrodynamic Modelling of Flood Inundation for a Part of the Mekong River with TELEMAC-2D. *British Journal of Environment & Climate ChangeBJECC*, *5013*(2), 162–175. Retrieved from http://www.sciencedomain.org/index.php?/abstract/9609 doi: 10.9734/BJECC/2015/12885

Wang, Y., & Zhou, W. (2015). Design and Application of Small Scale Cluster System Based on OpenFOAM. *International Journal of Hybrid Information Technology*, *8*(2), 121–134. doi: 10.14257/ijhit.2015.8.2.11

Wilson, C. A. M. E., Stoesser, T., Olsen, N. R. B., & Bates, P. D. (2003). Application and validation of numerical codes in the prediction of compound channel flows. *Proceedings of the Institution of Civil Engineers: Water and Maritime Engineering*, *156*(2), 117–128.

Wilson, M., Bates, P., Alsdorf, D., Forsberg, B., Horritt, M., Melack, J., ... Famiglietti, J. (2007). Modeling large-scale inundation of Amazonian seasonally flooded wetlands. *Geophysical Research Letters*, *34*(15), L15404. Retrieved from http://dx.doi.org/10.1029/2007GL030156 doi: 10.1029/2007GL030156

Wohl, E. (2013, aug). Floodplains and wood. *Earth-Science Reviews*, *123*, 194–212. Retrieved from http://www.sciencedirect.com/science/article/pii/S0012825213000834 doi: 10.1016/j.earscirev.2013.04.009

Woltemade, C. J., & Potter, K. W. (1994). A watershed modeling analysis of fluvial geomorphologic influences on flood peak attenuation. *Water Resources Research*, *30*(6), 1933–1942. Retrieved from http://dx.doi.org/10.1029/94WR00323 doi: 10.1029/94WR00323

Wormleaton, P. R., & Merrett, D. J. (1990). An improved method of calculation for steady uniform flow in prismatic main channel/flood plain sections. *Journal of Hydraulic Research*, *28*(2), 157–174.

Wu, W. (2008). *Computational river dynamics*. Taylor & Francis.

Yazdi, J., & Salehi Neyshabouri, S. a. a. (2012, oct). A Simulation-Based Optimization Model for Flood Management on a Watershed Scale. *Water Resources Management*, *26*(15), 4569–4586. Retrieved from http://link.springer.com/10.1007/s11269-012-0167-1 doi: 10.1007/s11269-012-0167-1

Yeh, G. T., Huang, G. B., Zhang, F., Cheng, H. P., & Lin, H. C. (2006). *WASH123D: a numerical model of flow, thermal transport, and salinity, sediment, and water quality transport in WAterSHed systems of 1-D stream-river network, 2-D overland regime, and 3-D subsurface media* (Tech. Rep.). Dept. of Civil and Environmental Engineering, Univ. of Central Florida, Orlando, FL.

Zhang, N., Li, P., & He, A. (2014, feb). Coupling of One-Dimensional and Two-Dimensional Hydrodynamic Models Using an Immersed-Boundary Method. *Journal of Fluids Engineering*,

*136*(4), 040907. Retrieved from http://fluidsengineering.asmedigitalcollection.asme.org/article.aspx?doi=10.1115/1.4025676 doi: 10.1115/1.4025676